Université d'Ottawa · University of Ottawa

Université d'Ottawa · University of Ottawa

FACULTÉ DES ÉTUDES SUPÉRIEURES ET POSTDOCTORALES

FACULTY OF GRADUATE AND POSTDOCTORAL STUDIES

LU, Junjie

AUTEUR DE LA THÈSE - AUTHOR OF THESIS

M.A.Sc. (Electrical Engineering)

GRADE - DEGREE

School of Information Technology and Engineering

FACULTÉ, ÉCOLE, DÉPARTEMENT - FACULTY, SCHOOL, DEPARTMENT

TITRE DE LA THÈSE - TITLE OF THE THESIS

Modelling Optical Waveguide Bends and Applications to Plasmon-polariton Waveguides

P. Berini

DIRECTEUR DE LA THÈSE - THESIS SUPERVISOR

EXAMINATEURS DE LA THÈSE - THESIS EXAMINERS

D. McNamara

B. Syrett

J.-M. De Koninck, Ph.D.

LE DOYEN DE LA FACULTÉ DES ÉTUDES SUPÉRIEURES ET POSTDOCTORALES

SIGNATURE

DEAN OF THE FACULTY OF GRADUATE AND POSTDOCTORAL STUDIES

Modelling Optical Waveguide Bends And Applications to Plasmon- polariton Waveguides

By

Junjie Lu

A thesis submitted to the
School of Graduate Studies and Research

Master of Applied Science
In Electrical Engineering

Ottawa-Carleton Institute for Electrical Engineering
School of Information Technology and Engineering
Faculty of Engineering
University of Ottawa

July 2003

Your file Votre référence
ISBN: 0-612-90113-0
Our file Notre référence
ISBN: 0-612-90113-0

Abstract

Optical waveguide bends are key building blocks in many integrated optical components. Accurate numerical modelling of these bends is of great practical value to the design of the integrated optical technology. Analyzed in this thesis are the propagation characteristics of optical waveguide bends based on the method of lines (MoL), not only for its good numerical performances (accuracy, speed of computation and minimal memory requirements), but also for its high suitability for the analysis of waveguide structures.

This thesis gives the detailed formulation for the calculation of the waveguide-bending radiation loss and the transition loss due to modal mismatch at the junctions. Besides, the 1D and 2D spatial field distribution algorithms are also covered in the formulation.

The code based on the formulation has been implemented successfully. To validate the code, we applied it to three typical waveguide structures appearing in other literatures and compared the results. The comparison shows that our code works very well, and can be used not only for the lossless dielectric media, but also for the lossy media at the optical frequency.

This thesis also explores the application of the developed code to metal waveguide bends. The numerical results of the propagation characteristics of the metal waveguide bends at the optical frequencies are presented for what is believed to be the first time.

Acknowledgments

I would like to sincerely thank my supervisor, Dr. Pierre Berini, for bringing the problem of modeling optical bends to my attention; for his suggestions, discussions and encouragements throughout this work, and for his financial support and confidence in my abilities as a researcher.

I also wish to convey my thanks to Dr. Derek McNamara, Dr. Paul Jay, Lucette Lepage, Lynne Richer, Suzanne St-Michel, and Andrée Carrière for their help during the studies for my master degree.

I am also indebted to Yansong Cui and other team members supervised by Dr. Pierre Berini, and to all the staff members in Spectalis company for their encouragement and fruitful discussions.

I am most grateful to my parents and parents-in-law for their care, support, and patience.

Finally, but definitely not least, I would like to thank Huiping Guo, my beloved wife who supported me continuously and patiently while I completed this work.

Contents

List of Figures

List of Tables

List of Acronyms

1D	One-Dimensional
2D	Two-Dimensional
AB	Absorbing Boundary
ABCs	Absorbing Boundary Conditions
AWG	Arrayed Waveguide Grating
EW	Electric Wall
FD-BPM	Finite Difference Beam Propagation Method
FDM	Finite Difference Method
FEM	Finite Element Method
MoL	Method of Lines
SFEM	Scalar Finite Element Method
TBCs	Transparent Boundary Conditions
TE	Transverse Electric
TM	Transverse Magnetic
WKB	Wen-Kramers-Brillouin

Chapter 1

Introduction

1.1 Background

Bent waveguides are key building blocks in many integrated optical components because they are used to achieve directional changes or displacements of waveguides, such as in directional couplers, modulators, switches and ring lasers, or in connection with components integrated on the same chip. The propagation characteristics of bent waveguides are mainly determined by three factors [1]:

- Radiation loss. When the field propagates along a bend with constant radius of curvature, some power will be lost by tangential radiation because of the finite speed of light in the cladding medium [2]. In practice, the radiation loss may be neglected if the radius of curvature of the bend is sufficiently large. However, in order to minimize the size of optical devices, the design of curved waveguides with small radii of curvature is necessary. The radiation loss increases rapidly as the radius of curvature decreases.
- Transition loss. This loss takes place where there is modal mismatch of fields at the junction of waveguides with different radii of curvature. For instance, the maximum of the guided mode in the bend will be shifted outward with a smaller

radius of curvature, and therefore, when connected to a straight waveguide, bigger mode mismatch and higher transition loss will occur.

- The change of phase constant. In addition to the effects such as radiation and transition loss, bending also causes changes in the phase constant [3]. For wavelength–selective waveguide devices such as the Mach-Zehnder interferometric (MZI) filter[4] and the arrayed-waveguide grating (AWG) [5] which require phase control in order to achieve wavelength accuracy, the effect of bending-induced phase-constant change is usually very important. In such cases, the accurate knowledge of the phase constant of bent sections is fundamental for the correct design of the device.

The propagation characteristics mentioned above in optical waveguide bends need to be accurately modeled so that a design rule could be set up and followed when designing bent waveguides with specific requirements.

1.2 Overview

In spite of their apparent simplicity, the analysis of the propagation characteristics in a bent waveguide continues to be a challenging electromagnetic problem. Since Marcatili [6] published the first theoretical paper on bends in 1969, lots of methods have been developed to analyze them. In summary, these methods are divided into three main categories: analytic approaches, semivectorial approaches and vectorial approaches.

A number of analytic approaches, up to now, have been used in analyzing the propagation in curved waveguide bends. Marcatili [6] analyzed a curved rectangular dielectric waveguide by dividing the waveguide cross-section into several regions. In each region, the field is expressed with Bessel or Hankel functions in the radial direction

and with sinusoidal or exponential functions in the axial direction, and field matching is performed along the sides of the rectangular core. Marcuse [7] analyzed a curved three-layer asymmetric slab waveguide. In each of the layers, the field is expressed with Bessel or Hankel functions, and the field matching is performed at their boundaries. Marcuse also derived formulae [8-10] for pure bending loss in symmetric slab waveguides and in optical fibers. Lewin [11], in analyzing the radiation loss from curved dielectric slabs or fibers, used the same technique of representing the field in the external region by using a Hankel function of complex order and matching to fields in the guide that were assumed unperturbed from a straight guide. Heiblum and Harris [12] analyzed the same asymmetric slab that Marcuse did. In their paper, the curved waveguide is conformally transformed to the corresponding straight waveguide. They broke up the transformed region into a series of constant index steps and applied a quantitative geometrical Wentzel-Kramers-Brillouin (WKB) approximation to determine the radiation and transition losses. Later on, Winker, Love, and Ghatak [13] used geometrical optics to determine the power attenuation in both the multimode slab and the fiber waveguide with step-index and parabolic core profiles. Berglund and Gopinath [14] improved the Heiblum-Harris analysis. They used the WKB method described by Janta and Gedeon [15-16] and carried out a more complete WKB analysis of the transformed structure.

Semivectorial analysis for bent waveguides mainly involves the finite difference beam propagation method (FD-BPM), the finite element method (FEM), and the method of lines (MoL). M. Rivera [17] used FD-BPM to analyze bent dielectric waveguides. In his scheme, transparent boundary conditions (TBCs) [18] are included. Yamamoto and Koshiba [19] employed the FEM to model curved waveguide bends. Their FEM scheme

was an approximate scalar FEM (SFEM). They extended the SFEM, for the first time, to include the loss due to the curvature of waveguides. Gu, Besse, and Melchior [20-21] presented a semivectorial approach based on the method of lines (MoL). To improve the accuracy of field matching at the interfaces between different media, they used an integral technique to obtain the matrix representation of the differential operator instead of using the difference quotient to approximate the differential operator.

The following approaches belong to the full-vectorial category. Bastiaansen, Keur, and Block [22] made a vectorial analysis of curved channel waveguides by using the source-type integral equation method. Kim and Gopinath [23] developed a finite-difference method (FDM) to analyze optical dielectric waveguide bends. In their paper, the finite-difference scheme was modified to satisfy the boundary conditions. Pascher and Pregla [24] implemented the vectorial analysis for curved rib waveguide bends by means of MoL. The discretization in their scheme is along the axial direction. The radial fields are expressed in terms of Bessel and Hankel functions of large complex orders and complex arguments. This in turn complicates the numerical calculations due to the requirement of special computer codes. To simply the numerical calculation, Pregla [25] put forward a new MoL algorithm, which does not need the Bessel or Hankel functions. In Pregla's new algorithm, discretization is along the radial direction and absorbing boundary conditions (ABCs) are introduced on the right side of the computation window.

1.3 Why Method of Lines

The method of lines (MoL) is a rigorous vectorial technique. The MoL is well known for its numerical performance: accuracy, speed of computation, and minimal memory

requirements. Furthermore, a number of papers [26-36] have shown that the MoL is highly suitable for the analysis of straight waveguide structures. Pregla, in his papers [24-25], further shows the MoL's superior accuracy when it is applied to analyze the optical waveguide bends.

1.4 Contribution of the Thesis

This thesis sets up a design tool for analyzing propagation characteristics in an optical waveguide bend using the algorithm suggested by Pregla [25]. The code has been implemented in Matlab.

In this thesis, for the first time, the transition loss is modelled using the method of lines (MoL). Pregla, in his paper [25], only gave the basic formulation for the radiation loss. In addition to the derivation of the ABCs, his work has been extended in two aspects: first, to formulate and compute 1D electromagnetic field distributions along the matching interface and to formulate and compute 2D spatial field distributions on the entire cross-section; second, to model the transition loss due to the modal mismatch of fields at junctions, which is never done by others using the MoL.

In this thesis, the radiation loss of metal optical waveguides due to bending is calculated. The finite-width metal waveguide has great potential for applications requiring short propagation distances and two-dimensional field confinement in the transverse plane. Up to now, much work [46-48] has been done for the analysis and characterization of the straight metal waveguides of finite width, but, to the author's best knowledge, no numerical work regarding the bending loss of the metal waveguide has appeared in the literature.

1.5 Organization of the Thesis

The rest of the thesis is structured as follows:

Chapter 2 gives the detailed formulation. It covers the algorithm described by R. Pragla, ABCs in cylindrical MoL, 1D and 2D field distributions, and transition loss based on 2D spatial field overlap integral.

Chapter 3 is devoted to the verification of the code and *Chapter 4* shows the applications of the modelling in practical designs for metal optical waveguides.

The last chapter, *Chapter 5*, is a brief conclusion to the former chapters and also presents some suggestions for future work.

Three appendices provide some extra information on Muller's Method, vector differential operators in the cylindrical coordinate system, and the component of ε_h at an abrupt transition.

Chapter 2

Formulation

2.1 Introduction

The formulation is based on the algorithm described by Pregla in [25]. Pregla's algorithm [25] is very flexible, not only suitable for the analysis of circular bends with simple cross-section shown in Fig. 2-1, but also valid for a multilayered structure with arbitrary number of layers. The general model of the multilayered waveguide is shown in Fig. 2-2. Each layer can be homogeneous or inhomogeneous. The permittivity of each layer is allowed to be complex and change abruptly, which provides the possibility to handle lossy media. The permittivity of each layer is radius-dependant.

However, Pregla only provided some basic formulation in his paper. In the first part of this chapter, more details on the formulation of radiation loss will be given. Besides, the ABCs on the right side of the computation window will be derived, which is the key to make Pregla's algorithm work.

Starting from Pregla's algorithm, further analysis will be done to make two extensions:

- Formulate 1D field distributions on the matching interface and 2D spatial field distributions on the entire cross-section of the bent waveguide structure. The former

helps identify different modes more easily while the latter is indispensable for modeling the transition loss.

- Formulate the transition loss due to the mode mismatch at the junction of waveguides with different radii of curvature.

2.2 Radiation Loss

2.2.1 Basic Equations

For the convenience of analysis, a single Hertz potential $\vec{\Pi}_e$ with two components, instead of two potentials with one component is introduced in the cylindrical coordinate system (r, φ, z). This enables the use of a more concise mathematical formulation with less algebraic manipulations than in the conventional approach. Thus the analysis is easier to follow and the computer algorithms are readily programmed. In this case, the vector potential $\vec{\Pi}_e$ has two components: Π_r and Π_φ. The solution is performed in the two coordinate directions r and φ. The permittivity may also depend on the two directions r and φ.

In the remainder of this section, starting from Maxwell's equations, we first give the derivation of the vector wave equation that the vector potential $\vec{\Pi}_e$ satisfies, and the vector field expressions based on the vector potential $\vec{\Pi}_e$. We then expand them into corresponding scalar wave equations and six field component expressions.

In an isotropic source-free region, Maxwell's equations are expressed as [37]:

$$\nabla \times \vec{H} = j\omega\varepsilon_0\varepsilon_r\vec{E} \tag{2.1}$$

$$\nabla \times \vec{E} = -j\omega\mu_0\mu_r\vec{H} \tag{2.2}$$

$$\nabla \bullet \vec{B} = 0 \tag{2.3}$$

$$\nabla \bullet \vec{D} = 0 = \nabla \bullet (\varepsilon_r \vec{E}) \tag{2.4}$$

For the dielectric case, Eq. (2.3) becomes $\nabla \bullet \vec{H} = 0$ since $\mu_r = 1$ and μ_0 is a constant. We may therefore take:

$$\vec{H} = j\omega\varepsilon_0 \nabla \times \vec{\Pi}_e \tag{2.5}$$

Combining (2.2) with (2.5) we yield:

$$\nabla \times \vec{E} = k_o^2 \, \nabla \times \vec{\Pi}_e \tag{2.6}$$

Here, k_o is the free space wave number, i.e. $k_o = \omega\sqrt{\varepsilon_0\mu_0}$. Integration is performed on Eq. (2.6) and the following result is obtained:

$$\vec{E} = k_o^2 \, \vec{\Pi}_e + \nabla\phi \tag{2.7}$$

where ϕ is as yet an arbitrary scalar function. Taking the curl of (2.5), we get:

$$\nabla \times \vec{H} = j\omega\varepsilon_0 \nabla \times \nabla \times \vec{\Pi}_e = j\omega\varepsilon_0\varepsilon_r\vec{E} \tag{2.8}$$

Expanding and substituting for $\vec{E}$ gives:

$$\nabla\nabla \bullet \vec{\Pi}_e - \nabla^2 \vec{\Pi}_e = \varepsilon_r k_o^2 \, \vec{\Pi}_e + \varepsilon_r \nabla\phi = \varepsilon_r k_o^2 \, \vec{\Pi}_e + \nabla(\varepsilon_r\phi) - \phi\nabla\varepsilon_r \tag{2.9}$$

Since $\nabla \bullet \vec{\Pi}_e$ and ϕ are arbitrary up to this point, we choose the following relation between them:

$$\nabla\nabla \bullet \vec{\Pi}_e = \nabla(\varepsilon_r\phi) \tag{2.10}$$

Equation (2.10) integrates to $\nabla \bullet \vec{\Pi}_e = \varepsilon_r\phi$ apart from an irrelevant constant. Thus, the following equation for $\vec{\Pi}_e$ is obtained:

$$\nabla^2 \vec{\Pi}_e - \varepsilon_r^{-1}(\nabla \varepsilon_r)\nabla \cdot \vec{\Pi}_e + \varepsilon_r k_o^2 \vec{\Pi}_e = 0 \tag{2.11}$$

The equation (2.7) for $\vec{E}$ becomes:

$$\vec{E} = k_o^2 \vec{\Pi}_e + \nabla(\varepsilon_r^{-1}\nabla \bullet \vec{\Pi}_e) = k_o^2 \vec{\Pi}_e - \nabla \bullet \vec{\Pi}_e \varepsilon_r^{-2}\nabla \varepsilon_r + \varepsilon_r^{-1}\nabla\nabla \bullet \vec{\Pi}_e \tag{2.12}$$

From (2.11) we can get:

$$k_o^2 \vec{\Pi}_e = \varepsilon_r^{-2}(\nabla \varepsilon_r)\nabla \cdot \vec{\Pi}_e - \varepsilon_r^{-1}\nabla^2 \vec{\Pi}_e \tag{2.13}$$

Substituting (2.13) into (2.12) yields the following equation:

$$\vec{E} = \varepsilon_r^{-1}\nabla\nabla \bullet \vec{\Pi}_e - \varepsilon_r^{-1}\nabla^2 \vec{\Pi}_e = \varepsilon_r^{-1}\nabla \times \nabla \times \vec{\Pi}_e \tag{2.14}$$

After manipulation, (2.5) can be rewritten as:

$$\eta_o \vec{H} = jk_o \nabla \times \vec{\Pi}_e \tag{2.15}$$

where $\eta_o = \sqrt{\dfrac{\mu_o}{\varepsilon_o}}$.

To simplify the formulation, the coordinates and the dimensions are normalized as follows: $\bar{z} = k_o z$, $\bar{r} = k_o r, \bar{r}_o = k_o r_o, \bar{r}_n = \bar{r}/\bar{r}_o$, where r_o is the mean radius of the bend, namely the distance between the circular center and the vertical symmetry axis of the bend cross-section (see Fig.2-3). In the normalized cylindrical coordinate system, (2.13), (2.14) and (2.15) become:

$$\nabla^2 \vec{\Pi}_e - \varepsilon_r^{-1}(\nabla \varepsilon)\nabla \cdot \vec{\Pi}_e + \varepsilon_r \vec{\Pi}_e = 0 \tag{2.16}$$

$$\vec{E} = \varepsilon_r^{-1} \nabla \times \nabla \times \vec{\Pi}_e \tag{2.17}$$

$$\eta_o \vec{H} = j\nabla \times \vec{\Pi}_e \tag{2.18}$$

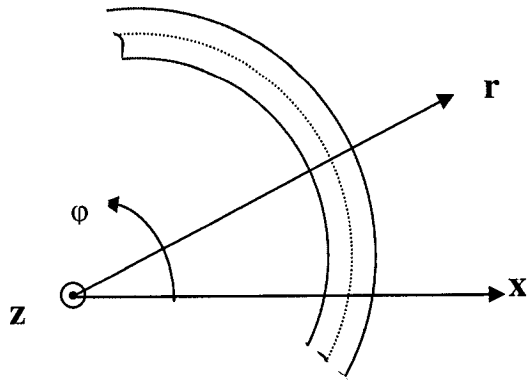

(a) Circular optical waveguide

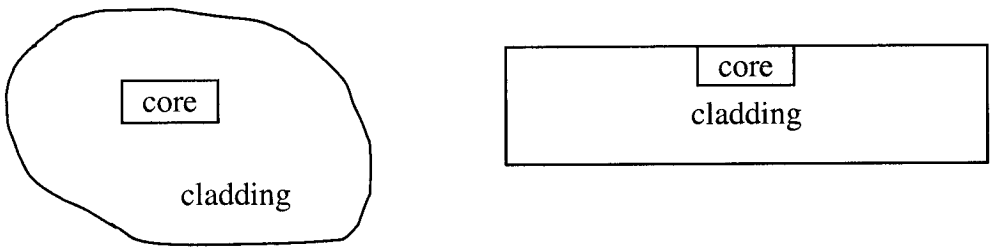

(b) Examples of the bend with embedded cross-section structure

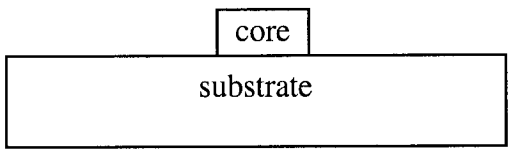

(c) Example of the bend with strip cross-section structure

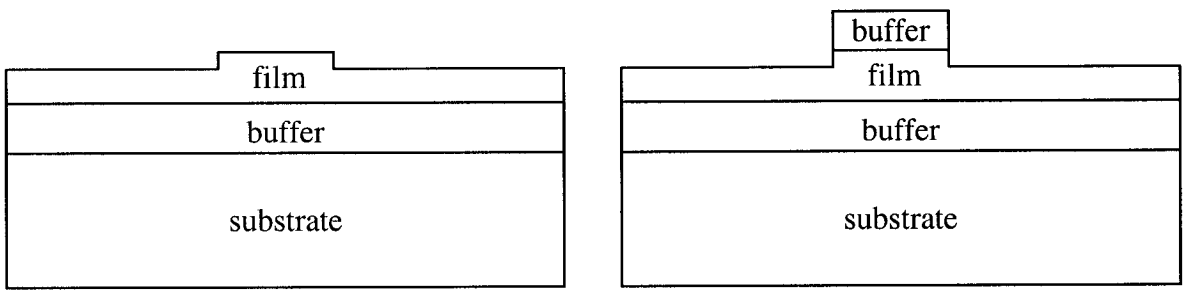

(d) Examples of the bend with rib cross-section structures

Fig. 2-1 Circular bends with simple cross-section. (a) top view of propagation along φ; (b),(c),(d) cross-section view.

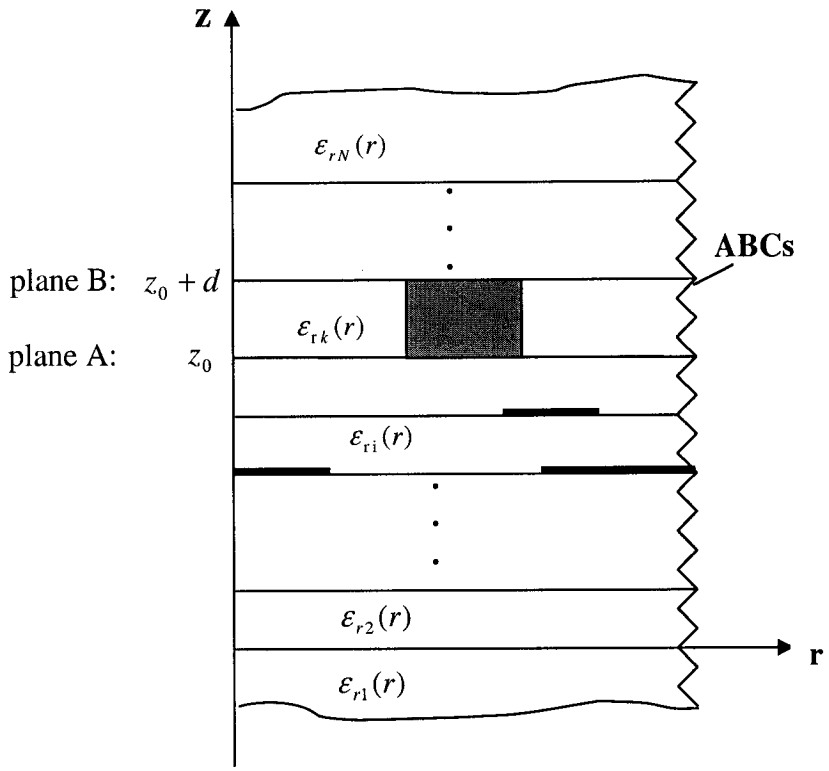

Fig. 2-2 General model for circular multilayered waveguide structures

Two things are assumed: first, the permittivity of each layer is only a function of the radial coordinate, i.e. $\varepsilon_r = \varepsilon_r(\bar{r})$; second, a wave propagates in the $+\varphi$ direction according to $\exp(-jk_\varphi \varphi) = \exp(-j\sqrt{\varepsilon_{re}}\,\bar{u})$ with $\bar{u} = \varphi \bar{r}_o$ and $\sqrt{\varepsilon_{re}} = k_\varphi / \bar{r}_o$. As a result: $\partial / \partial \varphi = -jk_\varphi = -j\sqrt{\varepsilon_{re}}\,\bar{r}_o$. The vector wave equation (2.16) is expanded into two coupled scalar wave equations (2.19) and (2.20):

$$\frac{\partial^2(\bar{r}_n \Pi_r)}{\partial \bar{z}^2} + \bar{r}_n \varepsilon_r \frac{\partial}{\partial \bar{r}}\left[\frac{1}{\bar{r}_n \varepsilon_r}\frac{\partial}{\partial \bar{r}}(\bar{r}_n \Pi_r)\right] + (\varepsilon_r - \frac{\varepsilon_{re}}{\bar{r}_n^{\,2}})(\bar{r}_n \Pi_r)$$

$$-j\sqrt{\varepsilon_{re}}\left[\bar{r}_n\varepsilon_r\frac{\partial}{\partial\bar{r}}(\frac{1}{\bar{r}_n\varepsilon_r}\Pi_\varphi)-\frac{1}{\bar{r}_n}\frac{\partial}{\partial\bar{r}}(\bar{r}_n\Pi_\varphi)\right]=0 \tag{2.19}$$

$$\frac{\partial^2(\bar{r}_n\Pi_\varphi)}{\partial\bar{z}^2}+\bar{r}_n\frac{\partial}{\partial\bar{r}_n}\left[\frac{1}{\bar{r}_n}\frac{\partial}{\partial\bar{r}}(\bar{r}_n\Pi_\varphi)\right]+(\varepsilon_r-\frac{\varepsilon_{re}}{\bar{r}_n^{\,2}})(\bar{r}_n\Pi_\varphi)$$

$$-j\sqrt{\varepsilon_{re}}\left[\frac{1}{\bar{r}_n}\frac{\partial}{\partial\bar{r}}(\bar{r}_n\Pi_r)-\bar{r}_n\frac{\partial}{\partial\bar{r}}(\frac{1}{\bar{r}_n}\Pi_r)\right]=0 \tag{2.20}$$

Eq. (2.17) is expanded into (2.21) to (2-23).

$$\varepsilon_r E_r=-\frac{\partial^2\Pi_r}{\partial\bar{z}^2}-j\frac{\sqrt{\varepsilon_{re}}}{\bar{r}_n}\left[\frac{1}{\bar{r}_n}\frac{\partial}{\partial\bar{r}}(\bar{r}_n\Pi_\varphi)+j\frac{\sqrt{\varepsilon_{re}}}{\bar{r}_n}\Pi_r\right] \tag{2.21}$$

$$\varepsilon_r E_\varphi=-\frac{\partial^2\Pi_\varphi}{\partial\bar{z}^2}-\frac{\partial}{\partial\bar{r}}\left[\frac{1}{\bar{r}_n}\frac{\partial}{\partial\bar{r}}(\bar{r}_n\Pi_\varphi)+j\frac{\sqrt{\varepsilon_{re}}}{\bar{r}_n}\Pi_r\right] \tag{2.22}$$

$$\varepsilon_r E_z=\frac{\partial}{\partial\bar{z}}\left[\frac{1}{\bar{r}_n}\frac{\partial}{\partial\bar{r}}(\bar{r}_n\Pi_r)-\frac{j\sqrt{\varepsilon_{re}}}{\bar{r}_n}\Pi_\varphi\right] \tag{2.23}$$

Similarly, from Eq.(2.18), three other field components are expanded:

$$\eta_o H_r=-j\frac{\partial}{\partial\bar{z}}\Pi_\varphi \tag{2.24}$$

$$\eta_o H_\varphi=j\frac{\partial}{\partial\bar{z}}\Pi_r \tag{2.25}$$

$$\eta_o H_z=j\left[\frac{1}{\bar{r}_n}\frac{\partial}{\partial\bar{r}}(\bar{r}_n\Pi_\varphi)+\frac{j\sqrt{\varepsilon_{re}}}{\bar{r}_n}\Pi_r\right]. \tag{2.26}$$

2.2.2 Discretization and solution of the wave equation

Following the analysis steps of the MoL, the coupled partial differential equation (2.19) and (2.20) should be discretized to obtain ordinary differential equations which can be solved analytically. As stated, the discretization is applied in the radial direction. For convenience, the potentials are normalized according to:

$$\sqrt{\bar{r}_n}\,\Pi_\varphi = \Pi_{\varphi n} \tag{2.27}$$

$$\sqrt{\bar{r}_n}\,\Pi_r = \Pi_{rn}. \tag{2.28}$$

After normalization, (2.19) and (2.20) are rewritten to (2.29) and (2.30) respectively:

$$\frac{\partial^2(\Pi_{rn})}{\partial \bar{z}^2} + \sqrt{\bar{r}_n}\varepsilon_r \frac{\partial}{\partial \bar{r}}\left[\frac{1}{\sqrt{\bar{r}_n}}\frac{1}{\sqrt{\bar{r}_n}\varepsilon_r}\frac{\partial}{\partial \bar{r}}(\sqrt{\bar{r}_n}\,\Pi_{rn})\right] + (\varepsilon_r - \frac{\varepsilon_{re}}{\bar{r}_n^{\,2}})(\Pi_{rn})$$

$$-j\sqrt{\varepsilon_{re}}\left[\varepsilon_r \bar{r}_n \frac{1}{\sqrt{\bar{r}_n}}\frac{\partial}{\partial \bar{r}}(\sqrt{\bar{r}_n}\frac{1}{\bar{r}_n^{\,2}\varepsilon_r}\Pi_{\varphi n}) - \frac{1}{\bar{r}_n}\frac{1}{\sqrt{\bar{r}_n}}\frac{\partial}{\partial \bar{r}}(\sqrt{\bar{r}_n}\,\Pi_{\varphi n})\right] = 0 \tag{2.29}$$

$$\frac{\partial^2(\Pi_{\varphi n})}{\partial \bar{z}^2} + \sqrt{\bar{r}_n}\frac{\partial}{\partial \bar{r}}\left[\frac{1}{\sqrt{\bar{r}_n}}\frac{1}{\sqrt{\bar{r}_n}}\frac{\partial}{\partial \bar{r}}(\sqrt{\bar{r}_n}\,\Pi_{\varphi n})\right] + (\varepsilon_r - \frac{\varepsilon_{re}}{\bar{r}_n^{\,2}})(\Pi_{\varphi n})$$

$$-j\sqrt{\varepsilon_{re}}\left[\frac{1}{\bar{r}_n}\frac{1}{\sqrt{\bar{r}_n}}\frac{\partial}{\partial \bar{r}}(\sqrt{\bar{r}_n}\,\Pi_{rn}) - \bar{r}_n\frac{1}{\sqrt{\bar{r}_n}}\frac{\partial}{\partial \bar{r}}(\sqrt{\bar{r}_n}\frac{1}{\bar{r}_n^{\,2}}\Pi_{rn})\right] = 0 \tag{2.30}$$

In this case, not only the potentials but also the permittivities and the radial coordinate r have to be discretized. A discretization as shown in Fig. 2-3, on two shifted line systems, which achieves accurate field matching at all dielectric interfaces, will be

applied. For the calculation window, an electric wall (EW) is placed on the top and bottom boundary respectively, while a magnetic wall (MW) or EW can be placed on the left side boundary because the bending shifts the modal fields outward, and an absorbing boundary (AB) is introduced for the right side of the calculation window. For Π_r, E_r, H_φ, and H_z, the Dirichlet boundary condition is therefore applied on the left side of the calculation window and the Newmann boundary condition is employed on the right side of the calculation window. With respect to Π_φ, H_r, E_φ, and E_z, the Newmann boundary condition is applied on the left side and an absorbing boundary condition (ABC) is placed on the right side of the calculation window. The discretization yields the results as follows:

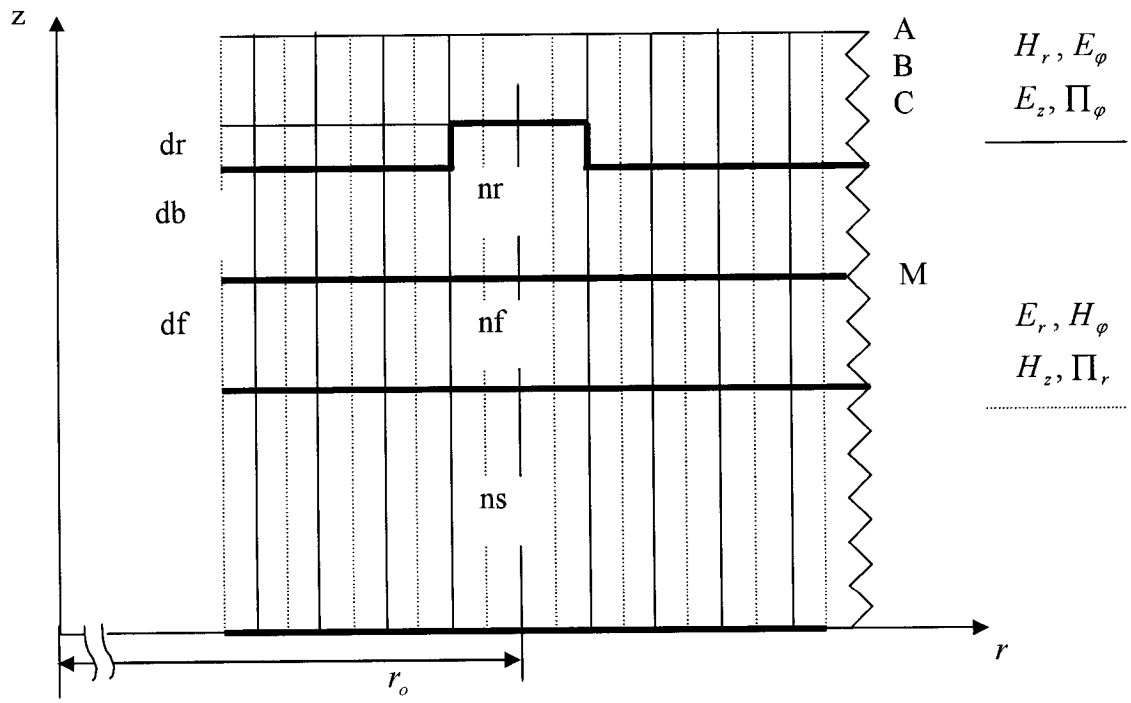

Fig. 2-3 A rib waveguide bend cross-section with shifted discretization lines

H lines:

$$\Pi_{rn} \rightarrow \vec{\Pi}_{rn} \text{ (vector)} \tag{2.31}$$

$$\varepsilon_r \rightarrow \bar{\varepsilon}_h \tag{2.32}$$

$$\bar{r}_n \rightarrow \bar{r}_h \tag{2.33}$$

$$\frac{\partial}{\partial \bar{r}} \rightarrow \bar{h}^{-1} D_h = \bar{D}_h \tag{2.34}$$

$$\sqrt{\bar{r}_n}^{-1} \frac{\partial}{\partial \bar{r}} (\sqrt{\bar{r}_n}\, \Pi_{rn}) \rightarrow \bar{D}_{hn} \vec{\Pi}_{rn} \tag{2.35}$$

$$D_{hn} = \sqrt{\bar{r}_e}^{-1} D_h \sqrt{\bar{r}_h} \tag{2.36}$$

Considering the boundary condition combination for Π_r, the backward difference scheme is employed, so we can get:

$$\frac{\partial}{\partial \bar{r}} \Pi_{rn}\Big|_i^b = \frac{\Pi_{rn,i} - \Pi_{rn,i-1}}{\bar{h}} \tag{2.37}$$

$$\frac{\partial}{\partial \bar{r}} \Pi_{rn}\Big|_1^b = \frac{\Pi_{rn,1} - \Pi_{rn,0}}{\bar{h}} = \frac{\Pi_{rn,1}}{\bar{h}} \tag{2.38}$$

$$\frac{\partial}{\partial \bar{r}} \Pi_{rn}\Big|_N^b = \frac{\Pi_{rn,N} - \Pi_{rn,N-1}}{\bar{h}} \tag{2.39}$$

$$D_h = \begin{bmatrix} 1 & & & & & \\ -1 & 1 & & & & \\ & -1 & 1 & & & \\ & & \ddots & \ddots & & \\ & & & \ddots & \ddots & \\ & & & & -1 & 1 \end{bmatrix} \tag{2.40}$$

E lines:

$$\Pi_{\varphi n} \rightarrow \bar{\Pi}_{\varphi n} \text{ (vector)} \tag{2.41}$$

$$\varepsilon_r \rightarrow \bar{\varepsilon}_e \tag{2.42}$$

$$\bar{r}_n \rightarrow \bar{r}_e \tag{2.43}$$

$$\frac{\partial}{\partial \bar{r}} \rightarrow \bar{h}^{-1} D_e = \bar{D}_e \tag{2.44}$$

$$\sqrt{\bar{r}_n}^{-1} \frac{\partial}{\partial \bar{r}} (\sqrt{\bar{r}_n}\, \Pi_{en}) \rightarrow \bar{D}_{en}\, \bar{\Pi}_{\varphi n} \tag{2.45}$$

$$D_{en} = \sqrt{\bar{r}_h}^{-1} D_e \sqrt{\bar{r}_e}\ . \tag{2.46}$$

For Π_φ, the forward difference scheme is applied taking account into the boundary condition combination, the following results hence yield:

$$\frac{\partial}{\partial \bar{r}} \Pi_{\varphi n}\Big|_i^f = \frac{\Pi_{\varphi n, i+1} - \Pi_{\varphi n, i}}{\bar{h}} \tag{2.47}$$

$$\frac{\partial}{\partial \bar{r}} \Pi_{\varphi n}\Big|_1^f = \frac{\Pi_{\varphi n, 2} - \Pi_{\varphi n, 1}}{\bar{h}} \tag{2.48}$$

$$\frac{\partial}{\partial \bar{r}} \Pi_{\varphi n}\Big|_N^f = \frac{\Pi_{\varphi n, N+1} - \Pi_{\varphi n, N}}{\bar{h}} \tag{2.49}$$

$$D_e = \begin{bmatrix} -1 & 1 & & & & & \\ & -1 & 1 & & & & \\ & & -1 & 1 & & & \\ & & & \ddots & \ddots & & \\ & & & & \ddots & \ddots & \\ & & & & & -1 & 1 \\ & & & & & c & b & -1-a \end{bmatrix} \tag{2.50}$$

(a, b and c definition see 2.2.5)

Here, $\bar{h} = k_o h$ is the normalized discretization distance. $\bar{\varepsilon}_h$, $\bar{\varepsilon}_e$, $\bar{r}_h$ and $\bar{r}_e$ are diagonal matrices. The subscripts indicate the discretization line system to which the quantities belong. Since Π_r and H_z are discretized on the same line system, the quantities on this system are marked with the subscript h. The quantities on the discretization line system for Π_φ are marked with the subscript e, because E_z is also discretized on this same system of lines.

After discretization, the wave equations (2.29) and (2.30) will become:

$$\frac{d^2}{d\bar{z}^2}\vec{\Pi}_{rn} - \left[\bar{\varepsilon}_h \bar{D}_{hn}^t \bar{\varepsilon}_e^{-1} \bar{D}_{hn} + \varepsilon_{re} \bar{r}_h^{-2} - \bar{\varepsilon}_h\right]\vec{\Pi}_{rn}$$

$$+ j\sqrt{\varepsilon_{re}}\left[\bar{r}_h^{-1} \bar{D}_{en} - \bar{\varepsilon}_h \bar{r}_h \bar{D}_{en} \bar{\varepsilon}_e^{-1} \bar{r}_e^{-2}\right]\vec{\Pi}_{\varphi n} = 0 \qquad (2.51)$$

$$\frac{d^2}{d\bar{z}^2}\vec{\Pi}_{\varphi n} - \left[\bar{D}_{en}^t \bar{D}_{en} + \varepsilon_{re} \bar{r}_e^{-2} - \bar{\varepsilon}_e\right]\vec{\Pi}_{\varphi n}$$

$$- j\sqrt{\varepsilon_{re}}\left[\bar{r}_e^{-1} \bar{D}_{hn} - \bar{r}_e \bar{D}_{hn} \bar{r}_h^{-2}\right]\vec{\Pi}_{rn} = 0 \qquad (2.52)$$

with

$$\bar{D}_{hn}^t = \bar{h}^{-1} D_{hn}^t = \bar{h}^{-1} (\sqrt{\bar{r}_e}^{-1} D_h \sqrt{\bar{r}_h})^t$$

$$= \bar{h}^{-1} (\sqrt{\bar{r}_h}\ D_h{}^t \sqrt{\bar{r}_e}^{-1})$$

$$= -\bar{h}^{-1} (\sqrt{\bar{r}_h}\ D_e \sqrt{\bar{r}_e}^{-1}) \qquad (2.53)$$

$$\bar{D}_{en}^t = \bar{h}^{-1} D_{en}^t = \bar{h}^{-1} (\sqrt{\bar{r}_h}^{-1} D_e \sqrt{\bar{r}_e})^t$$

$$= \bar{h}^{-1}(\sqrt{\bar{r}_e}\ D_e^{\ t}\sqrt{\bar{r}_h}^{-1})$$

$$= -\bar{h}^{-1}(\sqrt{\bar{r}_e}\ D_h\ \sqrt{\bar{r}_h}^{-1}). \tag{2.54}$$

For the sake of brevity a super-vector is introduced.

$$\hat{\Pi}_n = \begin{bmatrix} \vec{\Pi}_{rn} \\ -j\vec{\Pi}_{\varphi n} \end{bmatrix}. \tag{2.55}$$

The symbol (^) on the quantities indicates super-vectors and super-matrices. Accordingly, the discretized wave equation (2.51) and (2.52) is rewritten in a shorter form

$$\frac{d^2}{d\bar{z}^2}\hat{\Pi}_n - \hat{Q}\hat{\Pi}_n = 0. \tag{2.56}$$

Where $\hat{Q}$ is a super-matrix consisting of four sub-matrices :

$$\hat{Q}_{11} = \vec{\varepsilon}_h \bar{D}_{hn}^t \vec{\varepsilon}_e^{\ -1} \bar{D}_{hn} + \varepsilon_{re}\vec{r}_h^{\ -2} - \vec{\varepsilon}_h \tag{2.57}$$

$$\hat{Q}_{12} = \sqrt{\varepsilon_{re}}(\vec{r}_h^{\ -1}\bar{D}_{en} - \vec{\varepsilon}_h\vec{r}_h\ \bar{D}_{en}\vec{\varepsilon}_e^{\ -1}\vec{r}_e^{\ -2}) \tag{2.58}$$

$$\hat{Q}_{21} = \sqrt{\varepsilon_{re}}(\vec{r}_e^{-1}\ \bar{D}_{hn} - \vec{r}_e\bar{D}_{hn}\vec{r}_h^{\ -2}) \tag{2.59}$$

$$\hat{Q}_{22} = \bar{D}_{en}^t\bar{D}_{en} + \varepsilon_{re}\vec{r}_e^{\ -2} - \vec{\varepsilon}_e\ . \tag{2.60}$$

To solve (2.56), it must first be uncoupled. Uncoupling is achieved by transforming $\hat{Q}$ to main axes i.e. diagonalization. Diagonalizing $\hat{Q}$ is done according to

$$\hat{T}^{-1}\,\hat{Q}\,\hat{T} = \hat{\Gamma}^2 \tag{2.61}$$

$$\hat{\Pi}_n = \hat{T}\,\hat{\overline{\Pi}}_n . \tag{2.62}$$

In the transformation domain, the uncoupled version of (2.56) is obtained by

$$\frac{d^2}{d\bar{z}^2}\hat{\overline{\Pi}}_n - \hat{\Gamma}^2\,\hat{\overline{\Pi}}_n = 0 . \tag{2.63}$$

(2.63) is an uncoupled telegrapher's equation along $\bar{z}$. Its analytical solution is expressed by

$$\hat{\overline{\Pi}}_n = \cosh\left[\hat{\Gamma}(\bar{z}-\bar{z}_o)\right]\hat{C}_1 + \sinh\left[\hat{\Gamma}(\bar{z}-\bar{z}_o)\right]\hat{C}_2 \tag{2.64}$$

$$\frac{d}{d\bar{z}}\hat{\overline{\Pi}}_n = \sinh\left[\hat{\Gamma}(\bar{z}-\bar{z}_o)\right]\hat{\Gamma}\hat{C}_1 + \cosh\left[\hat{\Gamma}(\bar{z}-\bar{z}_o)\right]\hat{\Gamma}\hat{C}_2 \tag{2.65}$$

with

$$\hat{C}_1 = \hat{\overline{\Pi}}_n(\bar{z}_o) \text{ and}$$

$$\hat{C}_2 = \frac{d}{d\bar{z}}\hat{\overline{\Pi}}_n(\bar{z}_o) .$$

At the planes A ($z = z_o$) and B ($z = z_o + d$), the following results from (2.64):

$$\hat{\bar{\Pi}}_{nA} = \hat{C}_1 \tag{2.66}$$

$$\hat{\bar{\Pi}}_{nB} = (\cosh \hat{\Gamma}\bar{d})\hat{C}_1 + (\sinh \hat{\Gamma}\bar{d})\hat{C}_2 . \tag{2.67}$$

(2.66) and (2.67) are rewritten in a more compact form:

$$\begin{bmatrix} \hat{\bar{\Pi}}_{nA} \\ \hat{\bar{\Pi}}_{nB} \end{bmatrix} = \begin{bmatrix} I & o \\ \cosh \hat{\Gamma}\bar{d} & \sinh \hat{\Gamma}\bar{d} \end{bmatrix} \begin{bmatrix} \hat{C}_1 \\ \hat{C}_2 \end{bmatrix} \tag{2.68}$$

For the derivatives in the same planes, the results from (2.65) are as follows:

$$\frac{d}{d\bar{z}} \hat{\bar{\Pi}}_{nA} = \hat{\Gamma}\hat{C}_2 \tag{2.69}$$

$$\frac{d}{d\bar{z}} \hat{\bar{\Pi}}_{nB} = \sinh\left[\hat{\Gamma}\bar{d}\right]\hat{\Gamma}\hat{C}_1 + \cosh\left[\hat{\Gamma}\bar{d}\right]\hat{\Gamma}\hat{C}_2 . \tag{2.70}$$

$\hat{C}_2$ is solved from (2.67):

$$\hat{C}_2 = (\sinh \hat{\Gamma}\bar{d})^{-1}\left[\hat{\bar{\Pi}}_{nB} - (\cosh \hat{\Gamma}\bar{d})\hat{C}_1 \right] \tag{2.71}$$

with

$$\hat{C}_1 = \hat{\bar{\Pi}}_{nA} .$$

$\hat{C}_1, \hat{C}_2$ are substituted into (2.69) and (2.70) with the above expressions yielding:

$$\frac{d}{d\bar{z}}\hat{\bar{\Pi}}_{nA} = -\hat{\Gamma}(\tanh\hat{\Gamma}\bar{d})^{-1}\hat{\bar{\Pi}}_{nA} + \hat{\Gamma}(\sinh\hat{\Gamma}\bar{d})^{-1}\hat{\bar{\Pi}}_{nB} \tag{2.72}$$

$$\frac{d}{d\bar{z}}\hat{\bar{\Pi}}_{nB} = -\hat{\Gamma}(\sinh\hat{\Gamma}\bar{d})^{-1}\hat{\bar{\Pi}}_{nA} + \hat{\Gamma}(\tanh\hat{\Gamma}\bar{d})^{-1}\hat{\bar{\Pi}}_{nB}. \tag{2.73}$$

(2.72) and (2.73) are rewritten into a more compact form

$$\frac{d}{d\bar{z}}\begin{bmatrix}\hat{\bar{\Pi}}_{nA}\\ \hat{\bar{\Pi}}_{nB}\end{bmatrix} = \hat{\Gamma}^2\begin{bmatrix}-\hat{\gamma} & \hat{\alpha}\\ -\hat{\alpha} & \hat{\gamma}\end{bmatrix}\begin{bmatrix}\hat{\bar{\Pi}}_{nA}\\ \hat{\bar{\Pi}}_{nB}\end{bmatrix} \tag{2.74}$$

with $\hat{\gamma} = (\hat{\Gamma}\tanh\hat{\Gamma}\bar{d})^{-1}$

and $\hat{\alpha} = (\hat{\Gamma}\sinh\hat{\Gamma}\bar{d})^{-1}$.

Here, expressions for $\hat{\gamma}$ and $\hat{\alpha}$ are used for a layer with a finite thickness. For a layer with infinite thickness (compared with the wavelength), these expressions are simplified according to:

$$\hat{\gamma} = \begin{cases}\hat{\Gamma}^{-1} & \textit{if the real parts of } \hat{\Gamma} \textit{ are positive}\\ -\hat{\Gamma}^{-1} & \textit{if the real parts of } \hat{\Gamma} \textit{ are negative}\end{cases}$$

$$\hat{\alpha} = o.$$

The above are based on the following relations:

$$\tanh(a+jb) \rightarrow +1 \quad if\ a \rightarrow +\infty$$
$$\rightarrow -1 \quad if\ a \rightarrow -\infty$$

$$\sinh(a+jb) \rightarrow \pm\infty \quad if\ a \rightarrow \pm\infty$$

$$\frac{1}{\sinh(a+jb)} \rightarrow 0 \quad if\ a \rightarrow \pm\infty$$

2.2.3 Fields and Their Transformations between Layer Interfaces

To facilitate their manipulation, some simplifications will be done on the field components. First, the components are normalized according to:

$$\sqrt{\bar{r}_n}E_\varphi = E_{\varphi n} \tag{2.75}$$

$$\sqrt{\bar{r}_n}E_r = E_{rn} \tag{2.76}$$

$$\sqrt{\bar{r}_n}E_z = E_{zn} \tag{2.77}$$

$$\sqrt{\bar{r}_n}H_\varphi = H_{\varphi n} \tag{2.78}$$

$$\sqrt{\bar{r}_n}H_r = H_{rn} \tag{2.79}$$

$$\sqrt{\bar{r}_n}H_z = H_{zn}; \tag{2.80}$$

Second, the discretization is applied on two shifted different line systems as shown in Fig. 2-3 yielding:

E lines

$$E_{\varphi n} \rightarrow \vec{E}_{\varphi n} \text{ (vector)} \tag{2.81}$$

$$E_{zn} \rightarrow \vec{E}_{zn} \text{ (vector)} \tag{2.82}$$

$$H_{rn} \rightarrow \vec{H}_{rn} \text{ (vector)} \tag{2.83}$$

H lines

$$H_{\varphi n} \rightarrow \vec{H}_{\varphi n} \text{ (vector)} \tag{2.84}$$

$$H_{zn} \rightarrow \vec{H}_{zn} \text{ (vector)} \tag{2.85}$$

$$E_{rn} \rightarrow \vec{E}_{rn} \text{ (vector);} \tag{2.86}$$

Next, super-vectors are introduced for the fields transverse to the layer interfaces:

$$\hat{E}_n = \begin{bmatrix} \vec{E}_{rn} \\ -j\vec{E}_{\varphi n} \end{bmatrix} \tag{2.87}$$

$$\hat{H}_n = \eta_o \begin{bmatrix} -j\vec{H}_{\varphi n} \\ \vec{H}_{rn} \end{bmatrix} \tag{2.88}$$

and the super-matrix for the relative permittivities:

$$\underset{(2N\times 2N)}{\hat{\varepsilon}} = \begin{bmatrix} \bar{\varepsilon}_h & O \\ O & \bar{\varepsilon}_e \end{bmatrix}; \tag{2.89}$$

where $\bar{\varepsilon}_h$, $\bar{\varepsilon}_e$ are diagonal matrices $(N \times N)$ and O represents the $(N \times N)$ zero matrix.

Last, the super-matrix $\hat{R}$ is defined as:

$$\hat{R} = \hat{\varepsilon}^{-1}\left\{ \hat{Q} + \begin{bmatrix} -\varepsilon_{re}\bar{r}_h^{-2} & -\sqrt{\varepsilon_{re}}\bar{r}_h^{-1}\bar{D}_{en} \\ \sqrt{\varepsilon_{re}}\bar{r}_e\ \bar{\varepsilon}_e^{-1}\bar{D}_{hn}\bar{r}_h^{-2} & -\bar{D}_{en}^t\ \bar{D}_{en} \end{bmatrix}\right\}$$

$$= \begin{bmatrix} \hat{R}_{11} & \hat{R}_{12} \\ \hat{R}_{21} & \hat{R}_{22} \end{bmatrix} \tag{2.90}$$

with

$$\hat{R}_{11} = \bar{D}_{hn}^t \bar{\varepsilon}_e^{-1}\bar{D}_{hn} - I_h \tag{2.91}$$

$$\hat{R}_{12} = -\sqrt{\varepsilon_{re}}\bar{r}_h\ \bar{D}_{en}\bar{\varepsilon}_e^{-1}\bar{r}_e^{-2} \tag{2.92}$$

$$\hat{R}_{21} = \sqrt{\varepsilon_{re}}\bar{r}_e^{-1}\bar{\varepsilon}_e^{-1}\ \bar{D}_{hn} \tag{2.93}$$

$$\hat{R}_{22} = \varepsilon_{re}\bar{r}_e^{-2}\bar{\varepsilon}_e^{-1} - I_e \blacksquare \tag{2.94}$$

Using the definitions given above, the transverse fields are written as:

$$\hat{E}_n = -\hat{R}\ \hat{\Pi}_n \tag{2.95}$$

$$\hat{H}_n = \frac{d}{d\bar{z}}\hat{\Pi_n}. \tag{2.96}$$

In the transformed domain, if the definition

$$\hat{E}_n = \hat{T}\,\hat{\bar{E}}_n \tag{2.97}$$

$$\hat{H}_n = \hat{T}\,\hat{\bar{H}}_n \tag{2.98}$$

is given, where $\hat{\bar{E}}_n$ and $\hat{\bar{H}}_n$ are field quantities in the transformed domain,

then the following equations will result after combining them with (2.95) and (2.96):

$$\frac{\partial}{\partial \bar{z}}\hat{\bar{E}}_n = -\hat{T}^{-1}\hat{R}\,\hat{\Pi}_n \tag{2.99}$$

$$\frac{\partial}{\partial \bar{z}}\hat{\bar{H}}_n = \hat{T}^{-1}\frac{d}{d\bar{z}}\hat{\Pi}_n \tag{2.100}$$

Substituting (2.62) into (2.99) and (2.100) yields:

$$\frac{\partial}{\partial \bar{z}}\hat{\bar{E}}_n = -\hat{\bar{R}}\,\hat{\bar{\Pi}}_n \tag{2.101}$$

$$\frac{\partial}{\partial \bar{z}}\hat{\bar{H}}_n = \frac{d}{d\bar{z}}\hat{\bar{\Pi}}_n \tag{2.102}$$

with $$\hat{\bar{R}} = \hat{T}^{-1}\hat{R}\hat{T}. \tag{2.103}$$

The relation between the electric and magnetic field components on two planes A and B is described by the equation:

$$\begin{bmatrix} \hat{\bar{H}}_{nA} \\ \hat{\bar{H}}_{nB} \end{bmatrix} = \hat{\hat{\Gamma}}^2 \begin{bmatrix} -\hat{\gamma} & \hat{\alpha} \\ -\hat{\alpha} & \hat{\gamma} \end{bmatrix} \begin{bmatrix} \hat{\bar{\Pi}}_{nA} \\ \hat{\bar{\Pi}}_{nB} \end{bmatrix}$$

$$= -\hat{\hat{\Gamma}}^2 \begin{bmatrix} -\hat{\gamma} & \hat{\alpha} \\ -\hat{\alpha} & \hat{\gamma} \end{bmatrix} \begin{bmatrix} \hat{\bar{R}}^{-1} & o \\ o & \hat{\bar{R}}^{-1} \end{bmatrix} \begin{bmatrix} \hat{\bar{E}}_{nA} \\ \hat{\bar{E}}_{nB} \end{bmatrix} \qquad (2.104)$$

with $\hat{\hat{\Gamma}} = Diag\left(\hat{\Gamma},\ \hat{\Gamma}\right)$.

Equation (2.104) is rewritten as:

$$\begin{bmatrix} \hat{\bar{H}}_{nA} \\ \hat{\bar{H}}_{nB} \end{bmatrix} = \begin{bmatrix} \bar{y}_1 & \bar{y}_2 \\ \bar{y}_2 & \bar{y}_1 \end{bmatrix} \begin{bmatrix} \hat{\bar{E}}_{nA} \\ -\hat{\bar{E}}_{nB} \end{bmatrix} \qquad (2.105)$$

with $$\bar{y}_1 = \hat{\Gamma}^2 \hat{\gamma} \hat{\bar{R}}^{-1}$$

$$\bar{y}_2 = \hat{\Gamma}^2 \hat{\alpha} \hat{\bar{R}}^{-1} .$$

In the original domain, the relation between the electric and magnetic field components on two planes A and B is derived from (2.105). It is expressed as:

$$\begin{bmatrix} \hat{H}_{nA} \\ \hat{H}_{nB} \end{bmatrix} = \begin{bmatrix} y_1 & y_2 \\ y_2 & y_1 \end{bmatrix} \begin{bmatrix} \hat{E}_{nA} \\ -\hat{E}_{nB} \end{bmatrix} \qquad (2.106)$$

with

$$y_1 = \hat{T}\,\bar{y}_1\hat{T}^{-1}$$

$$y_2 = \hat{T}\,\bar{y}_2\hat{T}^{-1}.$$

2.2.4 Indirect Eigenvalue Equation

To set up the indirect eigenvalue equation, there is a need to turn to the recurrence relation used in [36] to relate the transverse fields from one layer to the other. The recurrence relation is written as follows:

$$\overline{H}_k = \overline{Y}^{(k)}\overline{E}_k$$

$$\overline{Y}^{(k)} = \bar{y}_2^{(k)}\left(\bar{y}_1^{(k)} - \overline{Y}^{(k-1)}\right)^{-1}\bar{y}_2^{(k)} - \bar{y}_1^{(k)}.$$

In [36], this algorithm is used in the transformed domain. It is correct only in the transformed domain if the layers are homogeneous. Only in this case are the transformation matrices for each layer equal. However, this algorithm does not hold valid if the layers are inhomogeneous. The admittances and fields should be transformed back to the original domain and the algorithm should be used for these quantities.

As a general case, the formulation for the structure is done with inhomogeneous layers, as Fig. 2-3 shows. The formulation is also suitable for the analysis of the structure with homogeneous layers, though a little redundant.

At the matching interface M, the admittance type relationship is obtained from the below layers:

$$\hat{H}^{\mathrm{I}}_{n,M} = Y_t^{\mathrm{I}} \hat{E}^{\mathrm{I}}_{n,M} . \tag{2.107}$$

The matrix Y_t^{I} is constructed by scanning up through layers from substrate to the layer adjoining the matching interface and applying the following recursive equation

$$Y_t^{(k)} = y_2^{(k)} \left[y_1^{(k)} - Y_t^{(k-1)} \right]^{-1} y_2^{(k)} - y_1^{(k)} \tag{2.108}$$

which begins from the substrate with

$$Y_t^{(substrate)} = -y_1^{(substrate)} . \tag{2.109}$$

Here, the substrate thickness may be infinite or finite with a shielded electric wall.

Accordingly, the similar admittance type relationship is achieved from the upper side at the matching interface M:

$$\hat{H}^{\mathrm{II}}_{n,M} = -Y_t^{\mathrm{II}} \hat{E}^{\mathrm{II}}_{n,M} \tag{2.110}$$

The matrix Y_t^{II} is constructed by scanning down through layers from the cover to the layer adjoining the matching interface and applying the following recursive equation

$$Y_t^{(l)} = y_2^{(l)} \left[y_1^{(l)} - Y_t^{(l-1)} \right]^{-1} y_2^{(l)} - y_1^{(l)} \tag{2.111}$$

which begins from the cover with

$$Y_t^{(cover)} = y_1^{(cover)}. \tag{2.112}$$

Again, the cover thickness may be infinite or finite with a shielded electric wall.

Since no electric currents exist in the "matching interface," all tangential field components must be continuous there. Therefore, the boundary conditions

$$\hat{H}^{\mathrm{I}}_{n,M} = \hat{H}^{\mathrm{II}}_{n,M} = \hat{H}_{n,M} \tag{2.113}$$

$$\hat{E}^{\mathrm{I}}_{n,M} = \hat{E}^{\mathrm{II}}_{n,M} = \hat{E}_{n,M} \tag{2.114}$$

must be satisfied. Hence, subtracting (2.110) from (2.107) yields

$$\hat{H}^{\mathrm{I}}_{n,M} - \hat{H}^{\mathrm{II}}_{n,M} = \left(Y_t^{\mathrm{I}} - Y_t^{\mathrm{II}}\right)\hat{E}_{n,M} = Y_{ts}(\varepsilon_{re})\hat{E}_{n,M} = 0. \tag{2.115}$$

(2.115) is the desired characteristic equation, which is an indirect eigenvalue problem for the effective propagation constant.

It is well known from mathematics that a homogeneous linear matrix equation shows nontrivial solutions only when the determinant of the matrix is equal to zero. For solution of the equation given above (2.115) it is accordingly necessary to first solve

$$\det(Y_{ts}(\varepsilon_{re})) = 0. \tag{2.116}$$

This yields the effective propagation constants (ε_{re}) of propagating modes supported by the optical waveguide bend. The effective propagation constant is a complex constant

because of the radiation. The radiation loss is obtained from the imaginary part of $\sqrt{\varepsilon_{re}}$. For a bend with an angle θ (in radian), the radiation loss is expressed by the equation

$$\alpha = 8.68 * \theta * \bar{r}_o * \mathrm{Im}\left(\sqrt{\varepsilon_{re}}\right) \text{ dB.} \tag{2.117}$$

The phase constant is obtained from the real part of $\sqrt{\varepsilon_{re}}$. For some propagating mode with the effective propagation constant ε_{re}, the normalized phase constant is expressed by

$$\beta / k_o = \mathrm{Re}(n_{eff}) = \mathrm{Re}\left(\sqrt{\varepsilon_{re}}\right) \tag{2.118}$$

In equation (2.116), ε_{re} is a complex value, and cannot be determined by a numerical procedure that finds the zeros of (2.116) by means of searching for points where the sign of the determinant changes. Instead, Muller's method must be used to find the complex roots (see Appendix A for the algorithm of Muller's method). Searching by Muller's method has an advantage: the poles of the determinant do not affect it.

The MoL formulation already handles complex quantities due to the radiation loss. Therefore, this algorithm can be used for bends with complex permittivities without any modification in the code.

2.2.5 Interface Conditions

To get a monotonic convergence behavior, the interface conditions at permittivity steps along the radial direction should be taken into consideration. Choosing suitable values for the permittivities in the vicinity of the steps can accomplish this task [26]. However, in certain cases the steps cannot be placed on suitable lines. In the case shown in Fig. 2-3 the step is placed on a Π_φ line. The component in $\bar{\varepsilon}_e$ at the transition from ε_{r1} to ε_{r2} must be chosen according to

$$\varepsilon_{rt} = \frac{\varepsilon_{r1} + \varepsilon_{r2}}{2} + p\,(\varepsilon_{r1} - \varepsilon_{r2}) \tag{2.119}$$

with $\quad -0.5 \le p \le 0.5$.

Here, $\varepsilon_{r1}, \varepsilon_{r2}$ are the permittivities on the left or the right side of the steps, respectively. The term with p allows a shift of the step from the Π_φ line by ph.

2.2.6 Nonequidistant Discretization

To speed up the calculation, nonequidistant discretization is introduced in the formulation. The diagonal normalization matrices are first set up:

$$s_e = \left[\sqrt{\frac{h_{\min}}{e_i}}\right]_{diag} \tag{2.120}$$

$$s_h = \left[\sqrt{\frac{h_{\min}}{h_i}}\right]_{diag} \tag{2.121}$$

$$\hat{s} = diag(s_h, s_e) \tag{2.122}$$

where e_i denotes the spacing between H lines, h_i represents the spacing between E lines, and $h_{\min}$ refers to the line spacing in the equidistant region with rapidly changing fields. Using the above diagonal matrices, a second normalization of the potentials is performed. The fields and the difference operators become:

$$\hat{\Pi}_N = \hat{s}^{-1}\hat{\Pi}_n \tag{2.123}$$

$$\hat{E}_N = \hat{s}^{-1}\hat{E}_n \tag{2.124}$$

$$\hat{H}_N = \hat{s}^{-1}\hat{H}_n \tag{2.125}$$

$$D_{eN} = s_h D_{en} s_e \tag{2.126}$$

$$\overline{D}_{eN} = h_{\min}{}^{-1} D_{eN} \tag{2.127}$$

$$D_{hN} = s_e D_{hn} s_h \tag{2.128}$$

$$\overline{D}_{hN} = h_{\min}{}^{-1} D_{hN} \tag{2.129}$$

These double normalized quantities must be used in the formulation instead of single normalized quantities.

2.2.7 Absorbing Boundary Conditions (ABCs) [39-43]

To analyze the bending loss using MoL, the calculation window must be delimited. But, the use of electric or magnetic walls on the right boundary will produce errors, since the tangential field components there are set to zero and radiation effects cannot be taken into account. To overcome this difficulty, two schemes are employed: one choice is putting the right boundary far away from the waveguide core until its influence is neglected, and the other choice is introducing ABCs on the right side of the calculation window. As a matter of fact, putting the right boundary far away from the waveguide core is not practical, though possible, considering the computing efficiency.

As ABCs will be introduced in D_e (see Fig. 2-3), the formulation will be started from the equation (2.30). Using the operator

$$L = (\sqrt{\bar{r}_n} D\bar{r} \frac{1}{\sqrt{\bar{r}_n}})(\frac{1}{\sqrt{\bar{r}_n}} D\bar{r} \sqrt{\bar{r}_n}) + D\bar{z}^2 + \bar{r}_n^{-2} D_\varphi^2 + \varepsilon_r$$

$$\text{with} \quad D\bar{r} = \frac{d}{d\bar{r}}, \quad D\bar{z}^2 = \frac{d^2}{d\bar{z}^2}, \quad D_\varphi{}^2 = \frac{d^2}{d\varphi^2}$$

(2.30) is rewritten as

$$L\Pi_{\phi n} = L^+ L^- \Pi_{\varphi n} = 0 \tag{2.130}$$

with solutions for the propagating fields in the $+r$ and $-r$ directions in two separate equations:

$$L^+ \Pi_{\varphi n} = 0 \quad \text{and} \quad L^- \Pi_{\varphi n} = 0 \tag{2.131}$$

where

$$L^{+}\Pi_{\varphi n} = (\sqrt{\bar{r}_n} D\bar{r} \frac{1}{\sqrt{\bar{r}_n}} + j\sqrt{\varepsilon_r}\sqrt{1+S^2})\Pi_{\varphi n} = 0 \tag{2.132}$$

$$L^{-}\Pi_{\varphi n} = (\sqrt{\bar{r}_n} D\bar{r} \frac{1}{\sqrt{\bar{r}_n}} - j\sqrt{\varepsilon_r}\sqrt{1+S^2})\Pi_{\varphi n} = 0 \tag{2.133}$$

$$S^2 = \frac{1}{\varepsilon_r}(D\bar{z}^2 + \bar{r}_n^{-2} D_\varphi^2). \tag{2.134}$$

Equation (2.132) describes wave propagation in the $+r$ direction and (2.133) in the $-r$ direction. In this case, only equation (2.132) is needed. The ABCs will be obtained from this equation for the right boundary. The main problem in Eq. (2.132) is the square root with differential operators under the radicand. Therefore, L^{+} is a nonlocal pseudodifferential operator and a direct numerical implementation is not possible. The usual approach [39-41] to overcome this problem is to use the following Padé approximation by the rational function:

$$\sqrt{1+S^2} \approx \frac{p_0 + p_2 S^2}{q_0 + q_2 S^2} \qquad |S^2| < 1 . \tag{2.135}$$

With the above approximation, Eq. (2.132) is rewritten as:

$$\left[-j(q_0 + q_2 S^2)\sqrt{\bar{r}_n} D\bar{r} \frac{1}{\sqrt{\bar{r}_n}} + \sqrt{\varepsilon_r}(p_0 + p_2 S^2)\right]\Pi_{\varphi n} = 0 . \tag{2.136}$$

Combining with Eq.(2.134), the result is:

$$\begin{aligned}&\{-j[q_0+q_2\varepsilon_r^{-1}(D\bar{z}^2+\bar{r}_n^{-2}D_\varphi^2)\,]\sqrt{\bar{r}_n}D\bar{r}\,\frac{1}{\sqrt{\bar{r}_n}}\\&+\sqrt{\varepsilon_r}\left[p_0+p_2\varepsilon_r^{-1}(D\bar{z}^2+\bar{r}_n^{-2}D_\varphi^2)\right]\}\Pi_{\varphi n}=0\end{aligned}\qquad(2.137)$$

Introducing

$$D\bar{z}^2+\bar{r}_n^{-2}D_\varphi^2=-\varepsilon_r-(\sqrt{\bar{r}_n}D\bar{r}\,\frac{1}{\sqrt{\bar{r}_n}})(\frac{1}{\sqrt{\bar{r}_n}}D\bar{r}\sqrt{\bar{r}_n})$$

from the wave equation (2.30) and using it in (2.137) yields:

$$\begin{aligned}&\Big\{-q_2(\sqrt{\bar{r}_n}D\bar{r}\,\frac{1}{\sqrt{\bar{r}_n}})(\frac{1}{\sqrt{\bar{r}_n}}D\bar{r}\,\sqrt{\bar{r}_n})(\sqrt{\bar{r}_n}D\bar{r}\,\frac{1}{\sqrt{\bar{r}_n}})\\&-jp_2\sqrt{\varepsilon_r}(\sqrt{\bar{r}_n}D\bar{r}\,\frac{1}{\sqrt{\bar{r}_n}})(\frac{1}{\sqrt{\bar{r}_n}}D\bar{r}\,\sqrt{\bar{r}_n})\\&+[(1-q_2)]\varepsilon_r(\sqrt{\bar{r}_n}D\bar{r}\,\frac{1}{\sqrt{\bar{r}_n}})-j(p_2-p_0)\varepsilon_r^{3/2}\Big\}\Pi_{\varphi n}=0\end{aligned}\qquad(2.138)$$

Discretizing the above equation on line N by using Taylor series at this line to obtain the potential on the neighborhood lines gives the following result:

$$\sqrt{\bar{r}_{e,N+1}}\Pi_{\varphi,N+1}=\frac{C_N}{C_{N+1}}\sqrt{\bar{r}_{e,N}}\Pi_{\varphi,N}+\frac{C_{N-1}}{C_{N+1}}\sqrt{\bar{r}_{e,N-1}}\Pi_{\varphi,N-1}+\frac{C_{N-2}}{C_{N+1}}\sqrt{\bar{r}_{e,N-2}}\Pi_{\varphi,N-2}\qquad(2.139)$$

$$C_{N+1} = p_2 \sqrt{\bar{r}_{e,N}}\, \bar{r}_{h,N}{}^{-1} \sqrt{\bar{r}_{h,N-1}}^{-1} + \frac{1}{3}(1-q_2)\bar{n}_a \bar{r}_{e,N+1}{}^{-1} + \bar{n}_a{}^{-1} q_2 \bar{r}_{h,N} \bar{r}_{e,N}{}^{-1} \bar{r}_{e,N+1}{}^{-1}$$

$$C_N = p_2 \sqrt{\bar{r}_{e,N}} \sqrt{\bar{r}_{h,N-1}}^{-1} (\bar{r}_{h,N}{}^{-1} + \bar{r}_{h,N-1}{}^{-1}) - \frac{1}{2}(1-q_2)\bar{n}_a \bar{r}_{e,N}{}^{-1}$$
$$+ \bar{n}_a{}^2 (p_2 - p_0) \sqrt{\bar{r}_{e,N}}^{-1} \sqrt{\bar{r}_{h,N-1}}^{-1}$$
$$+ (\bar{r}_{e,N}{}^{-1} \bar{r}_{e,N}{}^{-1} \bar{r}_{h,N} + \bar{r}_{e,N}{}^{-1} \bar{r}_{e,N}{}^{-1} \bar{r}_{h,N-1} + \bar{r}_{e,N}{}^{-1} \bar{r}_{e,N-1}{}^{-1} \bar{r}_{h,N-1}) \bar{n}_a{}^{-1} q_2$$

$$C_{N-1} = -p_2 \sqrt{\bar{r}_{e,N}} \sqrt{\bar{r}_{h,N-1}}^{-1} \bar{r}_{h,N-1}{}^{-1} + (1-q_2)\bar{n}_a \bar{r}_{e,N-1}{}^{-1}$$
$$- \bar{n}_a{}^{-1} q_2 (\bar{r}_{e,N-1}{}^{-1} \bar{r}_{e,N}{}^{-1} \bar{r}_{h,N-1} + \bar{r}_{e,N-1}{}^{-1} \bar{r}_{e,N-1}{}^{-1} \bar{r}_{h,N-1} + \bar{r}_{e,N-1}{}^{-1} \bar{r}_{e,N-1}{}^{-1} \bar{r}_{h,N-2})$$

$$C_{N-2} = -\frac{1}{6}(1-q_2)\bar{n}_a \frac{1}{\bar{r}_{e,N-2}} + \bar{n}_a{}^{-1} q_2 \bar{r}_{e,N-1}{}^{-1} \bar{r}_{e,N-2}{}^{-1} \bar{r}_{h,N-2}$$

with the abbreviation $\bar{n}_a = j\bar{h}\sqrt{\varepsilon_r}$ and where without loss of generality $q_0 = 1$ is introduced. From the above equations, the coefficients a, b and c in the expression for D_e (see 2.2.2) are found:

$$a = -\frac{C_N}{C_{N+1}} \tag{2.140}$$

$$b = \frac{C_{N-1}}{C_{N+1}} \tag{2.141}$$

$$c = \frac{C_{N-2}}{C_{N+1}} \tag{2.142}$$

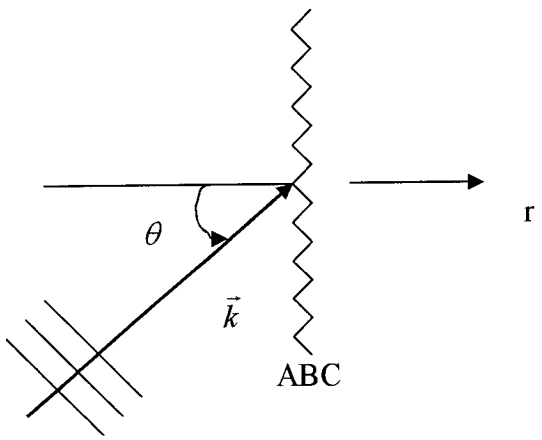

Fig. 2-4 Field wave reaches the ABC at the angle of incidence θ

Three parameters p_0, p_2 and q_2 are determined by choosing three angles with total absorption. According to [40], the reflection coefficient at the boundary is given by

$$R = \frac{\cos\theta - q_2 \cos\theta \sin^2\theta - p_0 + p_2 \sin^2\theta}{\cos\theta - q_2 \cos\theta \sin^2\theta + p_0 - p_2 \sin^2\theta} . \tag{2.143}$$

Therefore, with $R = 0$ for three chosen angles θ_1, θ_2 and θ_3, the coefficients can be obtained [41]:

$$\begin{bmatrix} 1 & -\sin^2\theta_1 & \cos\theta_1 \sin^2\theta_1 \\ 1 & -\sin^2\theta_2 & \cos\theta_2 \sin^2\theta_2 \\ 1 & -\sin^2\theta_3 & \cos\theta_3 \sin^2\theta_3 \end{bmatrix} \begin{bmatrix} p_0 \\ p_2 \\ q_2 \end{bmatrix} = \begin{bmatrix} \cos\theta_1 \\ \cos\theta_2 \\ \cos\theta_3 \end{bmatrix} \tag{2.144}$$

the above has the solution:

$$q_2 = (\cos\theta_1 \cos\theta_2 + \cos\theta_1 \cos\theta_3 + \cos\theta_2 \cos\theta_3)^{-1} \tag{2.145}$$

$$p_0 = (\cos\theta_1 + \cos\theta_2 + \cos\theta_3 + \cos\theta_1 \cos\theta_2 \cos\theta_3) q_2 \tag{2.146}$$

$$p_2 = (\cos\theta_1 + \cos\theta_2 + \cos\theta_3) q_2 . \tag{2.147}$$

As the radiation loss is tangential [2], the three angles θ_1, θ_2 and θ_3 should be chosen to be nearly 90 degrees.

2.3 Field Distribution

2.3.1 One-Dimension Distribution [38]

The analysis begins with Eg. (2.115), which is a homogenous matrix problem. Here, Y_{ts} is a $2N \times 2N$ square matrix. An infinity of nontrivial solutions exists for $\hat{E}_{n,M}$ only if Y_{ts} is singular. Thus, if Y_{ts} is singular, there exists a basis of 2N-dimensional vectors (with at least one vector) that expresses all possible solutions for $\hat{E}_{n,M}$.

Singular Value Decomposition (SVD) is the formal approach used to solve a homogeneous matrix problem. SVD determines both the null-space basis and the range basis. The SVD of Y_{ts} is expressed by

$$Y_{ts} = \hat{U}[\omega]_{diag}\hat{V}^T . \tag{2.148}$$

Here, both $\hat{U}$ and $\hat{V}$ are super orthonormal matrices: i.e $\hat{U}\hat{U}^T = I$ and $\hat{V}\hat{V}^T = I$. $[\omega]_{diag}$ is a diagonal matrix which contains the singular values ω_i of Y_{ts} in decreasing order of magnitude: $|\omega_i| > |\omega_{i+1}|$ and ω_{2N} is the smallest singular value. If Y_{ts} is singular then at least one singular value ω_{2N} will be null. In this case, only the last singular value is null.

The last column vector of $\hat{V}$ which corresponds to the last null singular value is the vector that defines the null-space basis. An infinity of solutions for $\hat{E}_{n,M}$ exists, since any constant times this basis vector is a valid solution. Physically, a constant attributes different power levels to the computed mode. Interest only lies in the field distribution. Without loss of generality, if $\hat{V} = [\overline{V}_1, \overline{V}_2, \ldots, \overline{V}_{2N-1}, \overline{V}_{2N}]$ where $\overline{V}_i (1 \le i \le 2N)$ is a column vector $(2N \times 1)$, then $\hat{E}_{n,M}$ is expressed by the null-space basis, namely the last column vector in $\hat{V}$, i.e.

$$\hat{E}_{n,M} = \overline{V}_{2N} \tag{2.149}$$

According to Eq. (2.107) or (2.110), $\hat{H}_{n,M}$ is obtained by

$$\hat{H}_{n,M} = Y_t^1 \hat{E}_{n,M}$$

or $$\hat{H}_{n,M} = -Y_t^{\Pi}\hat{E}_{n,M}. \tag{2.150}$$

From Eq. (2.95) and (2.96), the following results

$$\hat{\Pi}_{n,M} = -\hat{R}^{-1}\hat{E}_{n,M} \tag{2.151}$$

$$\frac{d}{d\bar{z}}\hat{\Pi}_{n,M} = \hat{H}_{n,M} \tag{2.152}$$

where $\hat{R}$ takes the value in the upper or lower layer adjoining the matching interface.

Starting from Eq. (2.23) and (2.26), the following results

$$\varepsilon_r E_{zn} = \frac{\partial}{\partial\bar{z}}\left[\frac{1}{\bar{r}_n}\frac{1}{\sqrt{\bar{r}_n}}\frac{\partial}{\partial\bar{r}}(\sqrt{\bar{r}_n}\,\Pi_{rn}) - \frac{j\sqrt{\varepsilon_{re}}}{\bar{r}_n}\Pi_{\varphi n}\right] \tag{2.153}$$

$$\eta_o H_{zn} = j\left[\frac{1}{\bar{r}_n}\frac{1}{\sqrt{\bar{r}_n}}\frac{\partial}{\partial\bar{r}}(\sqrt{\bar{r}_n}\,\Pi_{\varphi n}) + \frac{j\sqrt{\varepsilon_{re}}}{\bar{r}_n}\Pi_{rn}\right]. \tag{2.154}$$

To facilitate the coding, (2.153) and (2.154) is written in matrices respectively

$$E_{zn} = \varepsilon_r^{-1}[\bar{D}_{hn} \quad \sqrt{\varepsilon_{re}}\,\bar{r}_e^{-1}] * \bar{H}_{n,M} \tag{2.155}$$

$$H_{zn} = \eta_0^{-1}[\sqrt{\varepsilon_{re}}\bar{r}_h^{-1} \quad \bar{D}_{en}] * (-\hat{\Pi}_{n,M}) \tag{2.156}$$

If $\hat{E}_{n,M}$ and $\hat{H}_{n,M}$ are written as $\hat{E}_{n,M} = [E_1 E_2 E_3 \cdots E_{N-1} E_N E_{N+1} \cdots E_{2N-1} E_{2N}]^T$, and $\hat{H}_{n,M} = [H_1 H_2 H_3 \cdots H_{N-1} H_N H_{N+1} \cdots H_{2N-1} H_{2N}]^T$, transverse field components on the matching interface are expressed by

$$\hat{E}_{n,M} = [E_1 E_2 E_3 \cdots E_{N-1} E_N]^T \tag{2.157}$$

$$E_{\varphi n,M} = j[E_{N+1} \cdots E_{2N-1} E_{2N}]^T \tag{2.158}$$

$$H_{rn,M} = \eta_0^{-1}[H_1 H_2 H_3 \cdots H_{N-1} H_N]^T \tag{2.159}$$

$$H_{\varphi n,M} = j\eta_0^{-1}[H_{N+1} \cdots H_{2N-1} H_{2N}]^T . \tag{2.160}$$

Next, denormalization with respect to the six fields will be done according to

$$E_{r,M} = \sqrt{\bar{r}_h}^{-1} E_{rn,M} \tag{2.161}$$

$$E_{\varphi,M} = \sqrt{\bar{r}_e}^{-1} E_{\varphi n,M} \tag{2.162}$$

$$E_z = \sqrt{\bar{r}_e}^{-1} E_{zn} \tag{2.163}$$

$$H_{r,M} = \sqrt{\bar{r}_e}^{-1} H_{rn,M} \tag{2.164}$$

$$H_{\varphi,M} = \sqrt{\bar{r}_h}^{-1} H_{\varphi n,M} \tag{2.165}$$

$$H_{z,M} = \sqrt{\bar{r}_h}^{-1} H_{zn,M} . \tag{2.166}$$

The corresponding relative values of the above fields are obtained by

$$E_{r,M} = E_{r,M} / E_{\max} \tag{2.167}$$

$$E_{\varphi,M} = E_{\varphi,M} / E_{\max} \tag{2.168}$$

$$E_z = E_z / E_{\max} \tag{2.169}$$

$$H_{r,M} = H_{r,M} / E_{\max} \tag{2.170}$$

$$H_{\varphi,M} = H_{\varphi,M} / E_{\max} \tag{2.171}$$

$$H_{z,M} = H_{z,M} / E_{\max} \tag{2.172}$$

with

$$E_{\max} = \max(|E_{r,M}|) \qquad \text{for quasi-TE mode}$$

$$E_{\max} = \max(|E_z|). \qquad \text{for quasi-TM mode}$$

2.3.2 Two-Dimension Spatial Distribution

Starting from the one-dimensional field distribution on the matching interface, the two-dimensional field distribution is obtained. The idea is to scan the entire structure layer after layer, up from the matching interface to the cover or down from the matching interface to the substrate. The top or bottom boundary of one layer is the start for the calculation of another layer. For the interface between layers, the quantities in the physical domain must be used to match the boundary conditions. Besides, E_z is not continuous at the interface between two layers and can only be obtained from above or below the interface.

The following demonstrates the formulation of two-dimensional field distribution when scanning up from the layer adjoining the matching interface. After obtaining $\hat{\Pi}_{n,M}$ and $\frac{d}{d\bar{z}}\hat{\Pi}_{n,M}$, they are transferred into the transformation domain according to

$$\hat{\bar{\Pi}}_{n,M} = \hat{T}^{-1}\hat{\Pi}_{n,M} \text{ and } \frac{d}{d\bar{z}}\hat{\bar{\Pi}}_{n,M} = \hat{T}^{-1}\frac{d}{d\bar{z}}\hat{\Pi}_{n,M}.$$

The layer is discretized along z into many sublayers each having a thickness $\Delta\bar{z}$ and at the "i^{th}" sublayer, the following results:

$$\hat{\bar{\Pi}}_{n,M}(i) = \cosh[\hat{\Gamma}(i\Delta\bar{z})]\hat{\bar{\Pi}}_{n,M} + \sinh[\hat{\Gamma}(i\Delta\bar{z})]\frac{d}{d\bar{z}}\hat{\bar{\Pi}}_{n,M} \tag{2.173}$$

$$\frac{d}{d\bar{z}}\hat{\bar{\Pi}}_{n,M}(i) = \sinh[\hat{\Gamma}(i\Delta\bar{z})]\hat{\Gamma}\hat{\bar{\Pi}}_{n,M} + \cosh[\hat{\Gamma}(i\Delta\bar{z})]\hat{\Gamma}\frac{d}{d\bar{z}}\hat{\bar{\Pi}}_{n,M} \tag{2.174}$$

$$\hat{\bar{E}}_n(i) = -\hat{\bar{R}}\,\hat{\bar{\Pi}}_n(i) \tag{2.175}$$

$$\hat{\bar{H}}_n(i) = \frac{d}{d\bar{z}}\hat{\bar{\Pi}}_n(i) \tag{2.176}$$

$$\hat{E}_n(i) = \hat{T}\,\hat{\bar{E}}_n(i) \tag{2.177}$$

$$\hat{H}_n(i) = \hat{T}\,\hat{\bar{H}}_n(i) \tag{2.178}$$

$$E_{zn}(i) = \varepsilon_r^{-1}[\bar{D}_{hn} \quad \sqrt{\varepsilon_{re}}\,\bar{r}_e^{-1}] * \frac{d}{d\bar{z}}\hat{\Pi}_{n,M}(i) \tag{2.179}$$

$$H_{zn}(i) = \eta_0^{-1}[\sqrt{\varepsilon_{re}}\,\bar{r}_h^{-1} \quad \bar{D}_{en}] * (-\hat{\Pi}_{n,M}(i)) \tag{2.180}$$

After the calculation within one layer is finished, scanning of the next layer begins using this top interface as the starting boundary and the procedure mentioned above is repeated. When the calculation on the entire structure is finished, the denormalization is done and the corresponding relative value using the equations analogous to (2.161 to 2.172) is obtained.

2.4 Transition Loss

The transition loss is obtained from the overlap integral between waveguides of different curvature. As the junction of straight waveguide and curved waveguide is the most common case in integrated optics, the analysis for this case will be given. For the junction of waveguides of different curvature, the analysis is very similar. In this formulation, assuming the radius to be infinite, the mode and its two-dimensional field distribution is obtained for the straight case. After obtaining the two dimensional field distribution for the curved waveguide, the transition loss [12][14][53] for the TM case is estimated:

Transition Loss (dB)=

$$10\log_{10}\times\left(\frac{4}{(1+\beta^{cv}/\beta^{st})^2}\times\frac{\left|\int E_z^{st}(r,z)E_z^{cv}(r,z)drdz\right|^2}{\int\left|E_z^{st}(r,z)\right|^2drdz\int\left|E_z^{cv}(r,z)\right|^2drdz}\right)$$

$$=10\log_{10}\left(\frac{4}{(1+\beta^{cv}/\beta^{st})^2}\times\frac{\left|\sum_{j=1}^{M}\sum_{i=1}^{N}E_z^{st}(i,j)E_z^{cv}(i,j)\right|^2}{\sum_{j=1}^{M}\sum_{i=1}^{N}\left|E_z^{st}(i,j)\right|^2\times\sum_{j=1}^{M}\sum_{i=1}^{N}\left|E_z^{cv}(i,j)\right|^2}\right). \qquad (2.181)$$

Equation (2.181) is for the straight-bend junction, where β^{st} and β^{cv} are the propagation constants of the straight and bent waveguides, respectively, and E_z^{st} and E_z^{cv} are the corresponding normalized modal fields. When the mode is searched or the modal distribution is calculated, the absorbing boundary (AB) is placed on the right side of the calculation window. There is no problem for the calculation of the integral in the numerator in (2.181), but the AB will introduce some error in calculating the integral of the denominator since the integral should include all the modal distribution and the latter is not normalizable for a radiative field. The nonradiative modal distribution is used instead of the radiative modal distribution for the calculation of the integral in the denominator in (2.181). The nonradiative modal distribution is obtained by placing an electric wall (EW) boundary condition instead of AB on the right boundary of the calculation window. Obviously, this practice will also cause some inaccuracy, but it has been shown sufficiently accurate for device design [23]. Besides, the bend-to-straight junction can also be computed using (2.181) with β^{st} and β^{cv} interchanged [53].

For TE mode, the dominant transverse electric field E_r should be used, instead of E_z in (2.181).

Chapter 3

Validation

3.1 Introduction

In Chapter 2, the detailed formulation for waveguide bend induced radiation loss, bend transition loss, and field distributions etc. is given using the cylindrical-MOL. This chapter will verify the code implemented by Matlab. The code will be validated by comparing the simulation results obtained from it with those appearing in some other papers.

First, the results shown in Pregla's paper [25] are reproduced. Thus, the code regarding the formulation for the radiation loss and the absorbing boundary conditions can be verified. Furthermore, the one-dimensional and two-dimensional field distributions for quasi-TE and quasi-TM modes are shown.

Second, the code is applied to model the structure given in [19][23]. In [19], T. Yamamoto and M. Koshiba analyze the radiation loss using the Finite-Element Method (FEM); furthermore, they compare their results with those obtained from experiments and the semi-vectorial MoL [21]. In [23], S. Kim and A. Gopinath analyze the same structure and give the results of the radiation loss and transition loss. In addition to those, S. Kim

and A. Gopinath also present optimal lateral offsets for this structure. To further verify the code, these results will be computed and compared with others.

3.2 Validation I

3.2.1 Reproduction of Pregla's results

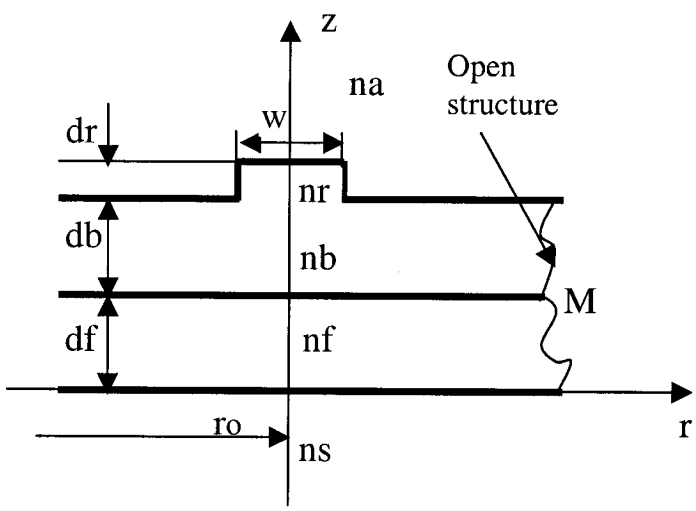

Fig. 3-1 A general rib waveguide bend cross-section

(A) Structure parameters (see Fig. 3-1)

Table 3-1 Dimension parameters of Pregla's structure

rib width (w)	rib height (dr)	film thickness (df)	buffer layer thickness (db)
2.9 μm	0.32 μm or 0.33 μm	1.12 μm	0 μm

Table 3-2 Refractive indices of the layers in Pregla's structure at $\lambda = 1.52\ \mu$ m

cover (na)	rib (nr)	film (nf)	buffer layer (nb)	substrate (ns)
1	3.3735	3.3735	3.3735	3.3042

(B) Size of the computation window

For comparison, the same computation window is taken as Pregla shows in his paper, i.e.: the distance between the left boundary and the middle of the rib is $8\ \mu$ m, and the distance between the right boundary and the middle of the rib is $12\ \mu$ m.

(C) Lines on the rib

When the size of the computation window is set up, a determination is made as to how many E- lines should be put on the rib. Table 3-3 and Table 3-4 are the results obtained for TE mode and TM mode when different lines are put on the rib.

Table 3-3 Radiation loss (dr=0.32 μ m, ro=2mm)

E-lines on rib	10 lines	20 lines	30 lines	40 lines
TE	13.1602 dB	13.8562 dB	14.0283 dB	14.0782 dB

Table 3-4 Radiation loss (dr=0.33 μ m, ro=2mm)

E-lines on rib	10 lines	20 lines	30 lines	40 lines
TM	5.17596 dB	4.92683 dB	4.89458 dB	4.88734 dB

From the results above, it is shown that the simulation results are stable when about 20 E-lines or more are placed on the rib. The following simulation results are obtained by putting 20 E-lines on the rib.

(D) Reproduction of Pregla's results [25]

In [25], Pregla shows the radiation loss of a 90° bend as function of bend radius (r_o) for TE mode (dr=0.32 μm or 0.33 μm) and TM mode (dr=0.33 μm); furthermore, he compares his results with Deri's experimental results [44]. Besides, he also shows the dominant TE mode field distributions of the bend (2mm radius) at the middle of the guided film with the thickness df.

The numerical results are shown in Fig. 3-2. Amongst Fig. 3-2, (a) and (b) represent radiation losses of TE mode versus radius with dr=0.32 μm and dr=0.33 μm, respectively. Figure 3-2(e) shows radiation losses versus radius with dr=0.33 μm (TM mode). In these figures, the solid line represents the results obtained from the code, while the triangle symbol represents the results shown by Pregla. Figure 3-2(c) shows radiation losses versus radius with different rib heights (TE mode), where the solid line represents the results with dr=0.32 μm and the dashed line represents the results with dr=0.33 μm. The numerical results shown in Fig. 3-2(c) agree with the theoretical analysis: the higher the rib, the lower radiation loss. Fig. 3-2(d) and Fig. 3-2(f) show the comparison between the numerical results and Deri's experimental results [44], where the solid line represents the numerical results and the circle symbol represents the experimental results.

Figure 3-3 shows the dominant field distributions of the TE mode of the bend with dr=0.32 μ m. Er and Hz are normalized to the peak value of Er. Figure 3-3 (a) and (b) give the same field distribution for Er and Hz as Pregla shows in his paper [25].

From numerical results given in Fig.3-2 and Fig.3-3, it is believed that the formulation and the code work.

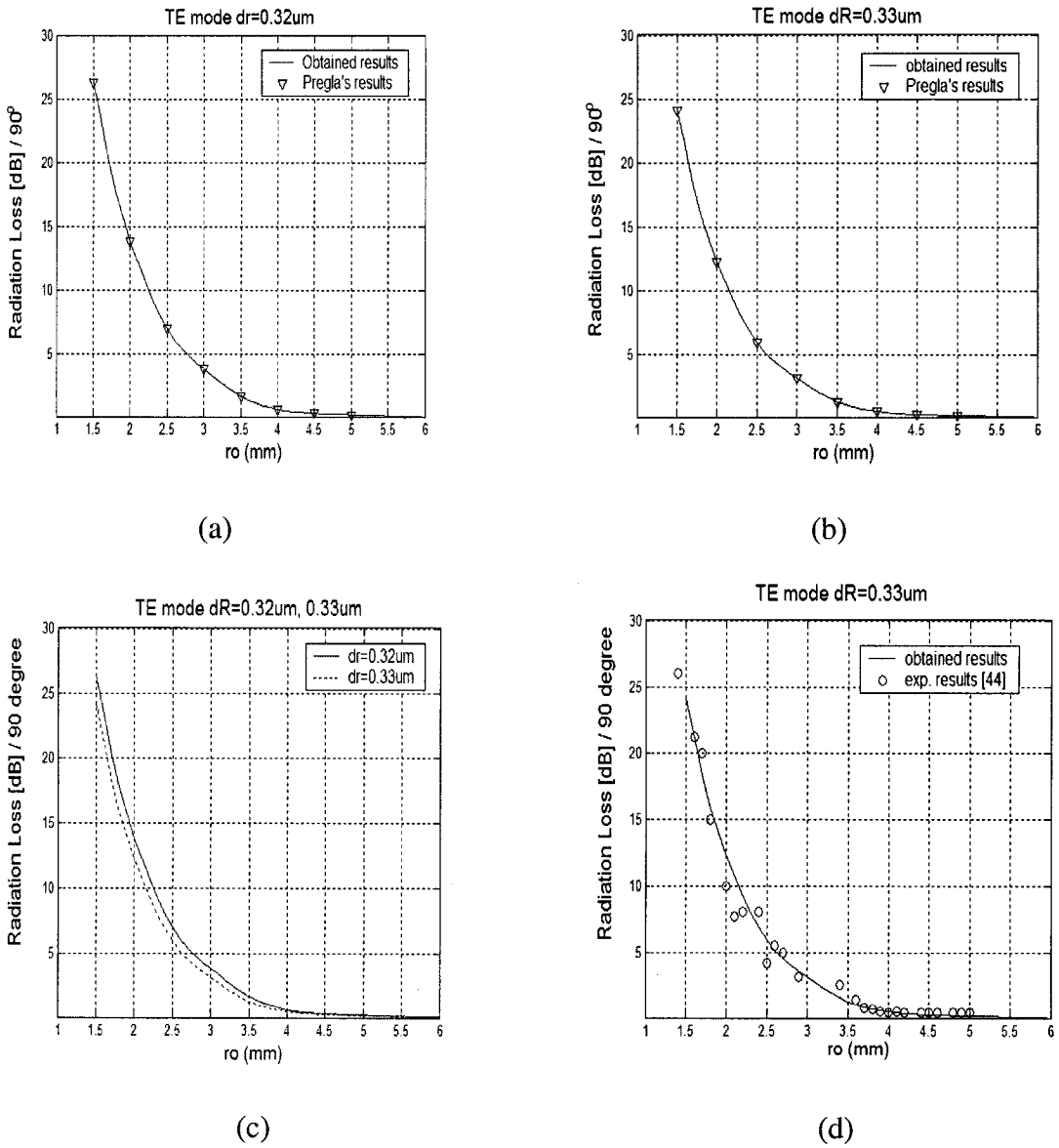

Fig. 3-2 continues from page 51- page52.

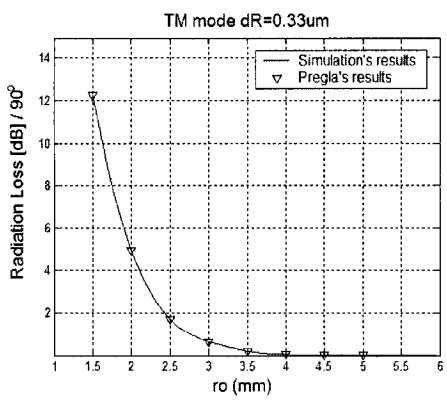

(e)

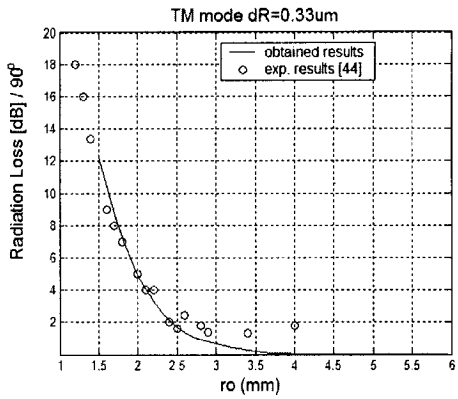

(f)

Fig. 3-2 Radiation loss versus radius, where (a) to (d) are for the TE mode of the bend structure with dr=0.32 μm or 0.33 μm and (e) to (f) are for the TM mode of the bend structure with dr=0.33 μm. The solid or dashed lines represent the numerical results and the triangle or circle symbol represents results from Pregla [25] or the experiment [44], respectively.

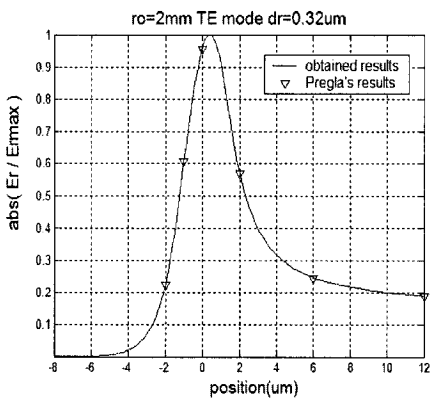

(a)

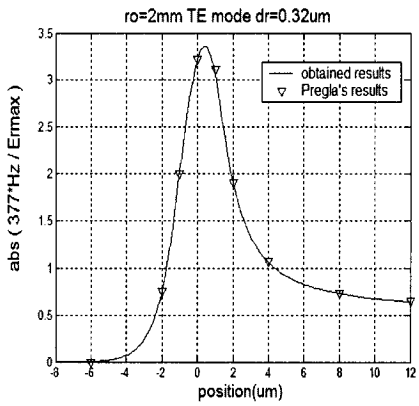

(b)

Fig. 3-3 Normalized dominant field distributions of the TE mode of the bend structure with dr=0.32 μm (in the middle of the guided film). (a) is for $\left|E_r / E_{r,\max}\right|$ and (b) is for $\left|\eta_0 * H_z / E_{r,\max}\right|$, where $\eta_0 = \sqrt{\mu_0/\varepsilon_0} \approx 377\,\Omega$. The solid lines represent the numerical results and the triangle symbol represents results from Pregla's paper [25].

(E) Normalized phase constants

Figure 3-4 shows the numerical results for normalized phase constants (β/β_o). Fig. 3-4 (a) gives the results for the TE mode of the bend structure with dr=0.32μm or 0.33μm and Fig. 3-4 (b) presents the results for the TM mode of the bend structure with dr=0.32μm or 0.33μm. It is found that there is a bending-induced increase of the normalized phase constant for the bent waveguide. The smaller the radius of curvature, the bigger the increase of the normalized phase constant, and as the radius of curvature increases, the normalized phase constant of the bend tends to be that of the straight waveguide asymptotically. The numerical results for the normalized phase constant are consistent with the prediction in [10], discussion in [3] and derivation in [1]. According to [1][3][10], the perturbation to the phase constant in bent symmetric waveguides is expressed by: $\Delta\beta = \beta_{bend} - \beta_{straight} = B/R^2$, where B is a positive constant which depends on the wavelength and waveguide structure parameters; R is the radius of the curvature. The bending-induced increase of the phase constant is simply interpreted as follows: a bent waveguide structure can be treated as an equivalent straight waveguide with modified index profile after conformal mapping [12] and the outer side presents higher refractive index than the inner side. It is well known that the electromagnetic waves moves from the media with lower refractive index to the media with higher refractive index and therefore the fields will shift outward. More fields being confined in higher refractive index will certainly result in the increase of the phase constant.

3.2.2 Field distributions

(A) 1D field distributions

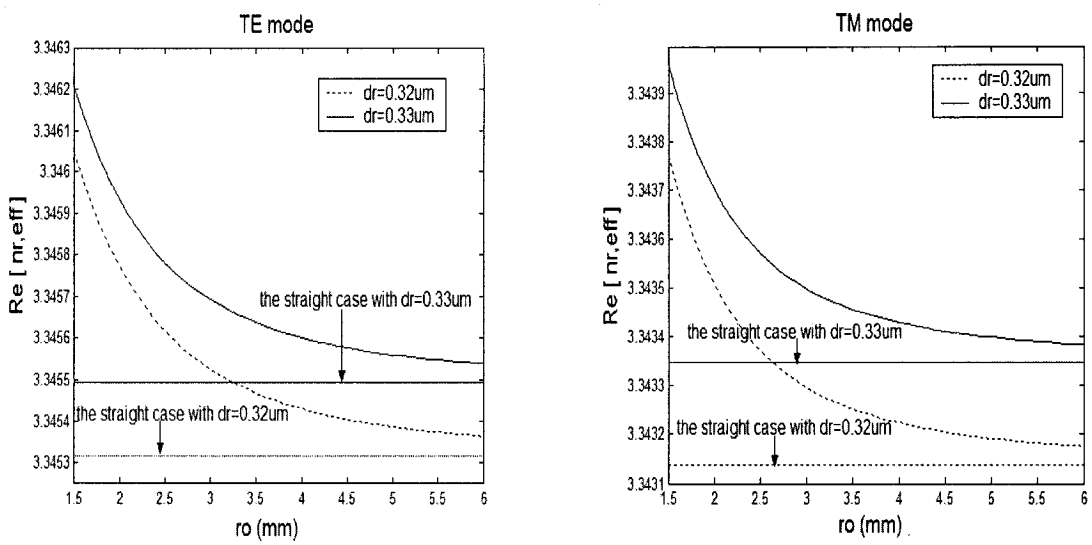

(a) (b)

Fig.3-4 Normalized phase constants for the bent waveguide structure. (a) is for the TE mode of the bent waveguide structure with dr=0.32 μm or 0.33 μm and (b) is for the TM mode of the bent waveguide structure with dr=0.32 μm or 0.33 μm.

Figure 3-5 gives six 1D normalized field distributions for the TE mode of the bent waveguide structure with dr=0.32 μm and radius=1m, while Fig.3-6 presents six 1D normalized field distributions for the TM mode of the bent waveguide structure with dr=0.33 μm and radius=1m. These fields are obtained in the middle of the guided film and can be treated as the field distributions of the straight rib waveguide due to the large radius of curvature. It is easily seen that the electric field Er and the magnetic field Hz are dominant fields for TE mode and the magnetic field Hr and the electric field Ez are dominant fields for TM mode. It is also observed that all the fields of TE mode or TM mode with the radius of the bent structure being 1m (this case can be thought to be the straight waveguide) are symmetric about the vertical axis. Six field distributions are

normalized to the peak value of the real part of the dominant electric field, i.e. Er for TE mode, and Ez for TM mode, respectively.

Figure 3-7 and Fig. 3-8 show the change of 1D normalized dominant electric field distributions of the TE or the TM mode. Fig. 3-7 (a) to Fig. 3-7(d) or Fig. 3-8 (a) to Fig. 3-8 (d) correspond to four cases of different radii of curvature, i.e. 6mm,3mm,2mm, and 1.5mm. All fields are normalized to their peak values. It is found that the field is actually propagating toward the $+r$ direction when the radius of curvature is small, which results in the radiation loss, and that the bending shifts the modal field peak radially outward: the smaller the radius, the greater the shifting. It is also observed that the shifting makes the fields more asymmetric for a smaller bend radius.

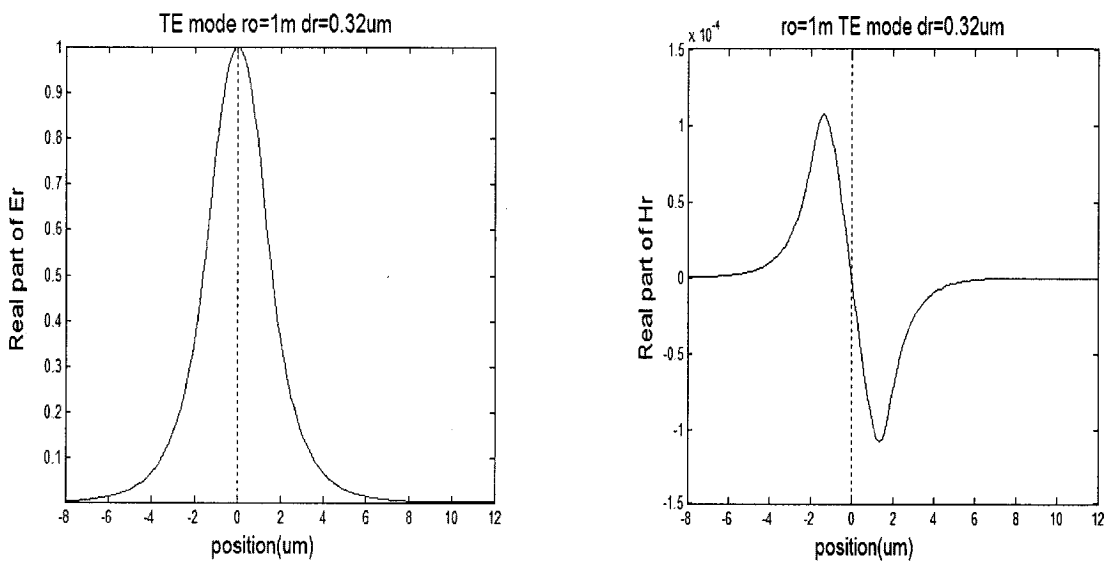

(a) (b)

Fig. 3-5 continues from page 55- page56.

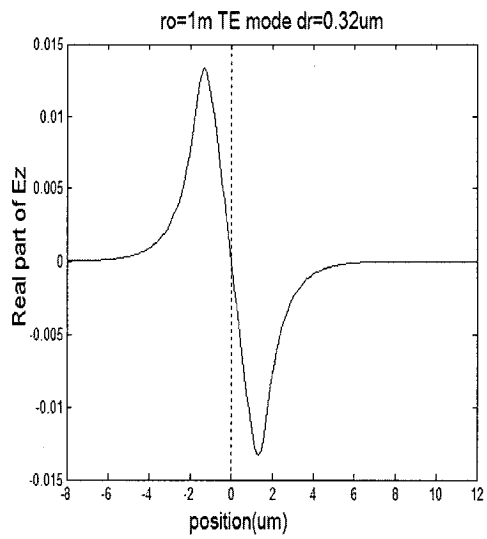

(c)

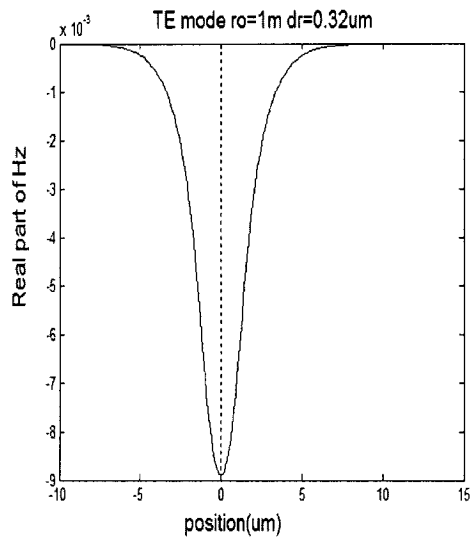

(d)

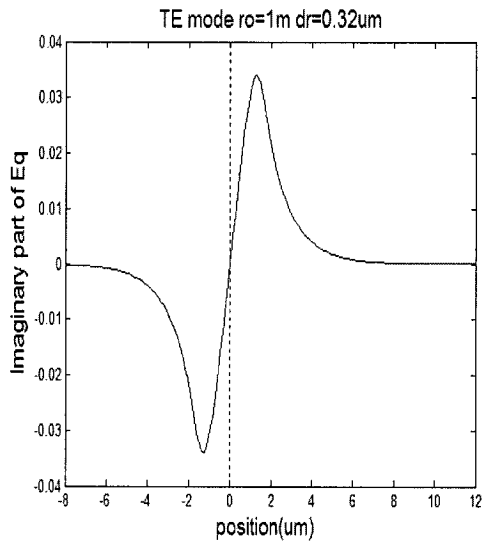

(e)

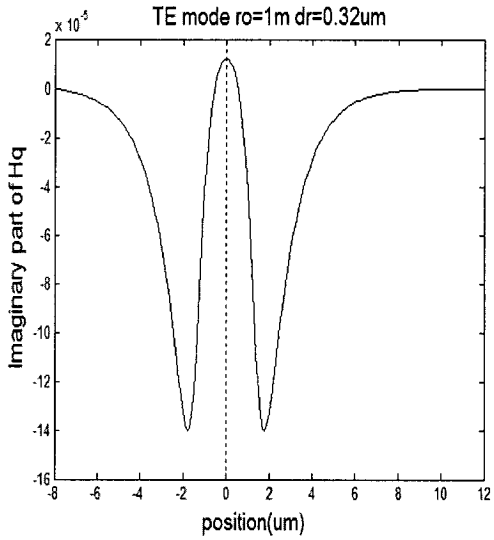

(f)

Fig. 3-5 Six normalized 1D field distributions of the TE mode of the bent rib waveguide (radius=1m) with dr=0.32 μ m, where the distributions are normalized to the peak value of the real part of Er.

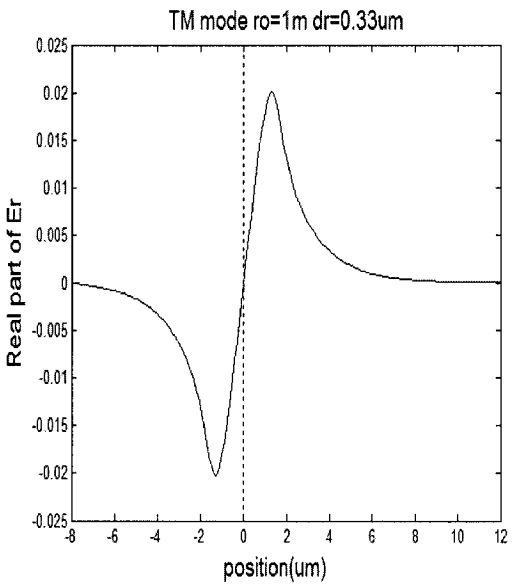

(a)

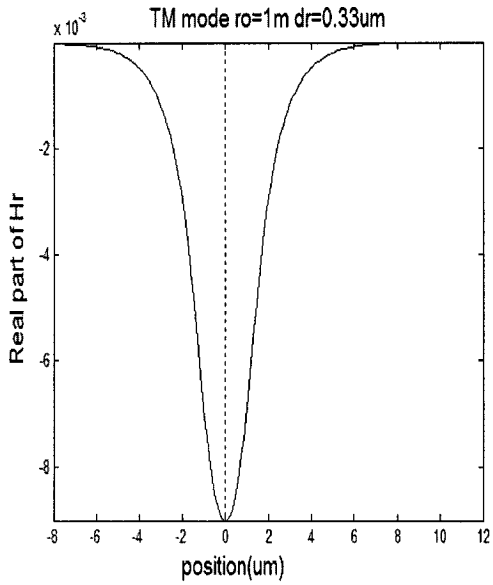

(b)

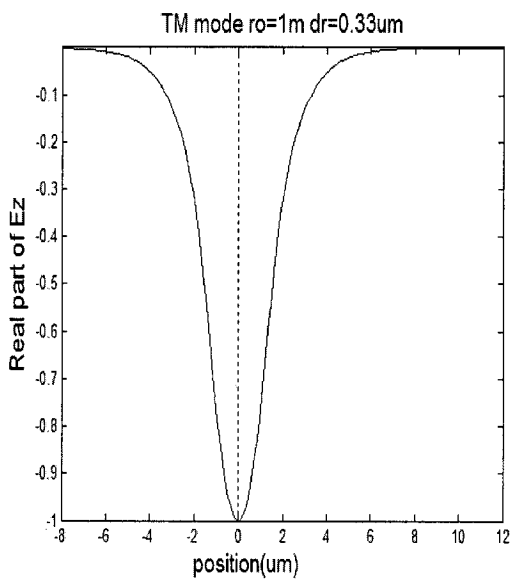

(c)

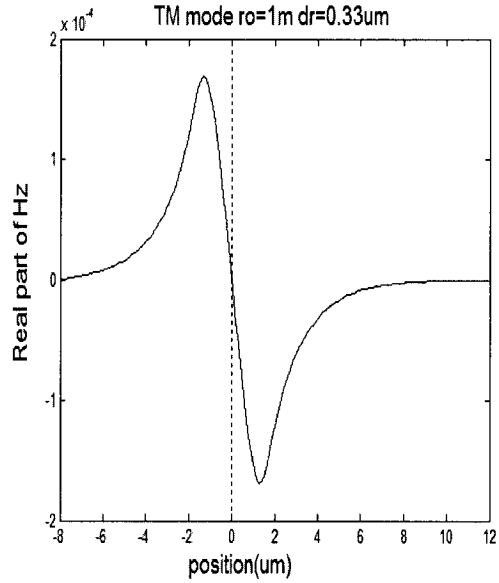

(d)

Fig. 3-6 continues from page 57- page58.

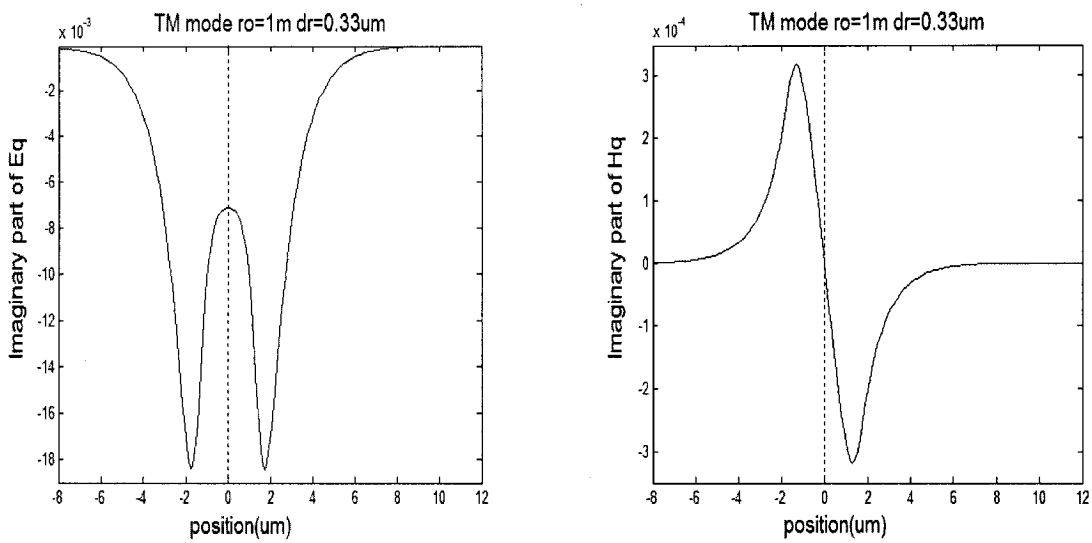

(e) (f)

Fig. 3-6 Six normalized 1D field distributions of the TM mode of the bent rib waveguide (radius=1m) with dr=0.33 μ m, where the distributions are normalized to the peak value of the real part of Ez.

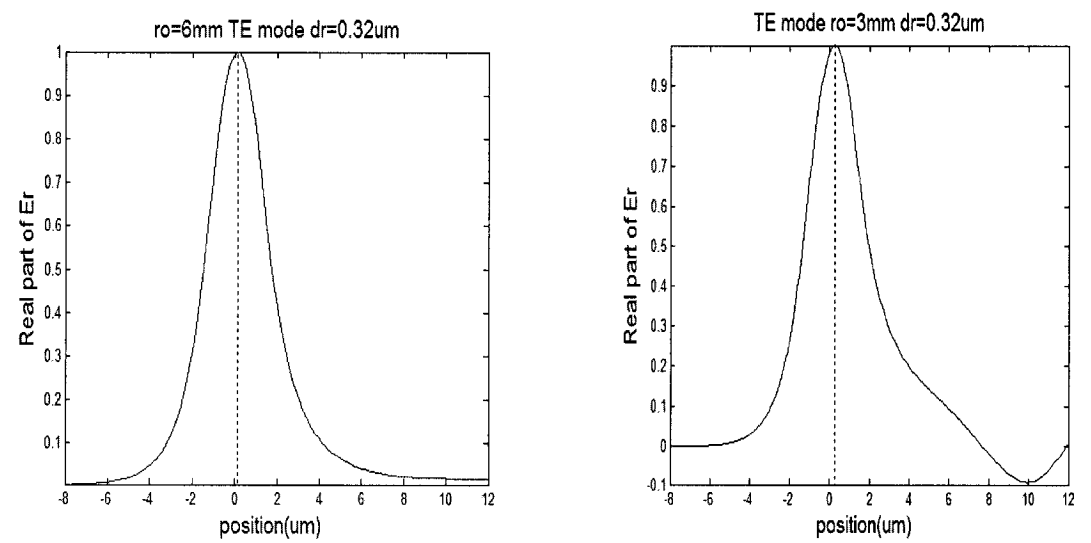

(a) (b)

Fig. 3-7 continues from page 58- page59.

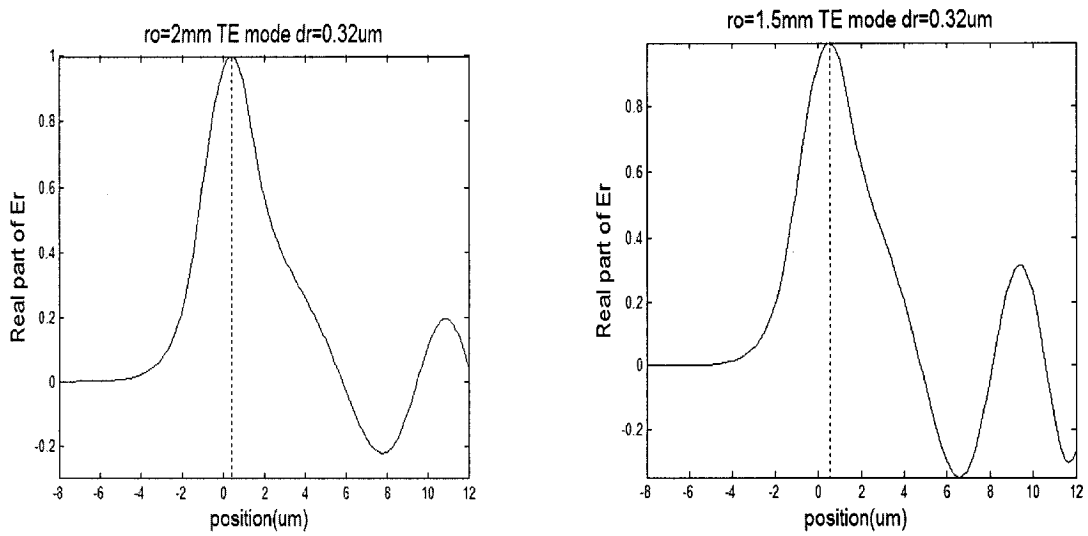

(c) (d)

Fig. 3-7 1D normalized dominant electric field distributions of the TE mode of the rib waveguide bend with dr=0.32 μ m, where the distributions are normalized by the peak value of the real part of Er. (a) to (d) correspond to four cases of radius, i.e. 6mm,3mm,2mm, and 1.5mm.

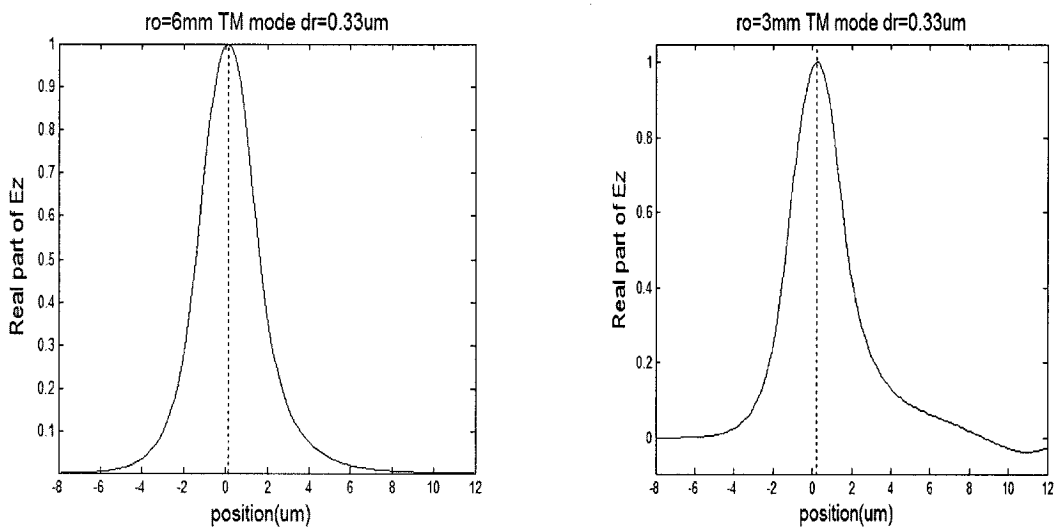

(a) (b)

Fig. 3-8 continues from page 59- page60.

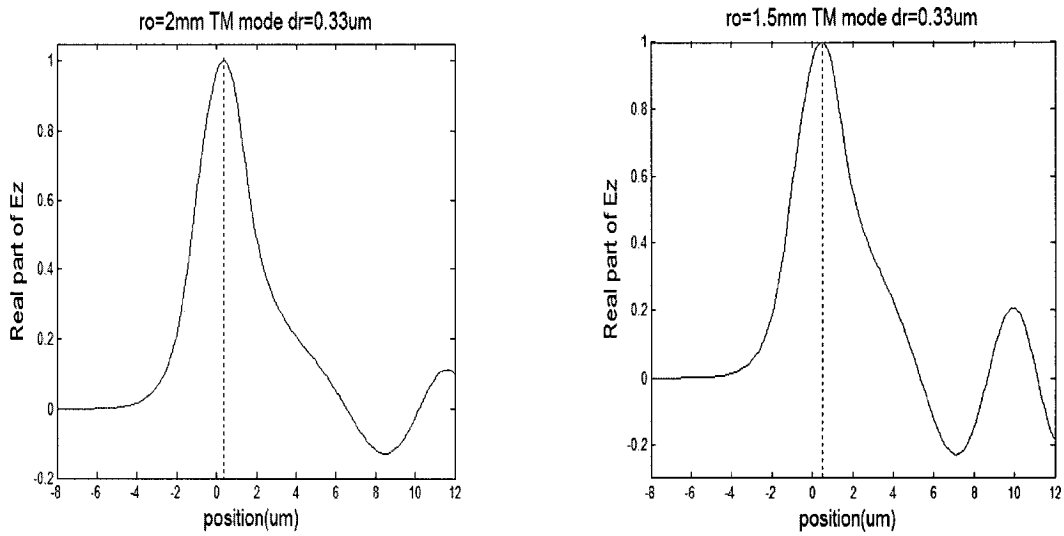

(c) (d)

Fig. 3-8 1D normalized dominant electric field distributions of the TM mode of the rib waveguide bend with dr=0.33 μ m, where the distributions are normalized by the peak value of the real part of Ez. (a) to (d) correspond to four cases of radius, i.e. 6mm,3mm,2mm, and 1.5mm.

(B) 2D field distributions

Figure 3-9 presents six 2D normalized spatial field distributions of the TE mode over the cross-section of the bent rib waveguide structure with ro=1m, and dr=0.32 μ m, while Fig. 3-10 shows six 2D normalized spatial field distributions of the TM mode on the cross-section of the bent rib waveguide structure with ro=1m, and dr=0.33 μ m. All fields are normalized to the peak value of the real part of their dominant electric fields. Fig. 3-9 and Fig. 3-10 show that Er or Ez is the dominant electric field for TE mode or TM mode, respectively. For the bent waveguide with ro=1m, the radius is large enough for the waveguide to be treated as a straight one. Therefore, all fields shown in Fig. 3-9 and Fig. 3-10 present symmetry about the vertical plane (r=0).

Figure 3-11 gives several contour plots of absolute normalized dominant electric field distributions of the TE mode (Er), while Fig. 3-12 presents several contour plots of absolute normalized dominant electric field distributions of the TM mode (Ez) on the same cross-section of the rib bend structure with dr=0.32μm. All fields are normalized to their corresponding maximum magnitudes. Fig.3-11(a) to Fig.3-11 (d) or Fig.3-12(a) to Fig.3-12 (d) correspond to four cases of radius, i.e. 1m, 4mm, 3mm, and 2mm. It is easily observed that the bending shifts the modal fields outward: the smaller the radius, the greater the shifting, and that the bending renders the fields more asymmetric about the vertical axis (r=0) for a smaller bend radius. By comparing Fig. 3-11 with Fig.3-12, it can be found that the dominant electric fields of the TE mode present more shifting than those of the TM mode at the same radius for this bent waveguide structure. Therefore, the TE mode of this bent waveguide structure shows more radiation loss than the TM mode at the same radius, as is observed by comparing Fig. 3-2 (b) to Fig. 3-2 (e).

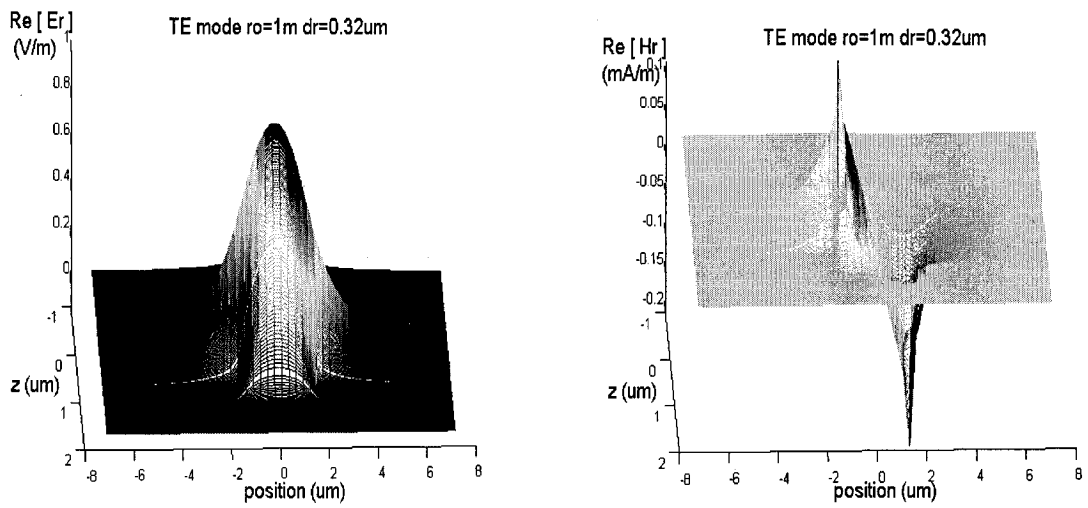

(a) (b)

Fig. 3-9 continues from page 61- page62.

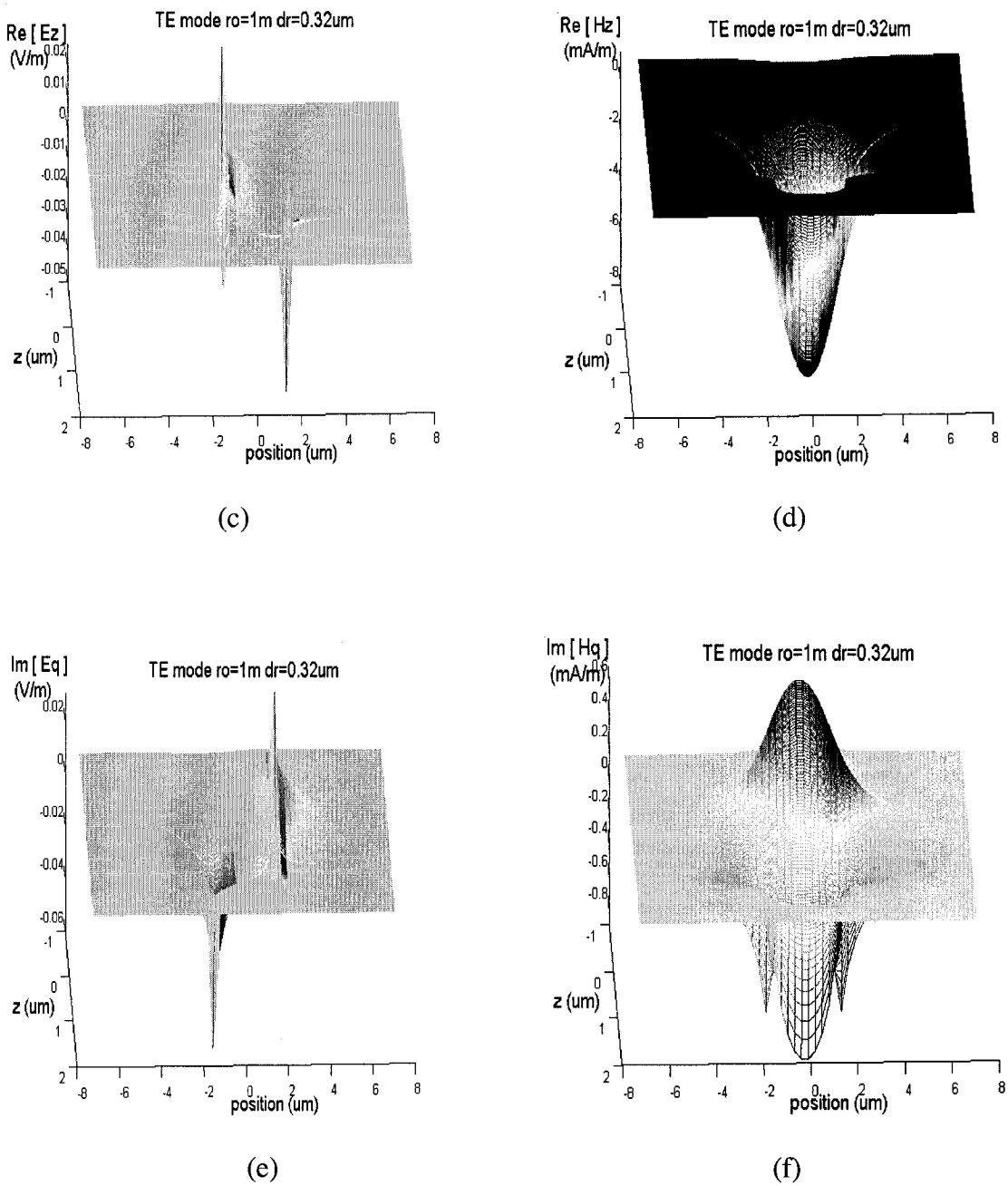

Fig. 3-9 Six 2D normalized spatial field distributions of the TE mode on the cross-section of the straight rib structure (ro=1m, dr=0.32 μ m). All quantities are normalized to the peak value of the real part of Er.

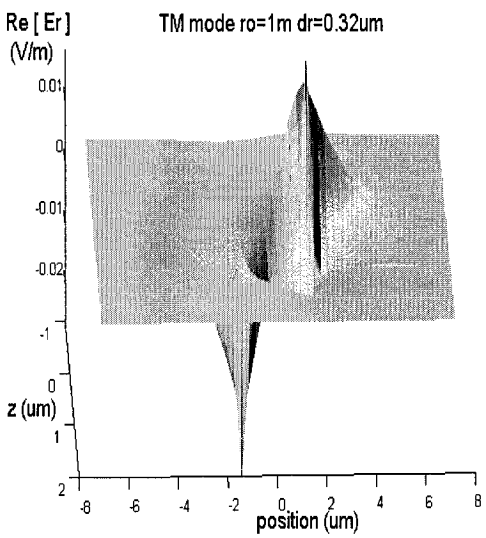

(a)

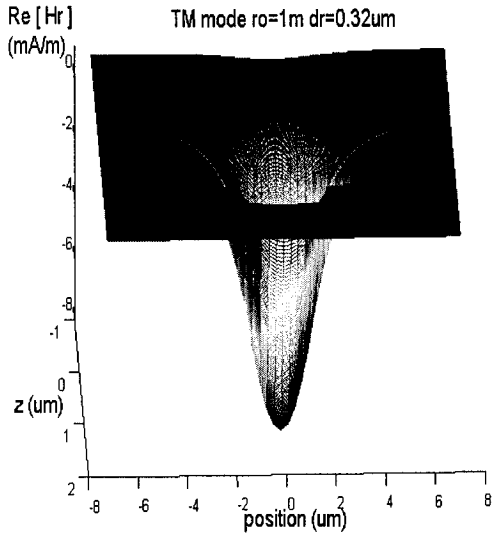

(b)

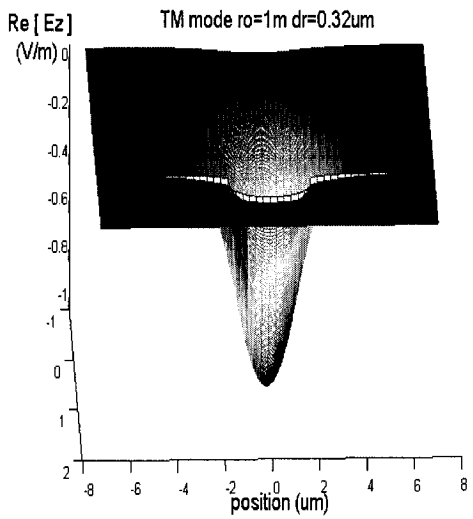

(c)

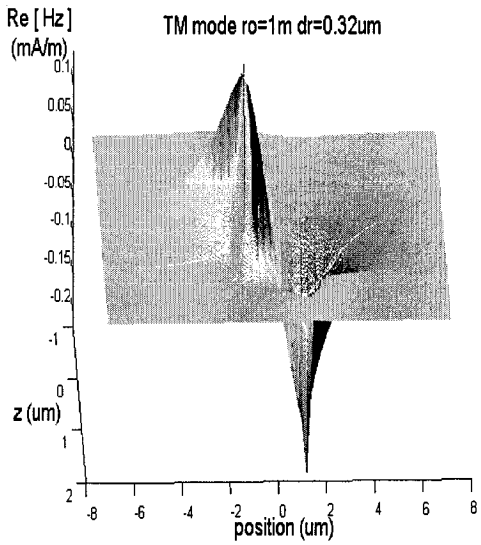

(d)

Fig. 3-10 continues from page 63- page 64.

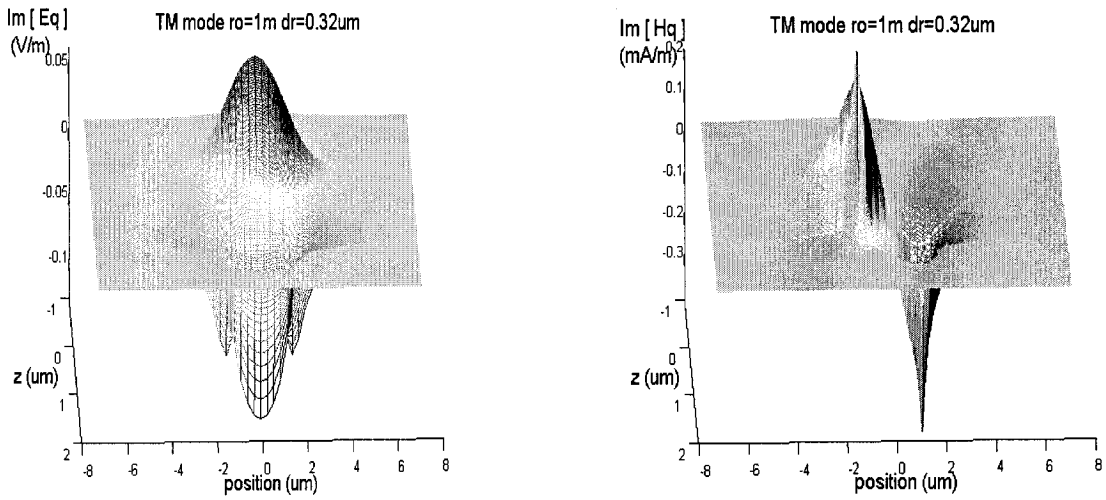

(e) (f)

Fig. 3-10 Six 2D normalized spatial field distributions of the TM mode on the cross-section of the straight rib structure (ro=1m, dr=0.32um). All quantities are normalized to the peak value of the real part of Ez.

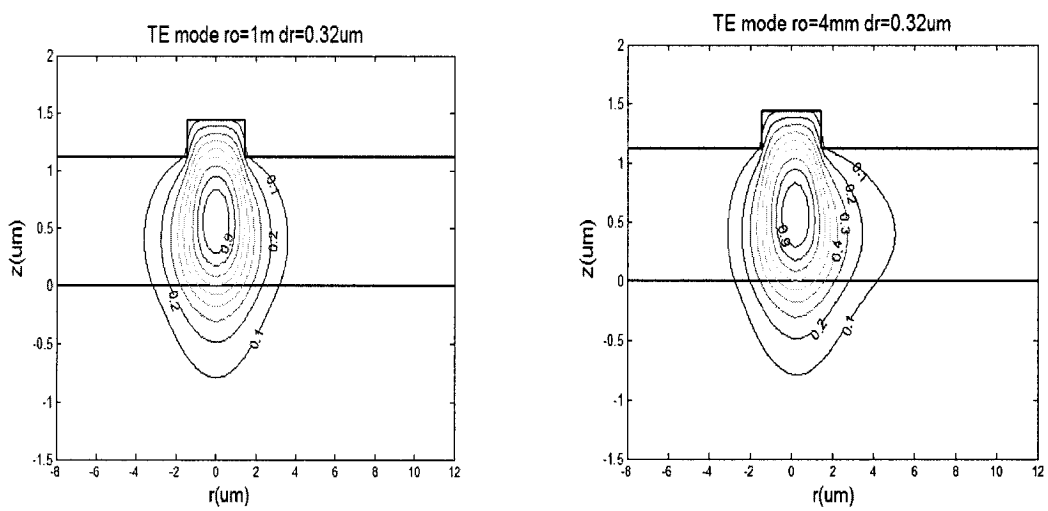

(a) (b)

Fig. 3-11 continues from page 64- page 65.

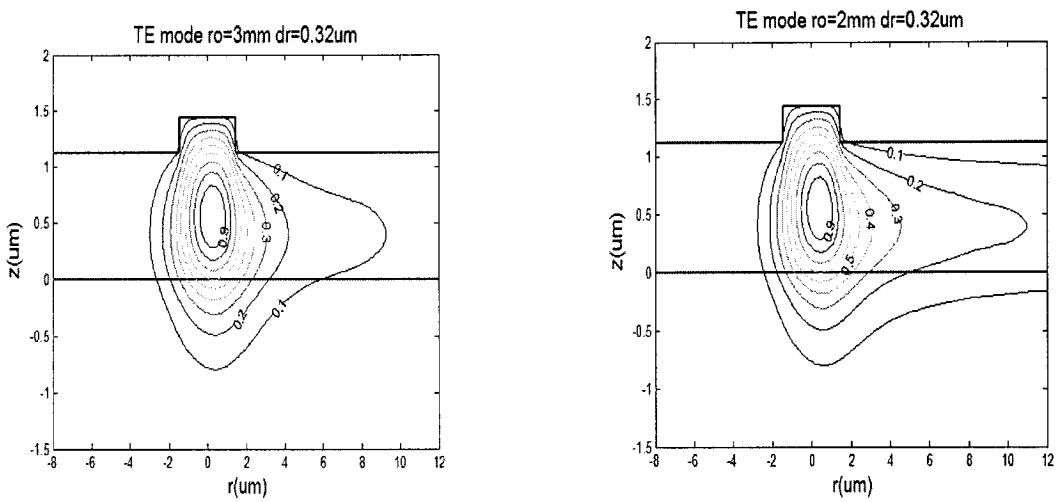

(c) (d)

Fig. 3-11 Contour plots of absolute normalized dominant electric field distributions of the TE mode (Er) on the cross-section of the rib bend structure with dr=0.32μm, where Er is normalized by the maximum magnitude of Er. (a) to (d) correspond to four cases of radius, i.e. 1m, 4mm, 3mm, and 2mm.

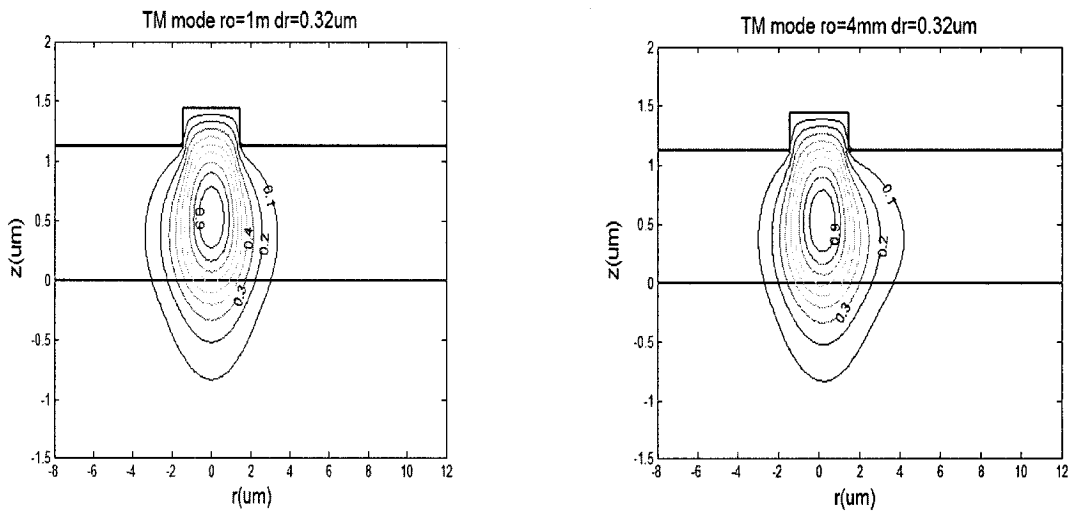

(a) (b)

Fig. 3-12 continues from page 65- page 66.

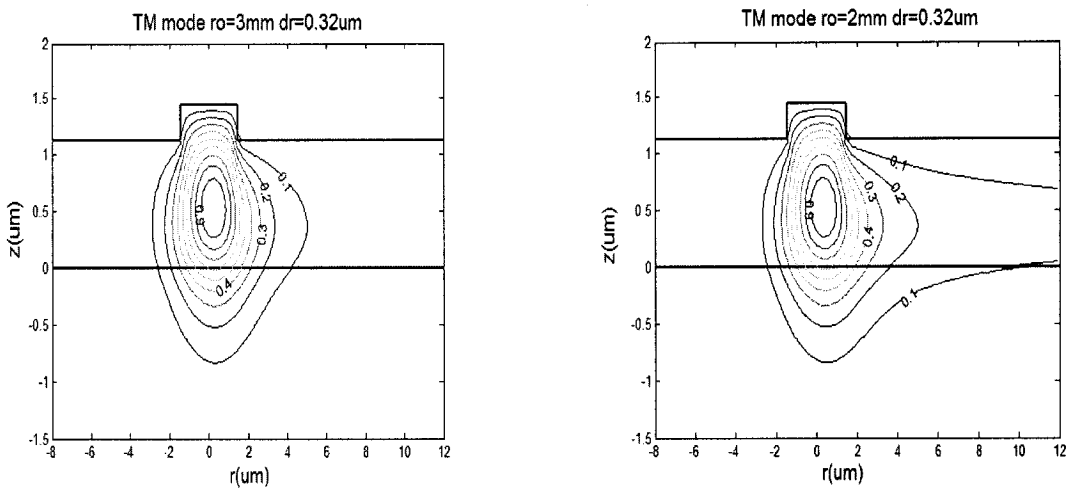

(c) (d)

Fig. 3-12 Contour plots of absolute normalized dominant electric field distributions of the TM mode (Ez) on the cross-section of the rib bend structure with dr=0.32μm, where Ez is normalized by the maximum magnitude of Ez. (a) to (d) correspond to four cases of radius, i.e. 1m, 4mm, 3mm, and 2mm.

3.3 Validation II

T. Yamamoto and M. Koshiba have computed the radiation losses for the structure shown in Fig. 3-13 using the Finite-Element Method (FEM) [19], and compared their results with those from experiments [45] and those obtained by J.S. Gu using the semi-vectorial MoL [21]. S. Kim and A. Gopinath have analyzed the same structure using the Finite-Difference Method (FDM) and got similar results [23]; furthermore, they also analyzed the transition loss at the junction between the straight waveguide and the curved one. In this part of the validation, the code will be applied to the same structure and the numerical results will be compared with those from [19][21][23][45].

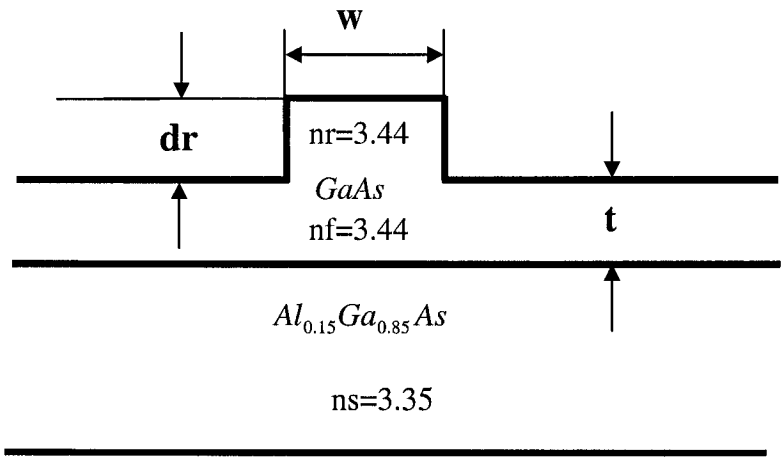

Fig. 3-13 Rib waveguide structure with rib width w and height dr. The waveguide film thickness is represented with t and the thickness of the substrate is treated as being infinite.

3.3.1 Numerical results and comparisons

(A) Structure parameters (see Fig. 3-13)

At the wavelength $\lambda = 1.15 \mu m$, the refractive indices of the layers in the rib waveguide are na (cover) =1, nr (rib) = 3.44, nf (film)=3.44, and ns (substrate)=3.35; geometrical parameters of the rib waveguide are w (rib width)= $3 \mu m$, dr (rib height) = $0.4 \mu m$, and t (film thickness) = $0.4 \mu m$ or $0.3 \mu m$.

(B) Computation window and the lines on the rib

After several attempts to adjust the distance between the right absorbing boundary and the outside of the rib, it is observed that one rib width (w) is enough to obtain converged numerical results. As to the lines on the rib, at least 30 E lines should be placed on the rib to obtain converged results.

(C) Numerical results

Figure 3-14 shows the numerical results of the radiation losses versus radius for the bend structure shown in Fig.3-13. In Fig.3-14, the solid line represents the numerical results; the dot and asterisk represent results from the experiment [45] and other numerical methods (FDM or FEM), respectively. Fig. 3-14 (a) and Fig. 3-14 (c) give the results of the TE mode of the structure with film thickness t=0.4; Fig. 3-14 (b) presents the results of the TM mode for the same structure. Fig. 3-14 (d) gives the radiation losses versus radius for the TE mode of the bend structure with the film thickness t=0.3um. From Fig. 3-14, it is seen that the agreement of the numerical results for the small radii of curvature with those from the experimental data [45] are acceptable, but the experiments [45] show much larger losses than the calculations for the larger radii of curvature, being greater than 200μm. Scattering losses of the waveguides apparently dominate for the bend structure with large radii of curvature and scattering losses are not taken into account in the formulation applied here. Comparing Fig. 3-14 (a) with Fig. 3-14 (b) shows that the TE mode of this bent waveguide structure with dr=t=0.4μm has more radiation loss at the same radius. It is also found from comparing Fig.3-14 (c) with Fig.3-14 (d) that the bend structure with a thinner film and same rib height produces lower radiation loss at the same radius.

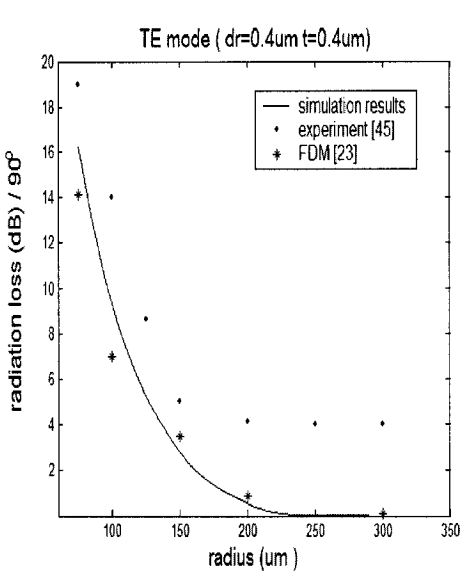

(a)

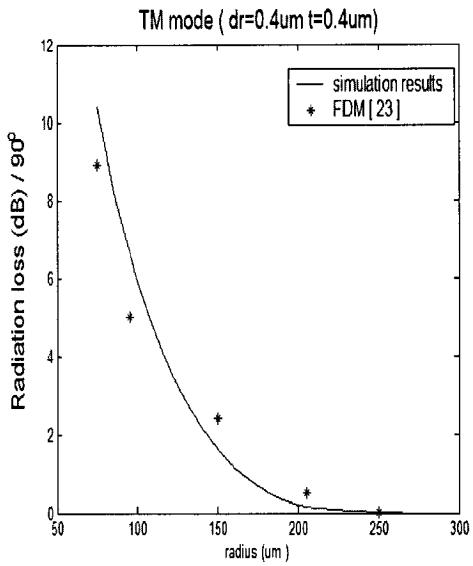

(b)

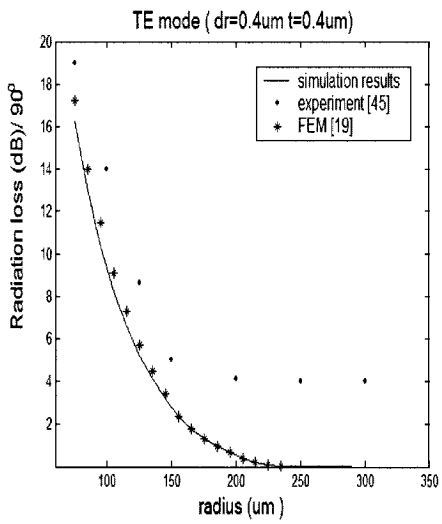

(c)

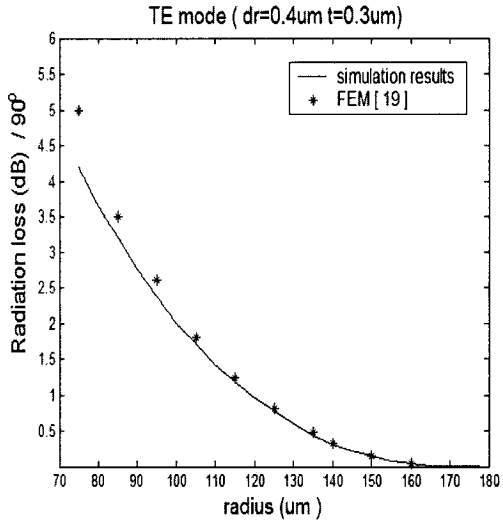

(d)

Fig. 3-14 Radiation losses versus radius, (a) to (c) are for the bend structure with film thickness t=0.4um and (d) for t=0.3um. Solid lines represent the numerical results, dot for experimental data, and the asterisk for data from other numerical methods.

Figure 3-15 shows the numerical results of the transition losses versus radius for the bend structure shown in Fig. 3-13. S. Kim and A. Gopinath have computed the transition losses of the TE and TM mode of the structure in [23]. They assume the end of the 90° bend is connected with the straight waveguide. Fig. 3-15 (a) gives the results for the TE mode, while Fig. 3-15 (b) shows the results for the TM mode. Through comparison, it is observed that the numerical results are close to those obtained by S. Kim and A. Gopinath. Fig. 3-15 shows that the transition loss tends to decrease with the radius becoming larger for both fundamental modes. From Fig. 3-15 (a) and Fig. 3-15 (b), it is found that the TE mode of this bend structure with dr=t=0.4μm produces more transition loss than the TM mode at the same radius, as the former case yields more radiation, resulting in more field shifting, and therefore gives more transition loss.

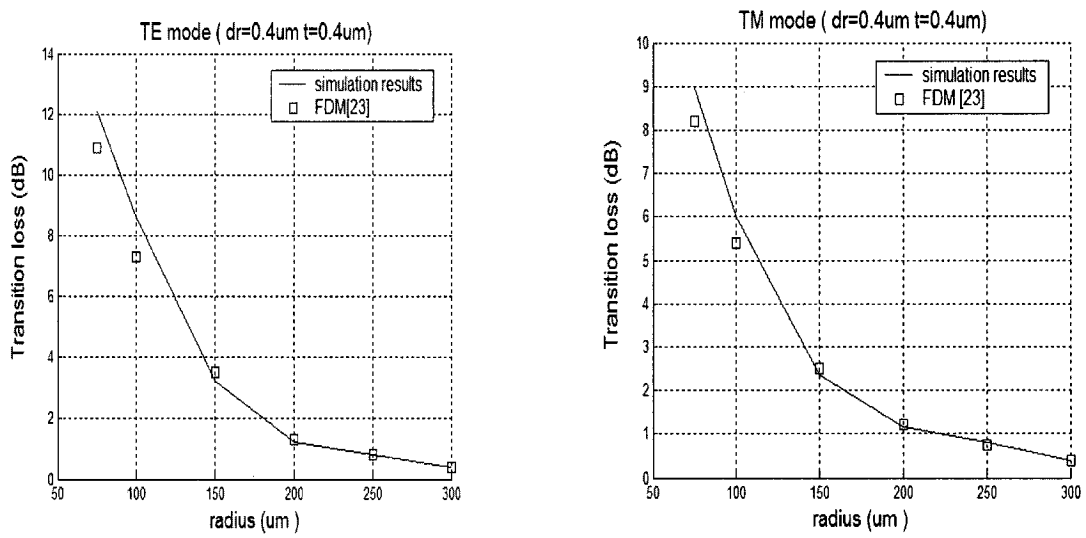

(a) (b)

Fig. 3-15 Transition losses versus radius, (a) for the TE mode and (b) for the TM mode. Solid lines represent the numerical results and the square for those from FDM.

3.3.2 Optimal Lateral Offset

It is known that the transition loss occurs at the junction of two waveguides with different radii of curvature(as shown in Fig.3-15). Introducing a lateral offset in the direction of the bend radius [51-54], as shown in Fig.3-16, is the usual method used to reduce this transition loss. The lateral offset improves the matching of the field distributions at the junction; thus, the transition loss is reduced. In fact, there exists an optimal lateral offset for the junction of two waveguides with fixed radii of curvature to minimize the transition loss. The optimal lateral offset is calculated from the shifted overlap integral. The following example will show that the code can be used to find the optimal lateral offset in practical designs.

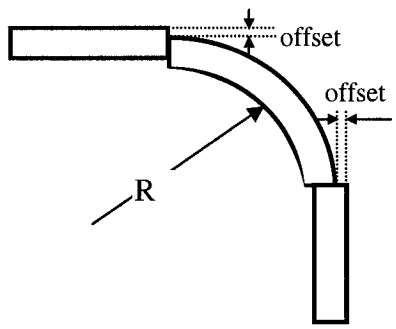

Fig. 3-16 Schematic diagram of lateral junction offsets between straight and curved waveguides.

In [23], S. Kim and A. Gopinath have calculated the optimum lateral offset. For the convenience of comparison, the code will be applied to the same structure, as shown in Fig. 3-13 shows, to find the optimum lateral offset. The structure has the following dimensional parameters: width=3 μm, film thickness t=0.4 μm and rib height dr =0.4 μm.

To find the optimal lateral offset, the overlap integral was repeated with different lateral locations for the straight waveguide. Fig. 3-17 presents the numerical results for

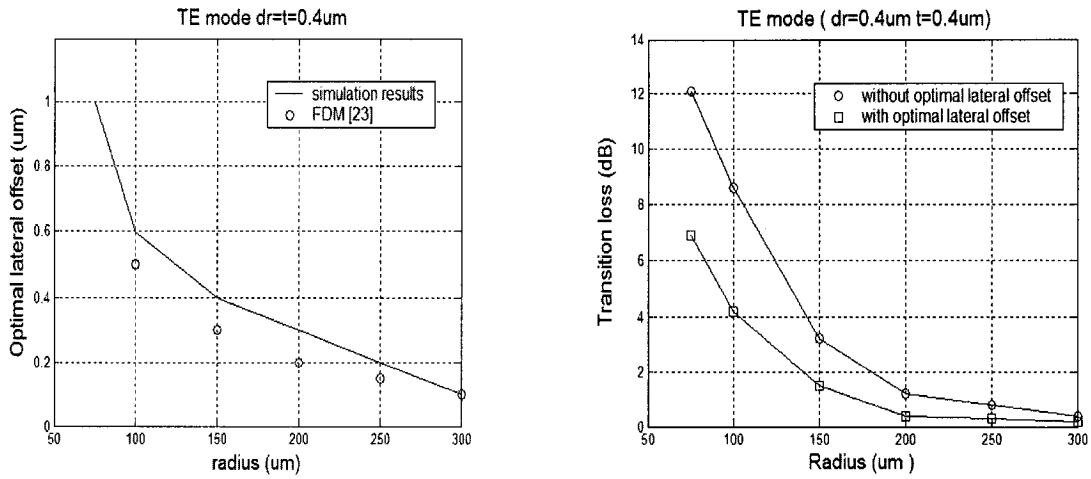

(a) (b)

Fig. 3-17 Optimal lateral offset and the minimized transition loss with the optimal offset for the TE mode. (a) is the plot of the optimal transition loss versus radius; (b) shows the transition loss versus radius without and with the optimal lateral offset.

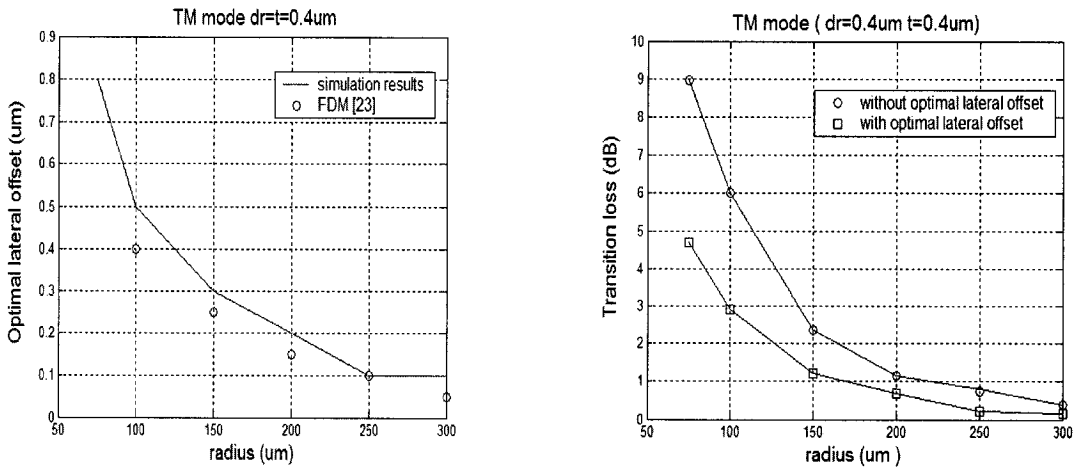

(a) (b)

Fig. 3-18 Optimal lateral offset and the minimized transition loss with the optimal offset for the TM mode. (a) is the plot of the optimal transition loss versus radius; (b) shows the transition loss versus radius without and with the optimal lateral offset.

the TE mode. Fig. 3-17 (a) gives the optimal lateral offset as a function of the radius of curvature, Fig. 3-17 (b) shows the transition loss as a function of the radius of curvature with and without the optimal lateral offset. Fig. 3-18 shows the numerical results for the TM mode. Fig. 3-18 (a) shows the optimal lateral offset versus the radius of curvature and Fig. 3-18 (b) gives the transition loss versus the radius of curvature with and without the optimal lateral offset. The numerical results for the optimal offset given in Fig. 3-17 and Fig. 3-18 are close to those from [23]. It is observed that the transition loss is reduced greatly with the optimal lateral offset. This example demonstrates that introducing a lateral offset is a very useful method to reduce the transition loss at the junction of two waveguides with different radii of curvature. Fig. 3-17 and Fig. 3-18 show that the bent waveguide structure with a smaller radius tends to have a greater optimal offset for both fundamental modes. It is very easy to understand as there is a greater modal mismatch at a smaller radius and thus a greater need for optimal offsets. Comparing Fig. 3-17 with Fig. 3-18 shows that the TE mode of this bend structure has a greater optimal offset than the TM mode at the same radius. This is attributed to the fact that the TE mode of this bend structure gives is shifted more than the TM mode at the same radius, and therefore needs a greater optimal offset.

3.4 Conclusion

In this chapter, the code has been applied to two different structures and the numerical results are compared with those available from other papers. It has been proven that the code works very well, and can be used to calculate the radiation loss due to the bending, as well as the transition loss coming from the mode mismatch between the bends with

different radii of curvature. In practice, the code can act as a general straight or bent waveguide mode solver. It thus can be employed to analyze not only lossless dielectric media, but also lossy media such as lossy metallization or lossy dielectric media, as the permittivity of each layer may be real or complex in the formulation. In Chapter 4, the developed code is successfully applied to analyze the mode propagation characteristics of metal waveguide bends, where the equivalent relative permittivity of the metal film at the wavelength of interest is negative.

Chapter 4

Metal Waveguide Bends

4.1 Introduction [46][47]

At optical wavelengths, the electromagnetic properties of some metals closely resemble those of an electron gas, or a cold plasma. Numerous experiments as well as classical electron theory both yield an equivalent negative dielectric constant for many metals such as gold, silver, and copper etc. when excited by an electromagnetic wave at or near optical wavelengths. It is well known that an interface between semi-infinite materials having positive and negative dielectric constants can guide transverse magnetic (TM) surface waves. According to solid state physics [55], a plasmon is a quantum of a plasma oscillation and the quantum of the coupled phonon-photon transverse wave field is called a polariton. In the case of a metal-dielectric interface, the waves are therefore termed plasmon-polariton modes and propagate as electromagnetic fields coupled to surface plasmons (surface plasma oscillations) comprised of conduction electrons in the metal.

A metal film of a certain thickness bounded by dielectrics above and below is often used as an optical slab (planar, infinitely wide) waveguide structure, with the core of the waveguide being the metal film. Metal films are commonly employed in optical

polarizing devices while long-range surface plasmon-polaritons can be used for signal transmission. Infinitely wide metal film structures, however, are of limited practical interest since they only offer 1D field confinement, which occurs along the vertical axis perpendicular to the direction of wave propagation implying that modes will spread out laterally as they propagate from a point, source used as the excitation. Metal films of finite thickness and finite width offer 2D field confinement in the plane transverse to the direction of propagation. These waveguides, termed plasmon-polariton waveguides for the sake of modes supported by them, may prove to be quite useful since they can be used in principle for optical signal transmission and routing over short distances or to construct passive components.

In [46][47], P. Berini has done much work on the characterization and description of plasmon-polariton modes guided by thin metal films of finite width. He has showed that the ss_b^0 mode, one of the fundamental modes supported by the metal waveguide, exhibits very interesting characteristics and is potentially very useful. The ss_b^0 mode evolves with decreasing film thickness and width towards the transverse electromagnetic (TEM) wave supported by the background, its losses and phase constant tending asymptotically towards those of the TEM wave. Carefully selecting the film's thickness and width can make this mode the only long-ranging one supported. In addition, the mode can have a field distribution that renders it excitable using an end-fire approach. The existence of this mode renders the finite-width metal film waveguide attractive for applications requiring short propagation distances and 2D field confinement in the transverse plane.

In the first part of this chapter, some numerical results in [47] are reproduced to further verify that the code can be applied to the analysis of metal waveguides. In the rest

of this chapter, the mode (ss_b^0) propagation characteristics of metal waveguide bends will be numerically analyzed.

4.2 Reproduction of some numerical results for straight metal waveguides

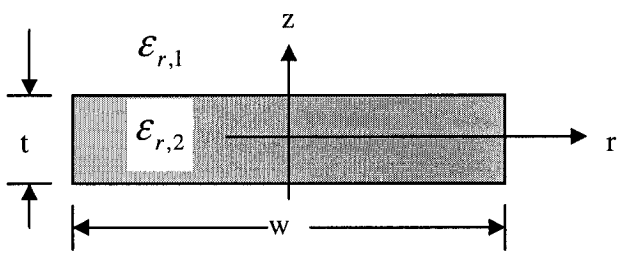

Fig. 4-1 Metal waveguide structure

The metal waveguide structure P. Berini considered in [47] is shown in Fig. 4-1. In [47], cartesian coordinate axes are used for the analysis, while cylindrical coordinate axes are employed in this code with propagation taking place along the ϕ axis, which is into the page. Here, t and w represent the thickness and width of the metal waveguide film; $\varepsilon_{r,2}$ is the equivalent permittivity of the metal film and the metal film is surrounded by an infinite homogeneous dielectric of permittivity $\varepsilon_{r,1}$. It is assumed in the analysis that the metal region shown in Fig. 4-1 can be modeled as an electron gas, i.e., a cold plasma, and that the dielectric function of a plasma can be approximately expressed as[55]: $\varepsilon(\omega) = 1 - \frac{\omega_p^2}{\omega^2}$, where ω_p is the plasma frequency and is dependent on the electron concentration. For the optical field to propagate through a plasma, its frequency ω should be greater than ω_p, i.e., a wave will propagate if its free space wavelength is less than $\lambda_p = 2\pi c / \omega_p$; otherwise the wave is reflected, and therefore λ_p is called the cut-off

wavelength. The table 4-1 below shows different electron concentrations and their corresponding cut-off wavelengths [55]. For plasmon-polariton waveguides, their operating wavelength should be greater than λ_p. In [47], the equivalent dielectric constants of this structure are $\varepsilon_{r,1} = 4$, $\varepsilon_{r,2} = -19 - j0.53$ (silver) and the optical free-space wavelength of excitation is set to $\lambda_0 = 0.633\mu m$. Note that the real part of the equivalent relative permittivity of silver at the wavelength of interest is negative.

Table 4-1

n, electrons/cm^3	10^{22}	10^{18}	10^{14}	10^{10}
λ_p, cm	3.3×10^{-5}	3.3×10^{-3}	0.33	33

As in [47], table 4-1 is used to show the vertical-horizontal wall combinations used along the axes of symmetry and the mode nomenclature proposed by P. Berini. The nomenclature for identifying the modes of the metal waveguide consists in using the letters a or s for asymmetric or symmetric transverse field distributions, respectively, followed by a subscript b or l for bound or leaky modes, respectively; m represents the order in the mode nomenclature. The ss_b^0, sa_b^0, as_b^0 and aa_b^0 modes are the fundamental modes supported by the metal waveguide

Table 4-2

Vertical-Horizontal walls	Mode
EW-EW	as_b^m
MW-EW	ss_b^m
MW-MW	sa_b^m
EW-MW	aa_b^m

4.2.1 Four fundamental modal distributions

In [47], the author showed the spatial 2D distribution of six electromagnetic fields for the four fundamental modes supported by the metal film with $w = 1\mu m$ and $t = 100nm$. The code is applied to the same structure and it reproduces the following results. It is observed that Fig. 4-2 to Fig. 4-5 show the same modal distributions as those represented in [47].

(A) Spatial distribution of six field components related to the ss_b^0 mode

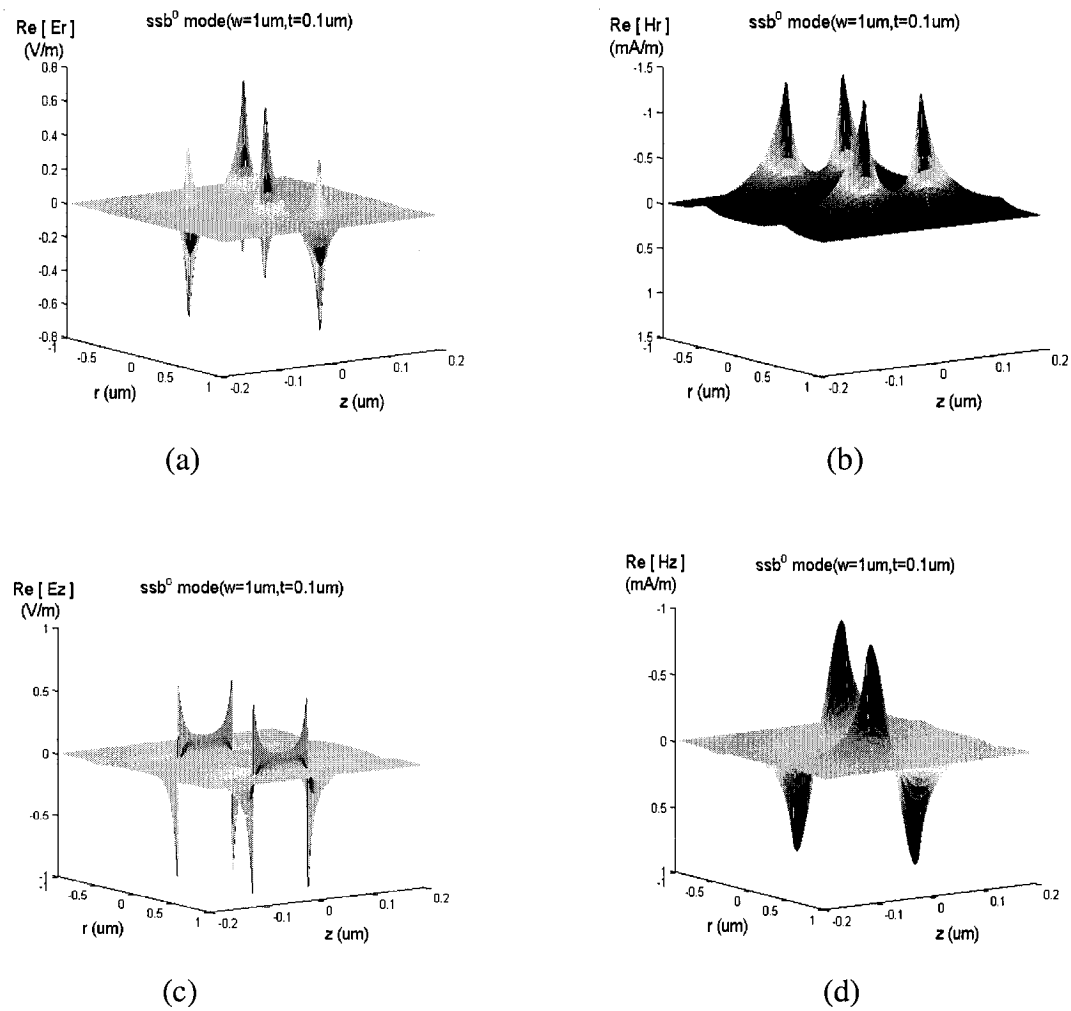

Fig. 4-2 continues from page 79- page 80.

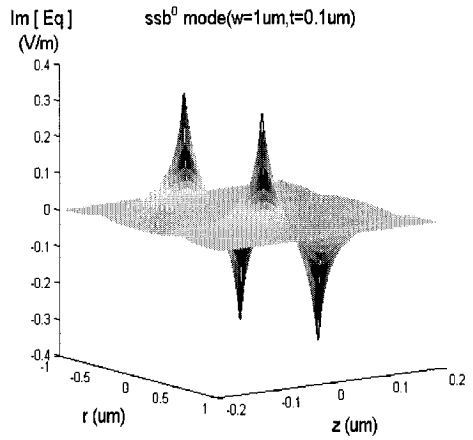

(e)

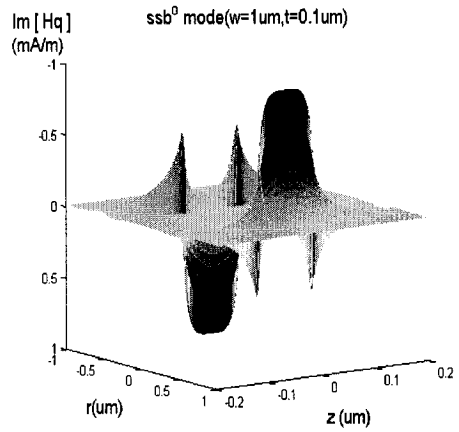

(f)

Fig. 4-2 Spatial distribution of the six field components related to the ss_b^0 mode supported by a metal film waveguide of thickness t=100nm and width w=1 μm. The waveguide cross-section is located in the r-z plane, and metal is bounded by the region $-0.5 \le r \le 0.5$ μm and $-0.05 \le z \le 0.05$ μm.The field distributions are normalized such that $\max\left|\mathrm{Re}\{E_z\}\right| = 1$.

(B) Spatial distribution of six field components related to the sa_b^0 mode

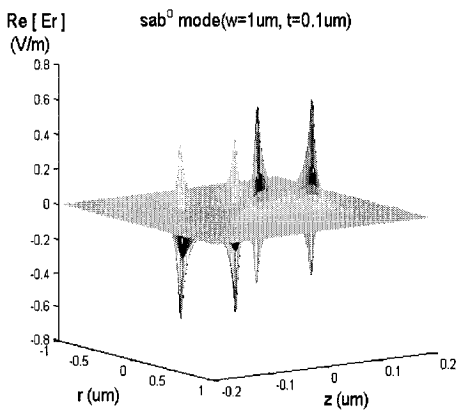

(a)

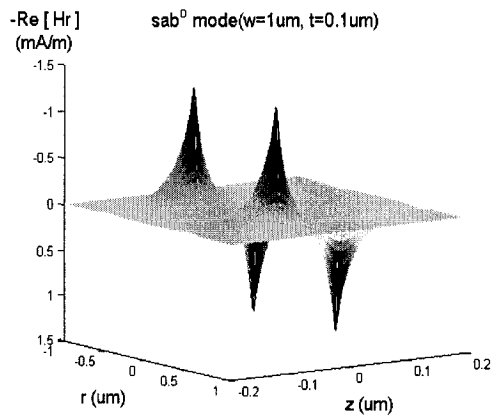

(b)

Fig. 4-3 continues from page 80- page 81.

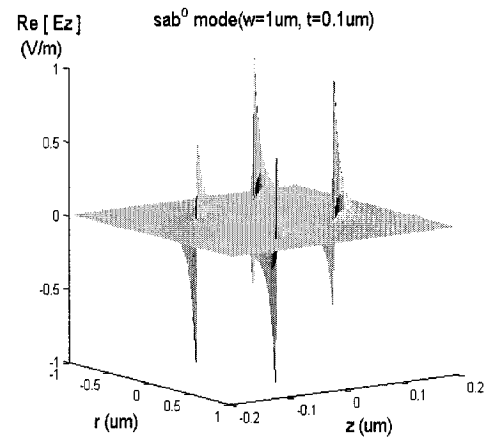

(c)

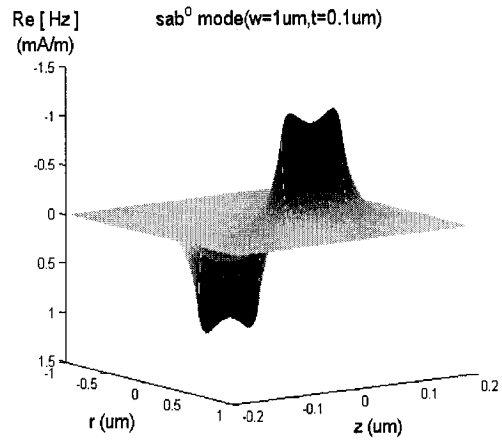

(d)

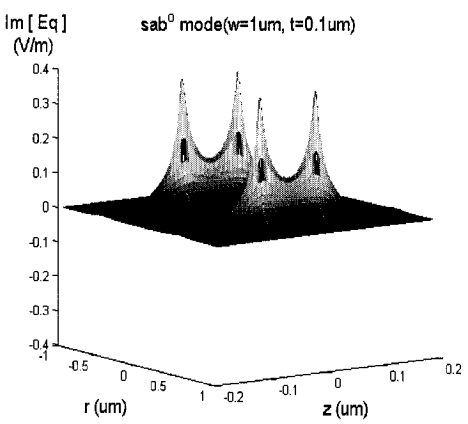

(e)

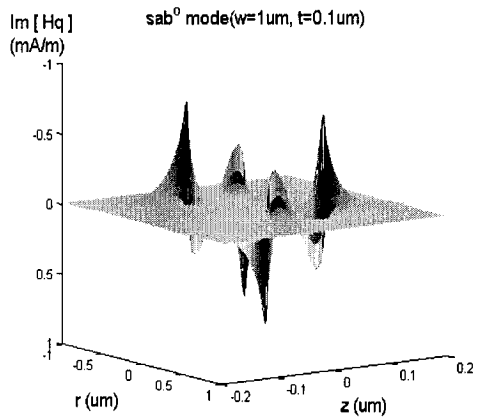

(f)

Fig. 4-3 Spatial distribution of the six field components related to the sa_b^0 mode supported by a metal film waveguide of thickness t=100nm and width w=1 μm. The waveguide cross-section is located in the r-z plane, and metal is bounded by the region $-0.5 \le r \le 0.5\ \mu m$ and $-0.05 \le z \le 0.05\ \mu m$.The field distributions are normalized such that $\max\left|\mathrm{Re}\{E_z\}\right| = 1$.

(C) Spatial distribution of six field components related to the as_b^0 mode

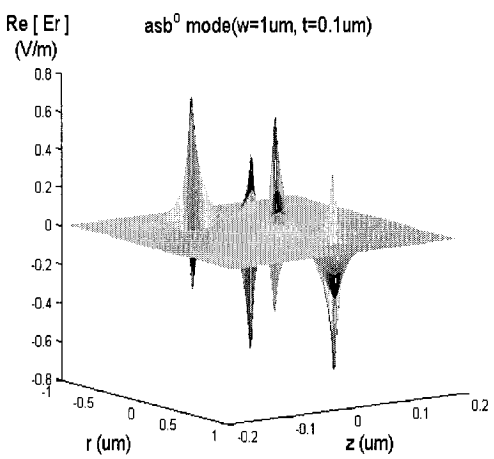

(a)

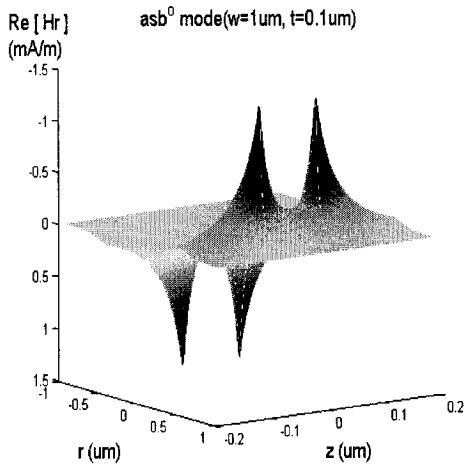

(b)

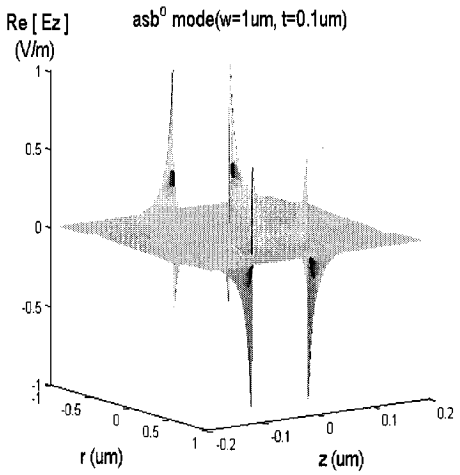

(c)

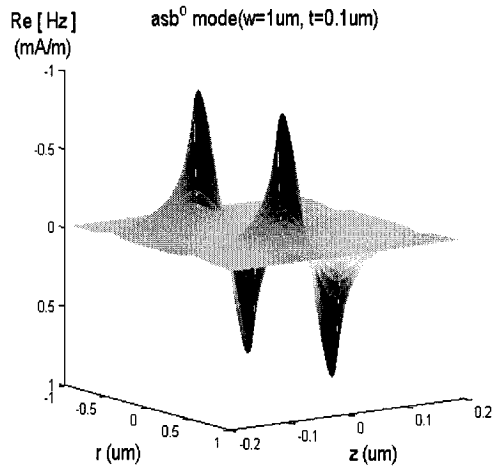

(d)

Fig. 4-4 continues from page 82- page 83.

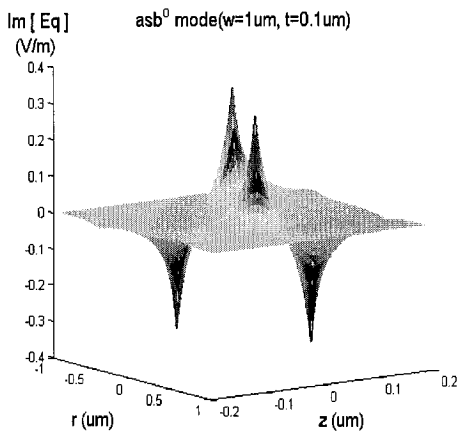

(e)

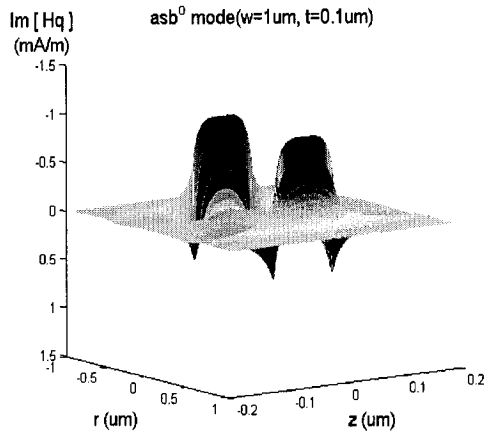

(f)

Fig. 4-4 Spatial distribution of the six field components related to the as_b^0 mode supported by a metal film waveguide of thickness t=100nm and width w=1 μm. The waveguide cross-section is located in the r-z plane, and metal is bounded by the region $-0.5 \le r \le 0.5\ \mu m$ and $-0.05 \le z \le 0.05\ \mu m$. The field distributions are normalized such that $\max\left|\mathrm{Re}\{E_z\}\right| = 1$.

(D) Spatial distribution of six field components related to the aa_b^0 mode

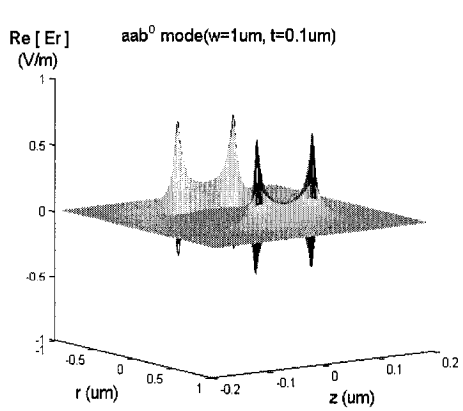

(a)

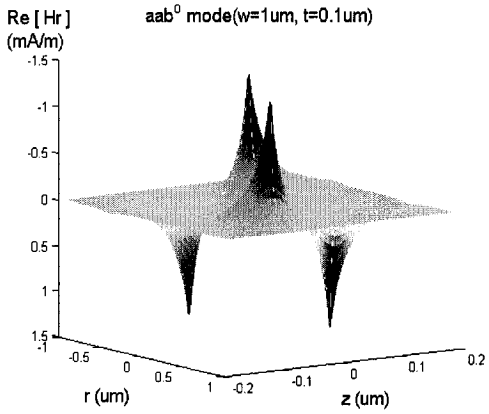

(b)

Fig. 4-5 continues from page 83- page 84.

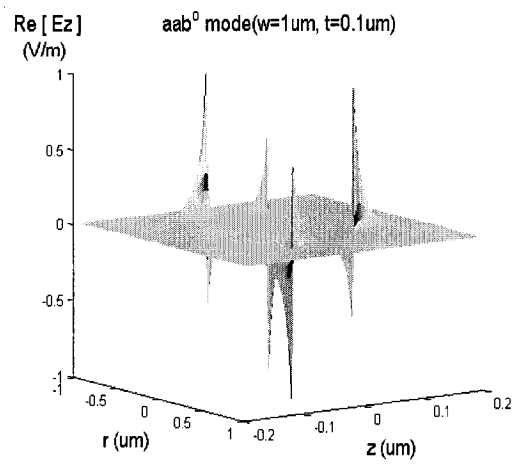

(c)

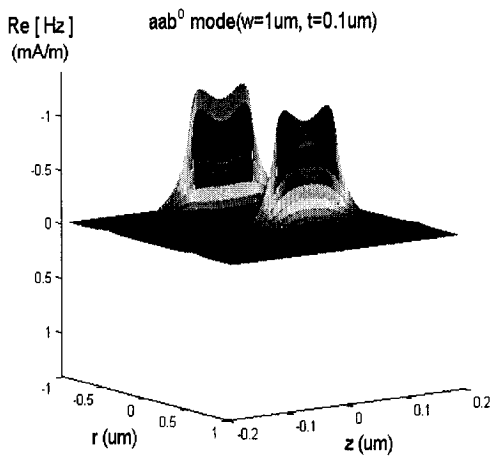

(d)

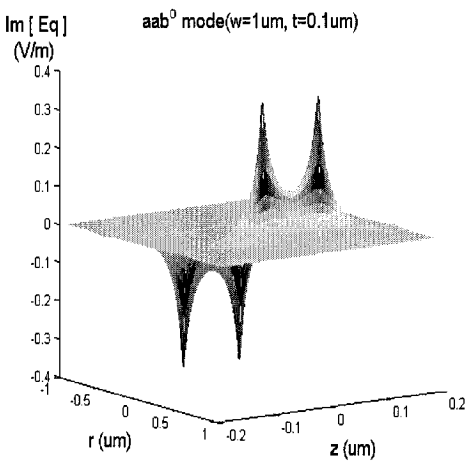

(e)

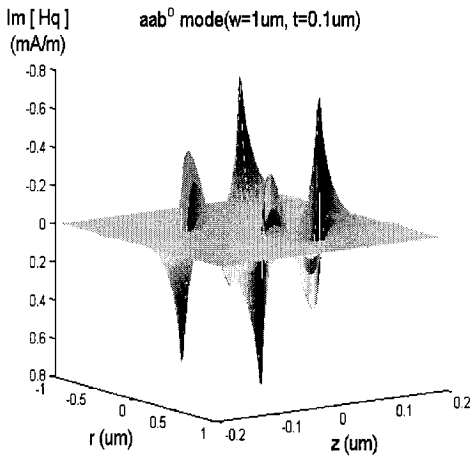

(f)

Fig. 4-5 Spatial distribution of the six field components related to the aa_b^0 mode supported by a metal film waveguide of thickness t=100nm and width w=1 μm. The waveguide cross-section is located in the r-z plane, and metal is bounded by the region $-0.5 \le r \le 0.5$ μm and $-0.05 \le z \le 0.05$ μm. The field distributions are normalized such that $\max\left|\mathrm{Re}\{E_z\}\right| = 1$.

4.2.2 Reproduction of modal dispersion curves with metal film thickness

In [47], P. Berini has showed the mode characteristics and evolution with film thickness of the metal waveguide. To verify the code, the modal dispersions associated with the four fundamental modes for the metal waveguide with film width w=1μm are reproduced. By comparison, almost the same curves as those from [47] are obtained.

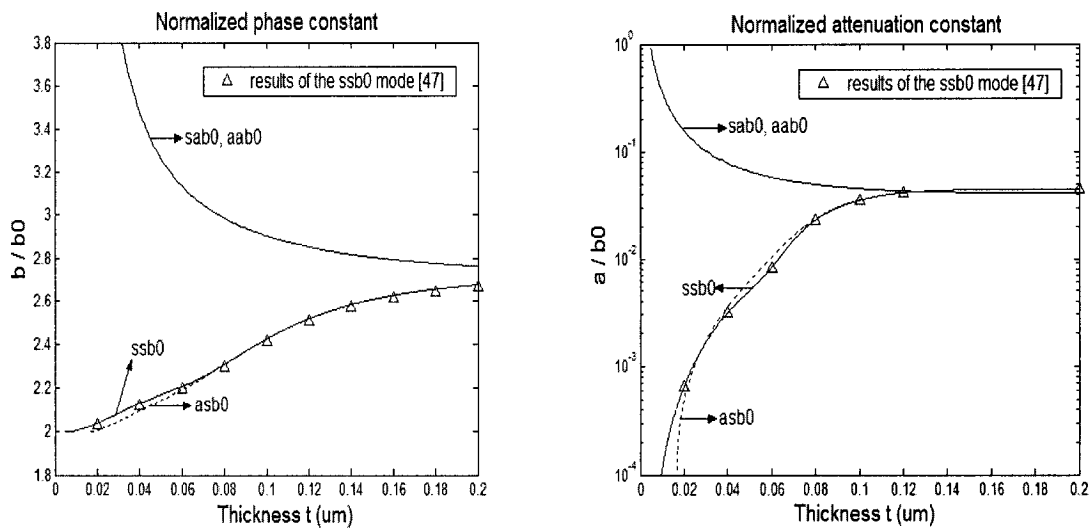

(a) (b)

Fig. 4-6 Dispersion characteristics with thickness of the four fundamental modes supported by a metal film waveguide of width w=1μm. (a) Normalized phase constant. (b) Normalized attenuation constant. The triangle symbol represents the numerical results of the ss_b^0 mode from [47].

4.2.3 Reproduction of $\mathrm{Re}\{S_\phi\}$ of the mode ss_b^0

In [47], the author also shows the profile of $\mathrm{Re}\{S_z\}$of the mode ss_b^0 over the cross-section of the metal waveguide for the case of thickness t=20nm and width w=1μm. Note that cartesian coordinate axes are used in [47], and $\mathrm{Re}\{S_z\} = \mathrm{Re}\,(E_x H_y^* - E_y H_x^*)/2$, while $\mathrm{Re}\{S_\phi\} = \mathrm{Re}\,(E_z H_r^* - E_r H_z^*)/2$ in the case of cylindrical coordinates. The code is applied to the same structure and the numerical results are shown in Fig. 4-7. It is observed that the normalized profile of $\mathrm{Re}\{S_\phi\}$ is the same as that of $\mathrm{Re}\{S_z\}$ represented in [47].

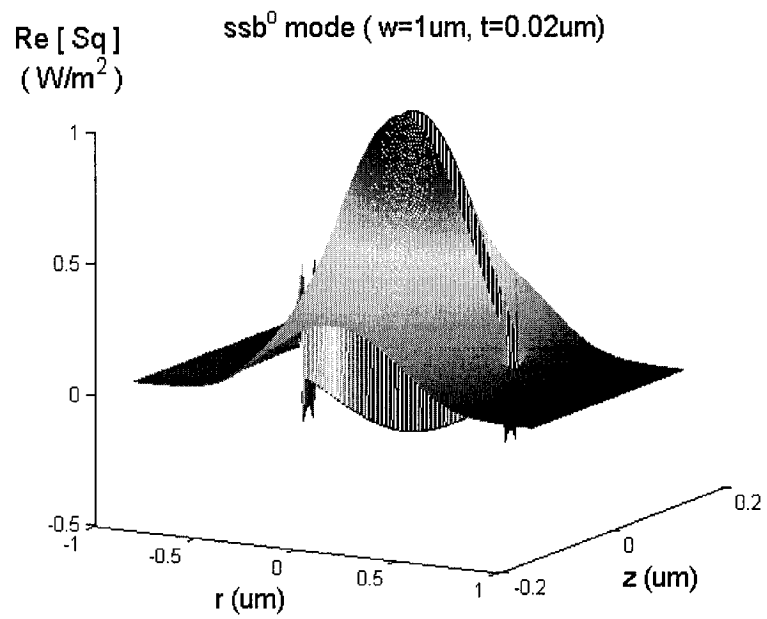

Fig. 4-7 Normalized profile of Re { S_ϕ } associated with the ss_b^0 mode for a metal film waveguide of width w=1um and thickness t=20nm. The waveguide cross-section is located in the r-z plane, and metal film is bounded by the region $-0.5 \le r \le 0.5\ \mu m$ and $-0.01 \le z \le 0.01\ \mu m$.

4.3 Mode propagation characteristics of metal waveguide bends

When the optical signal travels along a straight metal waveguide, there exists the propagation loss caused by the imaginary part of the equivalent dielectric constant. In this case, the insertion loss means the propagation loss. However, when it travels along a metal waveguide bend, the insertion loss includes two contributions: one is the inherent propagation loss coming from the imaginary part of the equivalent dielectric constant, and the other is the pure radiation loss due to the bending. In addition to the insertion loss, the transition loss will result if a bent metal waveguide is connected to another straight metal waveguide or metal waveguide bend with different radius. The accurate knowledge of the insertion loss, pure radiation loss and transition loss is very important for the metal waveguide to be applied in integrated optics. Besides, if metal waveguide bends are used for wavelength-selective waveguide devices such as the Mach-Zehnder interferometric(MZI) filter [4] and the arrayed-waveguide grating (AWG)[5] which require precise phase control in order to achieve wavelength accuracy, the accurate knowledge of the effect of bending-induced phase-constant change is also most important. Nevertheless, no literature, up to now, has dealt with these issues for metal waveguide bends. The code developed can be used to handle these issues. The following section give numerical results obtained from this code. No experimental or numerical results from other methods can be used for comparison, but the validity of these results is firmly believed because of the validation done for this code in Chapter 3 and some work done in the first part of this chapter.

The code is applied to the same structure as that described in [47], namely the optical free-space wavelength of excitation $\lambda_0 = 0.633\ \mu m$, the equivalent permittivity of the

metal film $\varepsilon_{r,2} = -19 - j0.53$ and the permittivity surrounding the metal film $\varepsilon_{r,1} = 4$. The cross-section of metal waveguide bends is as Fig. 4-1 shows. 12 cases of geometrical combinations of the bend structure are under consideration: the width is either w=1μm, or 0.5μm, and the thickness is t=10nm, 11nm, 12nm, 13nm, 14nm, or 15nm. The following numerical analysis only deals with the ss_b^0 mode supported by metal waveguide bends, as this mode is potentially useful in integrated optics [47].

To increase the computation efficiency, the symmetry of the modal distribution about the horizontal axis over the entire cross-section is utilized. An EW is therefore placed on the horizontal axis. Note that the vertical symmetry can not be employed as the bending has rendered the modal distribution to lose symmetry about the vertical axis (see Fig.4-12 to Fig. 4-15).

4.3.1 Numerical results

(A) Insertion loss, pure radiation loss and transition loss

Figure 4-8 and Fig. 4-9 show the numerical results of the insertion loss and the pure radiation loss versus the radii of curvature for the metal waveguide bend with different film thickness and width. Fig.4-8 (a_i) to Fig. 4-8 (f_i) ($i = 1, 2$) are for the waveguide structure with w=1μm and t=10nm to t=15nm, while Fig.4-9 (a_i) to Fig. 4-9 (f_i) ($i = 1, 2$) are for the waveguide structure with w=0.5μm and t=10nm to t=15nm, respectively. The subscript i identifies different kinds of losses, where $i = 1$ represents insertion losses, and $i = 2$ denotes pure radiation losses. The insertion loss is calculated by using this code and it comes from two contributions: the inherent propagation loss,

and the bending-induced pure radiation loss. In equation (2.117), α represents the insertion loss for metal waveguide bends. The propagation loss can be calculated by $\alpha_{prop} = 8.68 * \theta * \bar{r}_o * \mathrm{Im}(n_{eff})\,\mathrm{dB}$, where n_{eff} is the effective refractive index of the straight metal waveguide. The pure radiation loss is then obtained by subtracting the propagation loss from the insertion loss. The pure radiation losses can also be obtained by leaving out the imaginary part of the equivalent permittivity of the metal film in the simulation. It has been proven that the results from the two methods are very similar to each other.

From Fig. 4-8 and Fig. 4-9, it is observed that there exists a minimum for the insertion loss. Ropt denotes the radius corresponding to the minimum insertion loss. From equation (2.117), the insertion loss of a 90° metal waveguide bend depends on two factors: one is the radius and the other is the imaginary part of the effective propagation constant. When the radius becomes smaller little by little, the imaginary part of the effective propagation constant will increase gradually due to the bending, and therefore the insertion loss decrease or not is determined by which rate of change dominates. Obviously, decreasing the radius dominates for the case of $r_o > R_{opt}$, while the increasing of the imaginary part of the effective propagation constant weighs more for the case of $r_o < R_{opt}$. From Fig. 4-8 and Fig. 4-9, it is also found that the bending-induced radiation loss is very low when $r_o > R_{opt}$, and the insertion loss presents a quasi-linear relationship with the radius due to the fact that the insertion loss is mainly coming from the inherent propagation loss. From the numerical results shown in Fig. 4-8 and Fig. 4-9, a conclusion can be drawn for the pure radiation loss: a metal waveguide bend with a smaller geometrical-size film produces more pure radiation loss at a specific radius.

The optimum radius corresponding to the minimum point of the insertion loss shown in Fig. 4-8 and Fig. 4-9 is most interesting to the practical design. Considering its importance, the transition loss of the bent metal waveguide at the optimum radius is calculated assuming that it is connected to a straight metal waveguide. Fig. 4-10 presents optimum radii of curvature and the corresponding transition losses for metal waveguide bends, where the solid line represents the case of w=1μm, and the dashed line shows the case of w=0.5μm. Fig. 4-10 (a) gives optimum radii of curvature for metal waveguide bends with different geometrical combinations, while Fig. 4-10 (b) gives transition losses for curved metal waveguides at optimum radii of curvature. From Fig. 4-10 (a), it can be seen that a smaller geometrical-size metal waveguide bend presents a larger optimum radius. It is easily observed from Fig. 4-10 (b) that a smaller geometrical-size curved metal waveguide at its optimum radius shows lower transition loss.

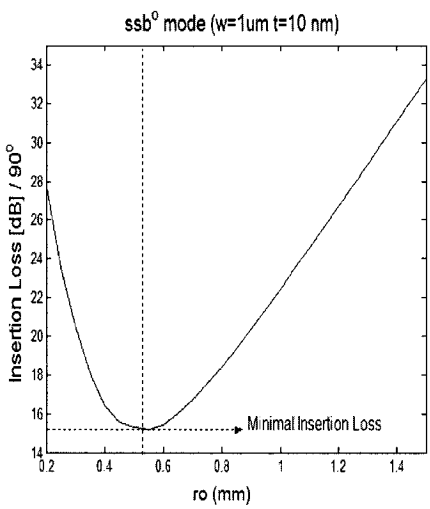

(a_1)

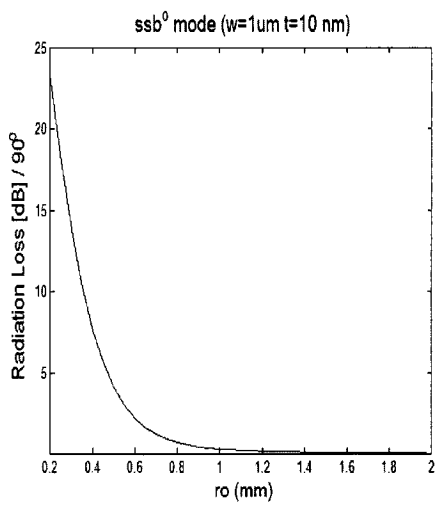

(a_2)

Fig. 4-8 continues from page 90- page 92.

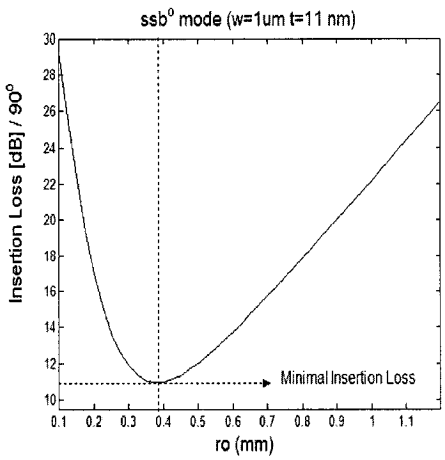

(b_1)

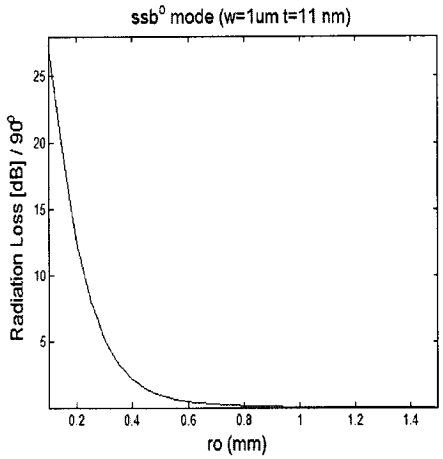

(b_2)

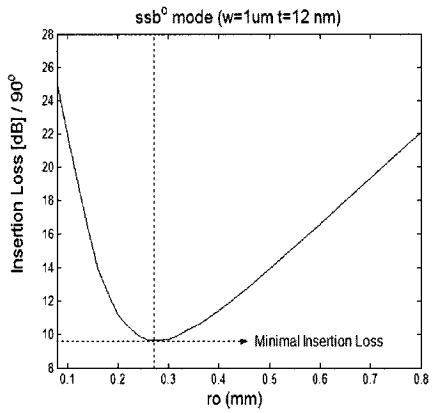

(c_1)

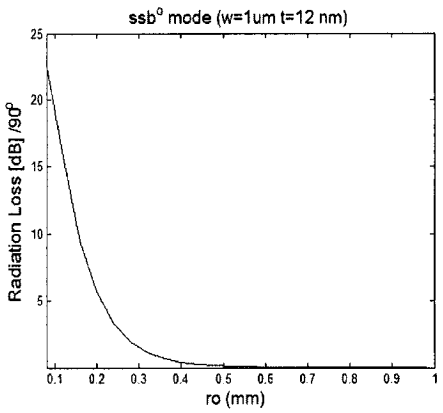

(c_2)

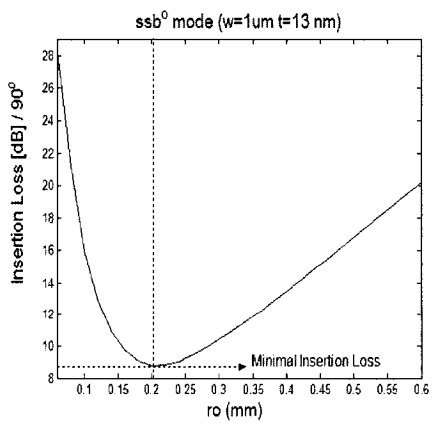

(d_1)

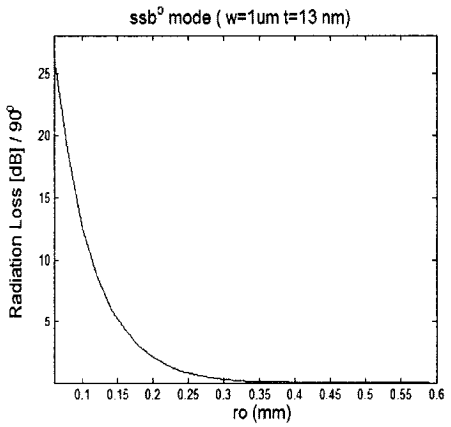

(d_2)

Fig. 4-8 continues from page 90- page 92.

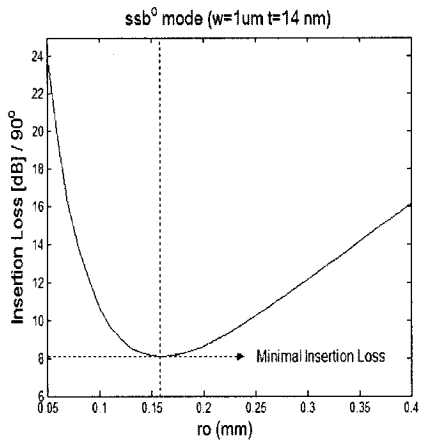

(e_1)

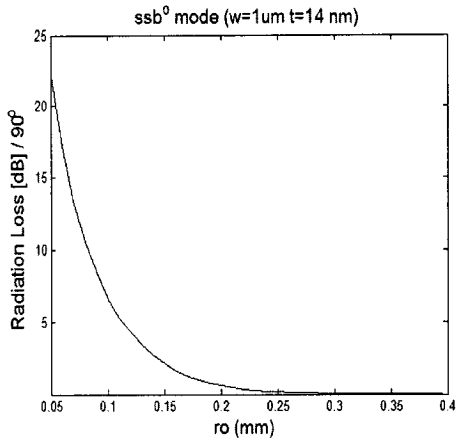

(e_2)

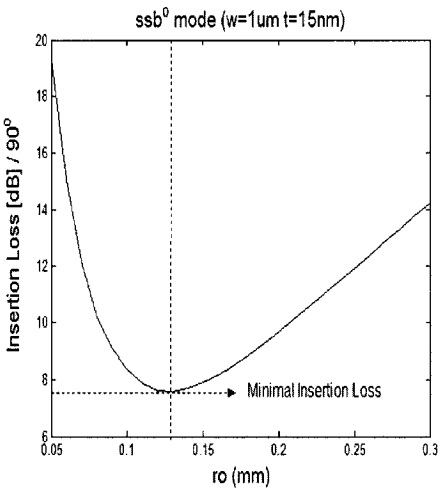

(f_1)

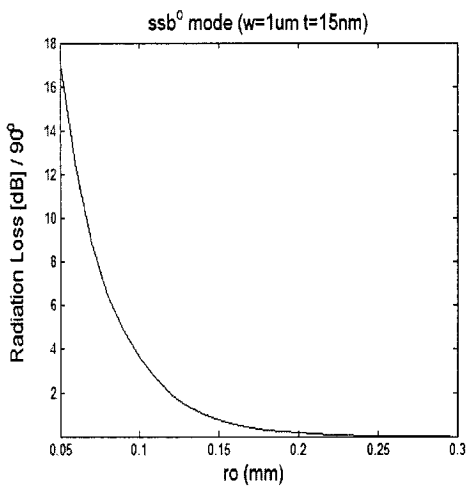

(f_2)

Fig.4-8 Insertion losses and pure radiation losses versus the radii of curvature for metal waveguide bends with w=1μm and t being from 10nm to 15nm (see Fig. 4-1). (a_i) to (f_i) $(i=1, 2)$ are for t=10nm to t=15nm, respectively. The subscript i identifies different kinds of losses, where $i=1$ represents insertion losses, and $i=2$ denotes pure radiation losses.

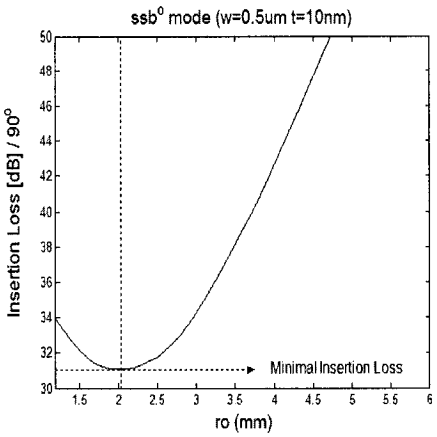

(a_1)

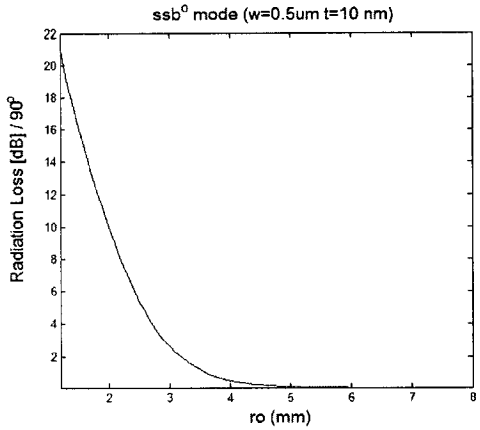

(a_2)

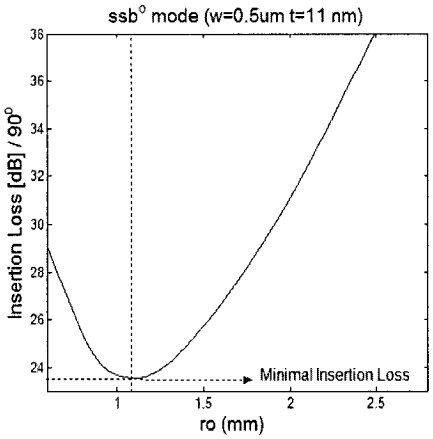

(b_1)

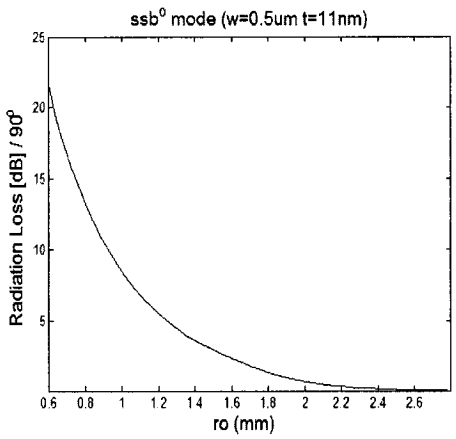

(b_2)

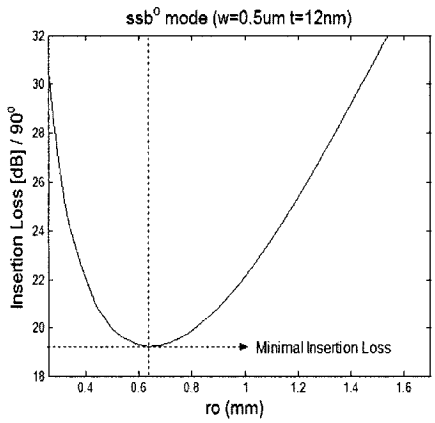

(c_1)

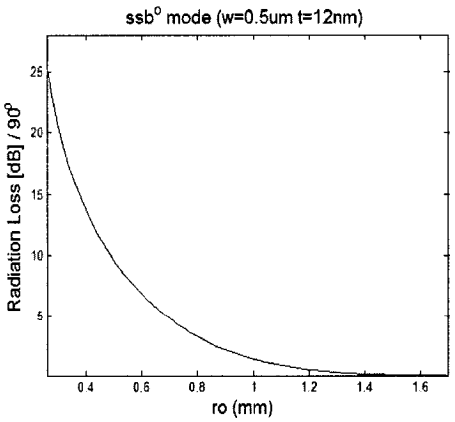

(c_2)

Fig. 4-9 continues from page 93- page 95.

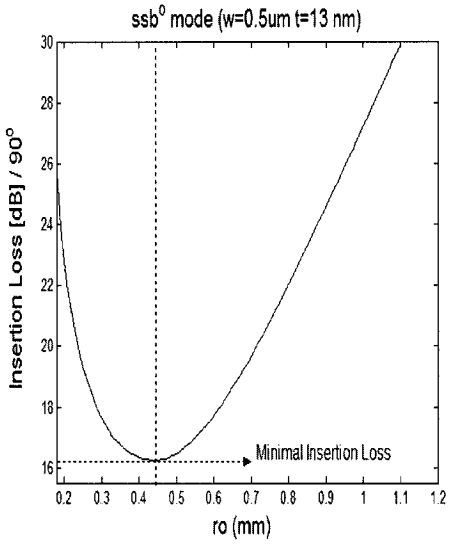

(d_1)

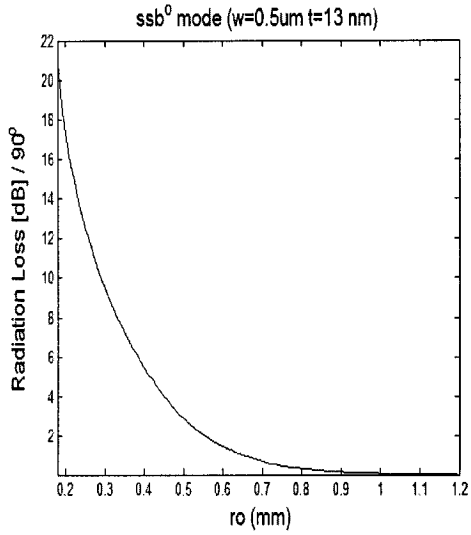

(d_2)

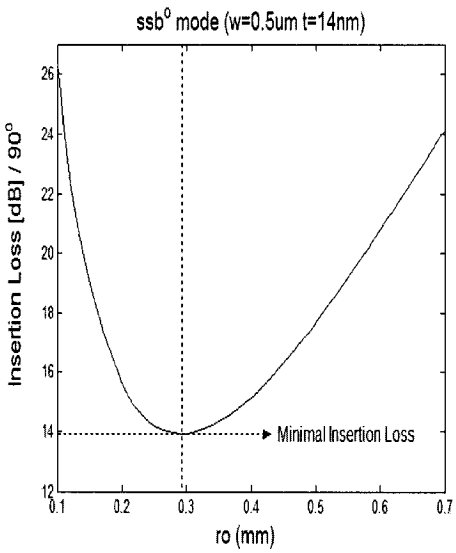

(e_1)

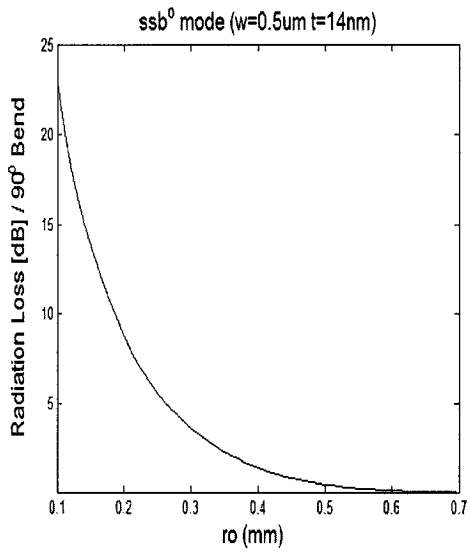

(e_2)

Fig. 4-9 continues from page 93- page 95.

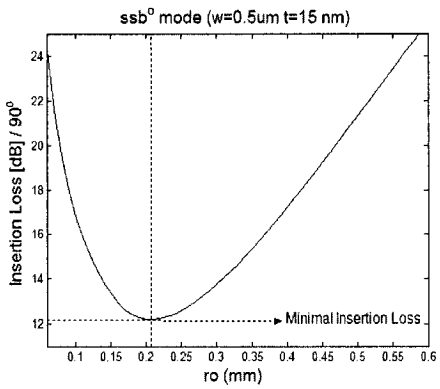

(f_1)

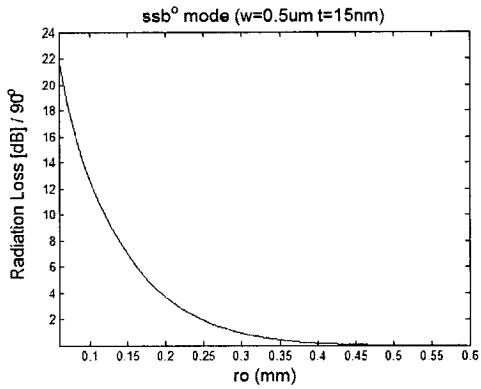

(f_2)

Fig.4-9 Insertion losses and pure radiation losses versus the radii of curvature for metal waveguide bends with w=0.5μm and t being from 10nm to 15nm (see Fig. 4-1). (a_i) to (f_i) $(i=1,2)$ are for t=10nm to t=15nm, respectively. The subscript i identifies different kinds of losses, where $i=1$ represents insertion losses, and $i=2$ denotes pure radiation losses.

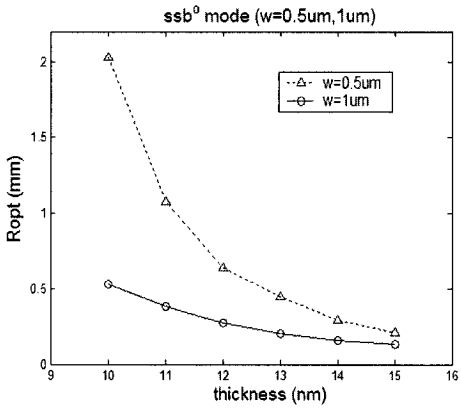

(a)

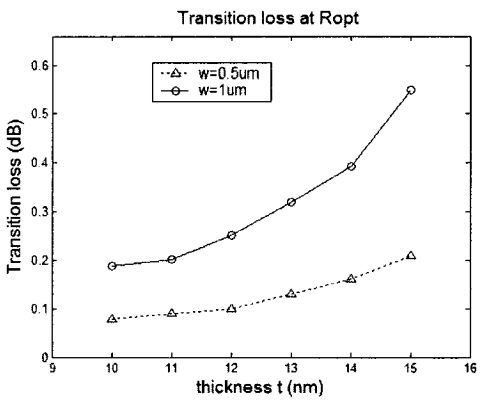

(b)

Fig. 4-10 Optimum radii of curvature and corresponding transition losses for metal waveguide bends. The solid line represents the case of w=1μm, and the dashed line shows the case of w=0.5μm. (a) gives optimum radii of curvature for metal waveguide bends with different geometrical combinations; (b) gives the transition loss when the curved metal waveguide with the optimum radius is connected to a straight one.

(B) Normalized phase constants

Figure 4-11 gives normalized phase constants (β/β_o) versus radii of curvature, where (a) to (f) are for w=1μm, and t=10nm to t=15nm, respectively. The solid lines show the results for the curved metal waveguides, and the dashed lines represent results for straight waveguides. From Fig. 4-11, it is observed that the normalized phase constant will increase due to the bending, and tends to be that of the straight waveguide asymptotically when the radius becomes infinitely large. For metal waveguide bends, the trend of the bending-induced increase of the normalized phase constants is the same as the Pregla's rib bend structure shown in Chapter 3. This behavior is attributed to the fact that bent metal waveguides analyzed here belong to the symmetrical-waveguide type and the rule of bending-induced increase holds for all waveguides symmetric about the vertical axis [3].

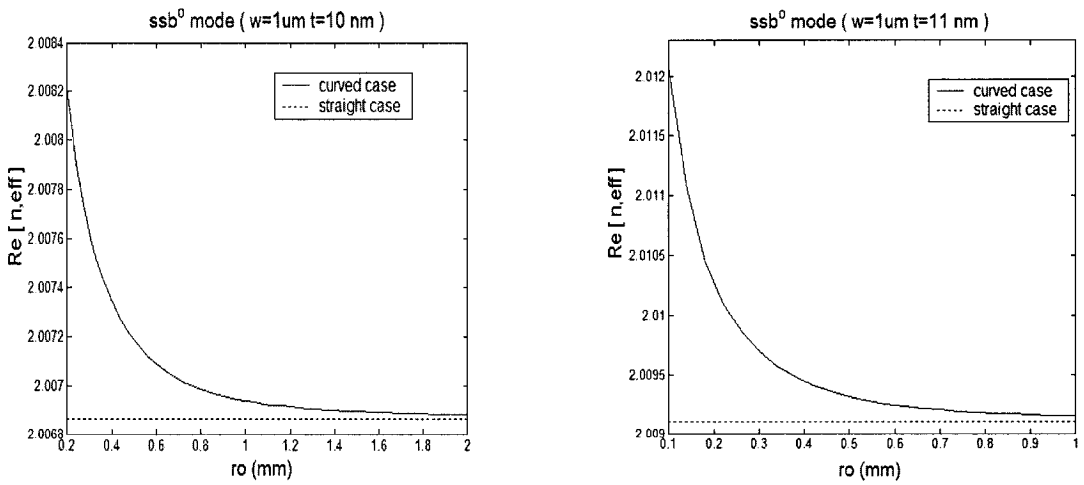

(a) (b)

Fig. 4-11 continues from page 96- page 97.

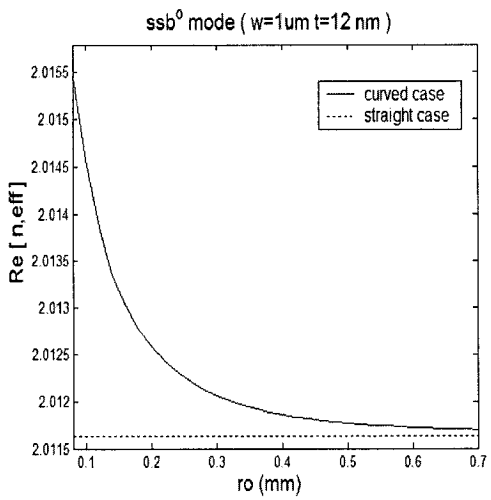

(c)

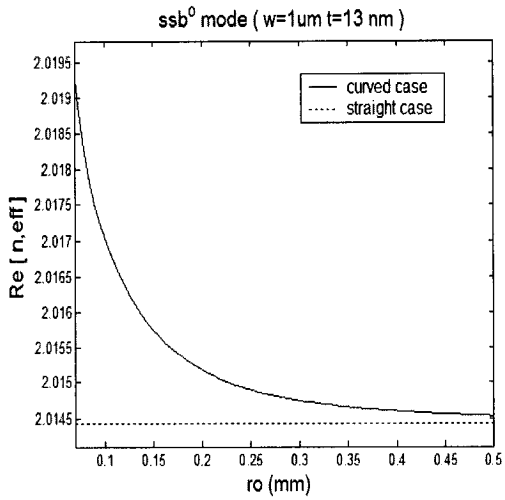

(d)

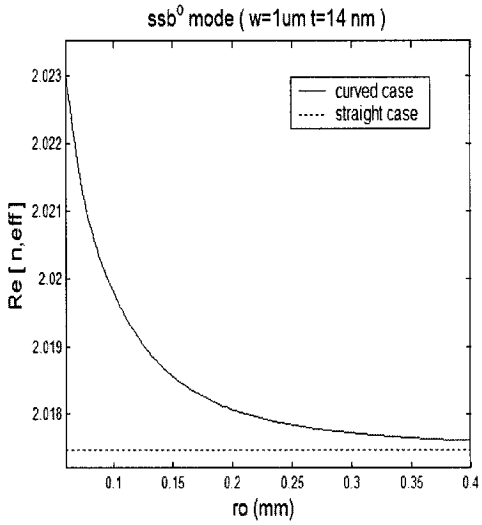

(e)

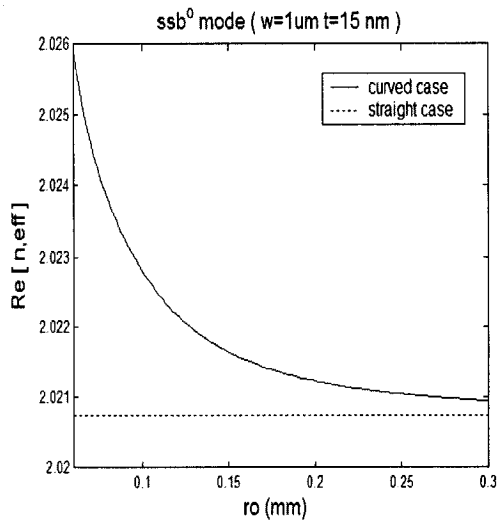

(f)

Fig. 4-11 The normalized phase constant (β / β_o) versus radii of curvature. (a) to (f) are for w=1μm, and t=10nm to t=15nm, respectively. The solid lines show the results for the curved metal waveguides, and the dashed lines represent results for straight cases.

4.3.2 Modal field distributions

(A) 1D dominant modal field distributions of the ss_b^o mode

Figure 4-12 and Fig. 4-13 present 1D normalized dominant electric field distributions (the real part of Ez) of the ss_b^o mode supported by the curved metal waveguides with w=1μm, and w=0.5μm, respectively. Note that these fields are obtained at the interface between the metal film and the cladding, but in the cladding. Fig. 4-12 (a) to Fig. 4-12 (f) or Fig. 4-13(a) to Fig. 4-13 (f) are correspondingly for t=10nm to t=15nm, respectively. Three curves on Fig. 4-12 (a) to Fig. 4-12 (f) or Fig. 4-13(a) to Fig. 4-13 (f) correspond to three different radii of curvature; among them, one case is the radius being 1m, another case corresponds to the upper limits of the radius of the radiation curves shown in Fig. 4-8 or Fig. 4-9 and the third radius is chosen so that it is shown distinctly from others on one figure. From Fig. 4-12 and Fig. 4-13, it is found that the field is actually propagating toward the $+r$ direction when the radius of curvature is small, which results in the radiation loss, and that the bending shifts the modal field peak radially outward and makes it more asymmetric for a smaller bend radius.

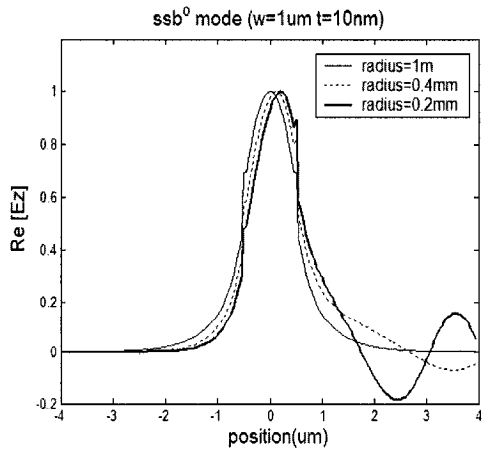

(a)

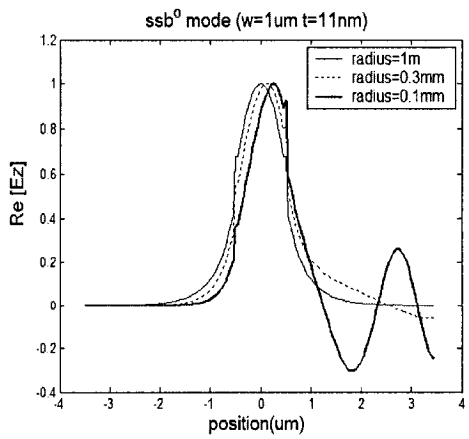

(b)

Fig. 4-12 continues from page 98- page 99.

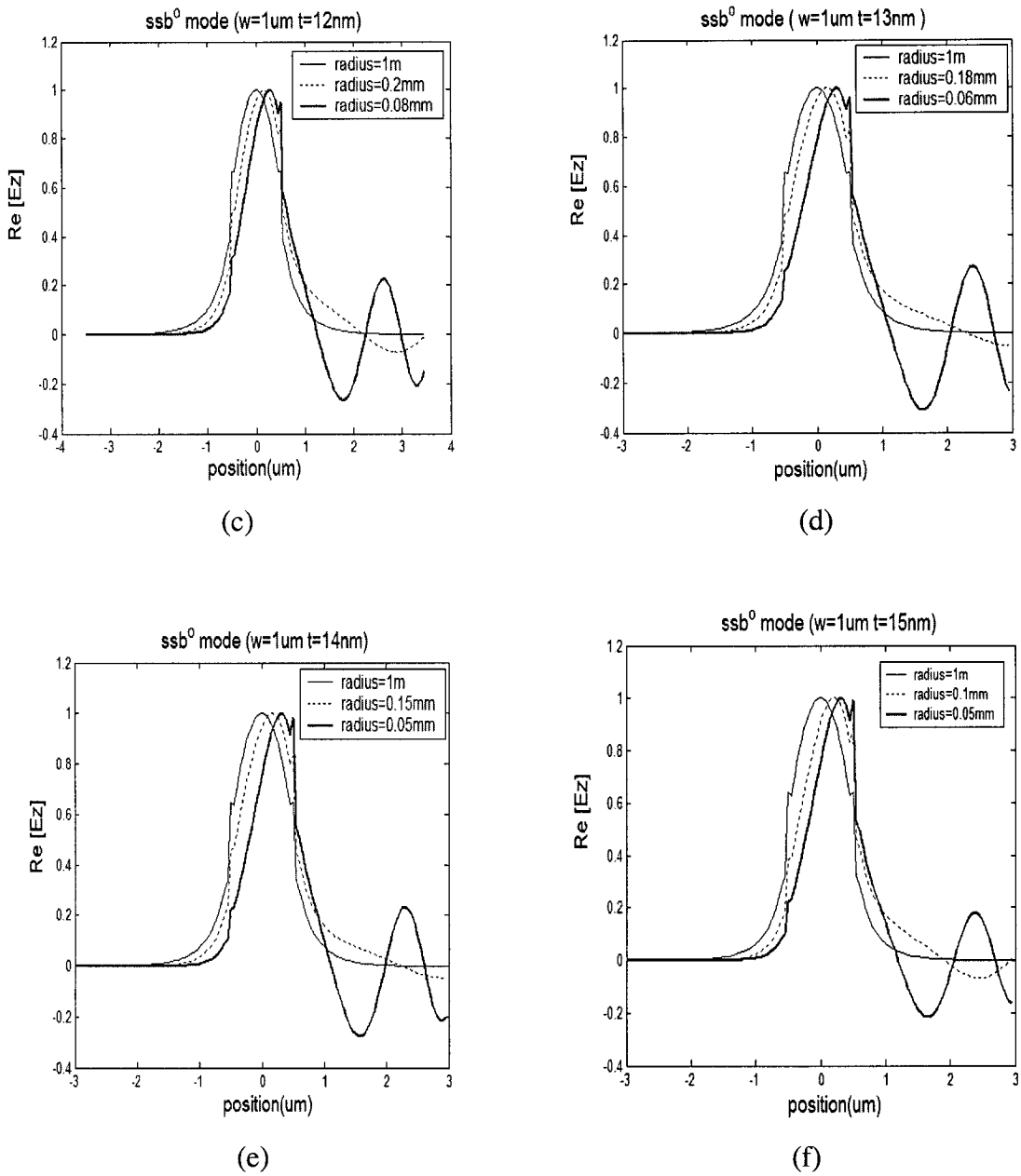

Fig.4-12 1D normalized dominant electric field distributions of the ss_b^o mode supported by the curved metal waveguides with w=1μm and different thickness t. (a) to (f) are for t=10nm to t=15nm, respectively. Three curves on (a) to (f) correspond to three different radii of curvature.

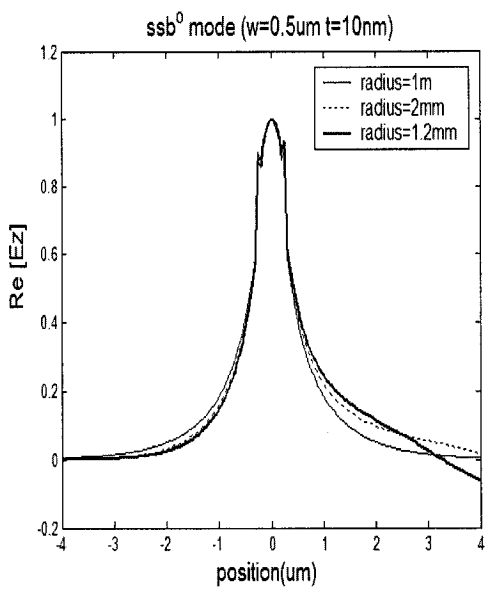

(a)

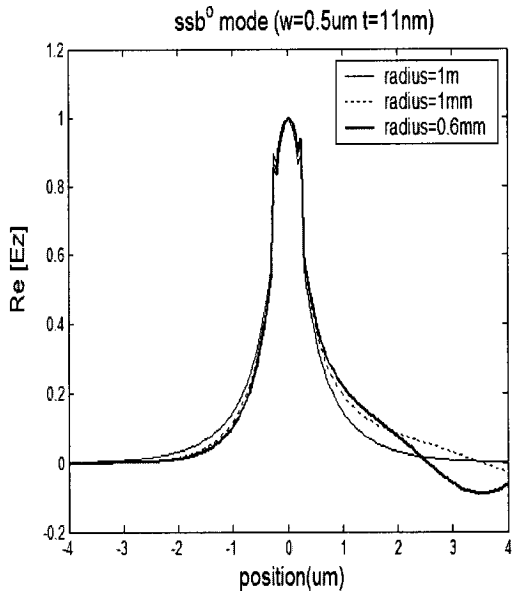

(b)

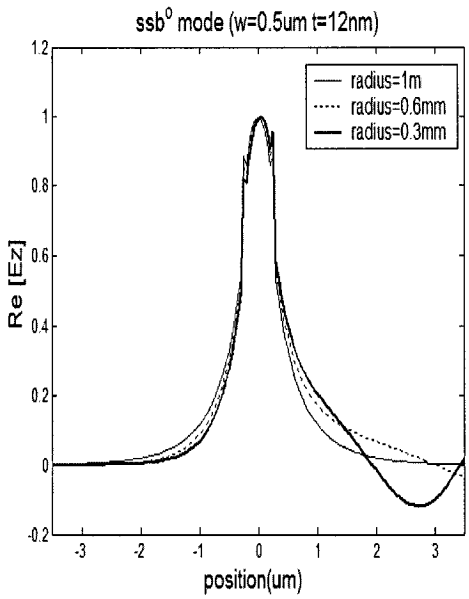

(c)

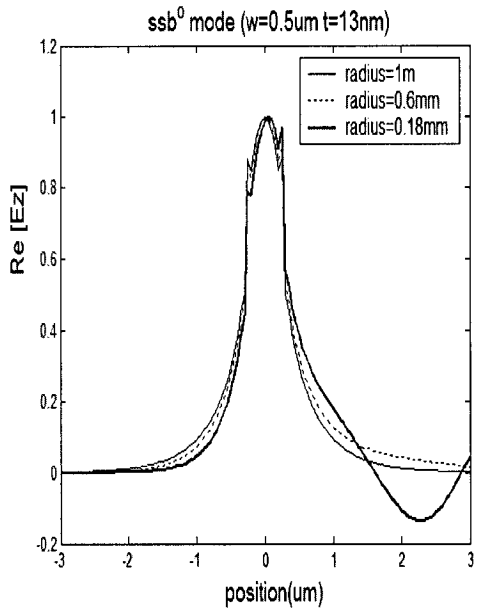

(d)

Fig. 4-13 continues from page 100- page 101.

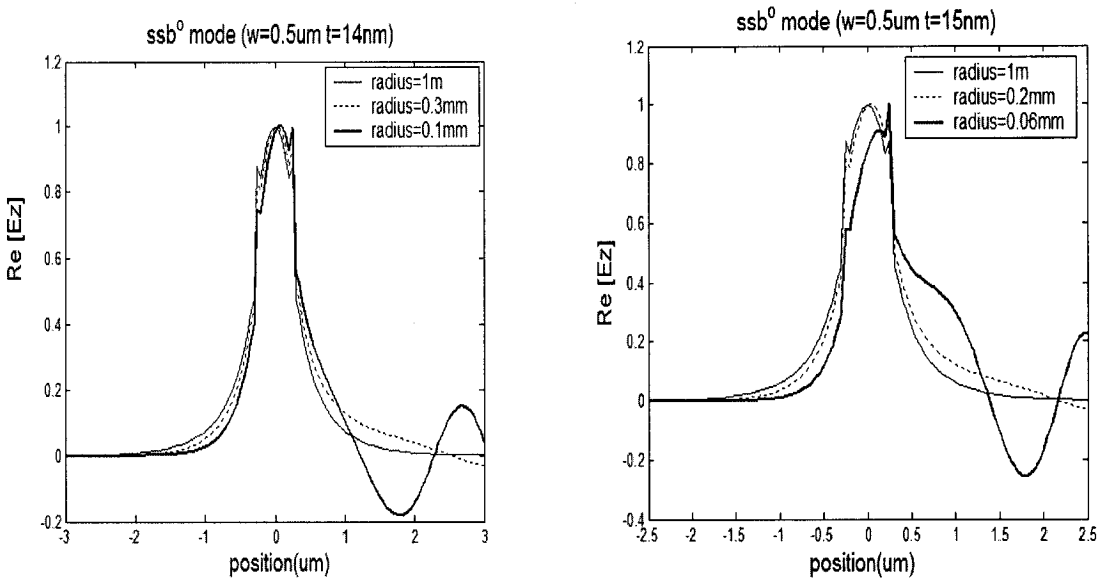

(e) (f)

Fig.4-13 1D normalized dominant electric field distributions of the ss_b^o mode supported by the curved metal waveguides with w=0.5μm and different thickness t. (a) to (f) are for t=10nm to t=15nm, respectively. Three curves on (a) to (f) correspond to three different radii of curvature.

(B) 2D modal field distributions of the ss_b^o mode

Figure 4-14 and Fig. 4-15 give contour plots of normalized dominant electric field distributions of the ss_b^o mode supported by the curved metal waveguides with w=1μm or 0.5μm, and different thickness t. For each geometrical combination, two contour plots are given. One is for the radius being 1m, and the other case is for the optimum radius. (a_i) to (f_i) ($i=1,2$) of Fig. 4-14 or Fig. 4-15 are for t=10nm to t=15nm, respectively. The subscript i identify the radius, where $i=1$ represents the case of radius=1m, and

$i = 2$ denotes the case of the optimum radius. From Figure 4-14 and Fig. 4-15, it can be seen that a smaller geometrical-size metal waveguide has more spreading field distributions, and that the peak of the field distributions of a smaller geometrical-size bent metal waveguide shifts a smaller distance at the optimum radius. The smaller shifting distance of the peak of the field distributions can explain why a smaller geometrical-size bent metal waveguide results in lower transition loss at its optimum radius.

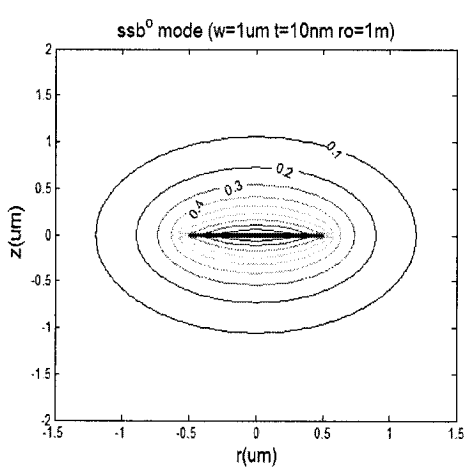

(a_1)

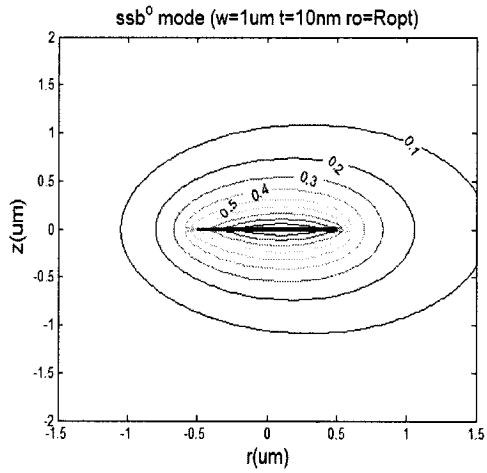

(a_2)

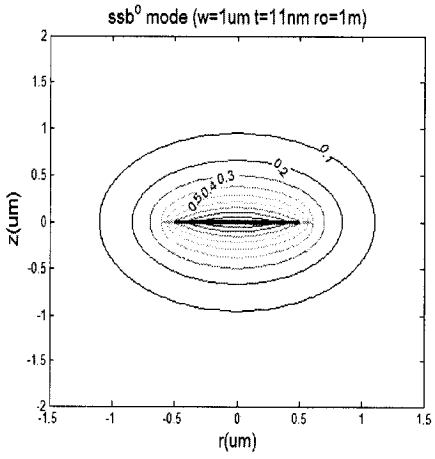

(b_1)

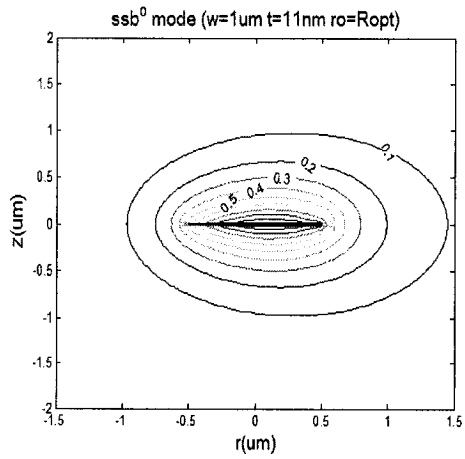

(b_2)

Fig. 4-14 continues from page 102- page 104.

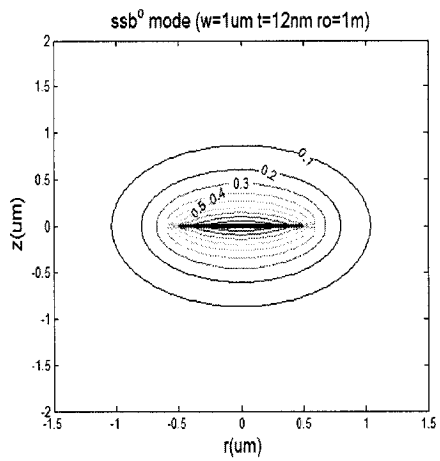

(c_1)

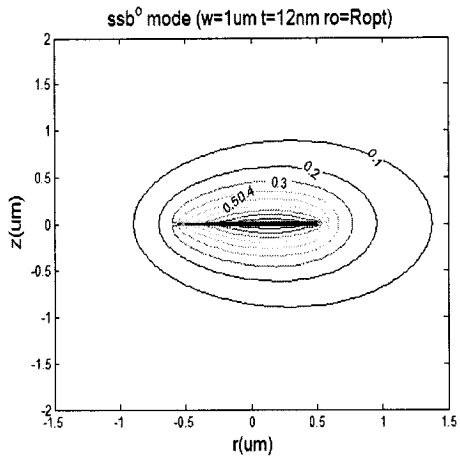

(c_2)

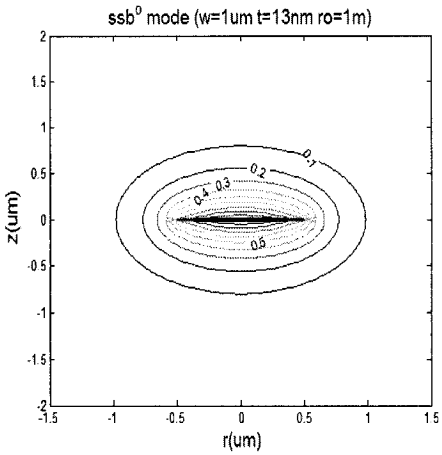

(d_1)

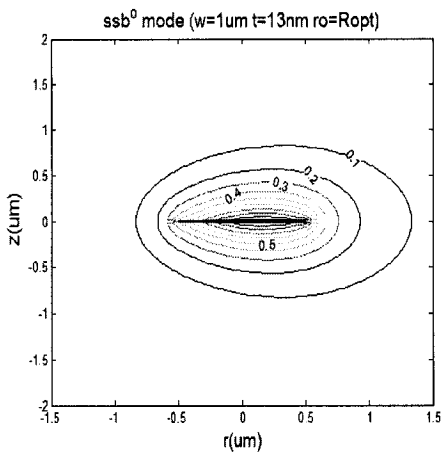

(d_2)

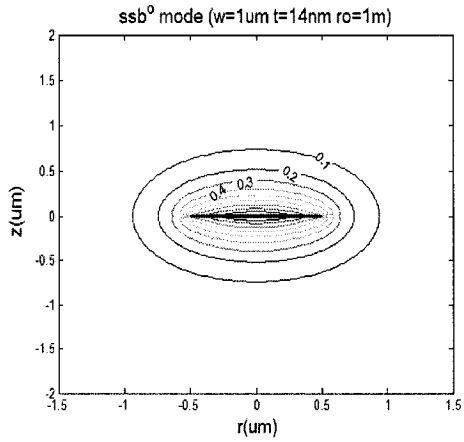

(e_1)

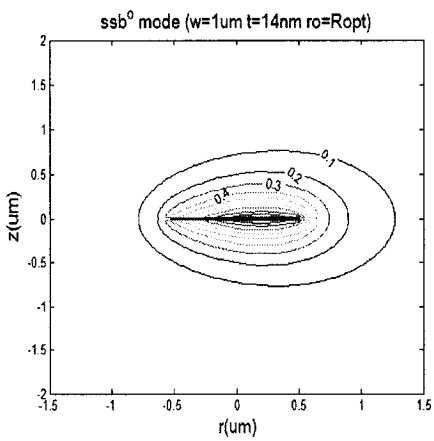

(e_2)

Fig. 4-14 continues from page 102- page 104.

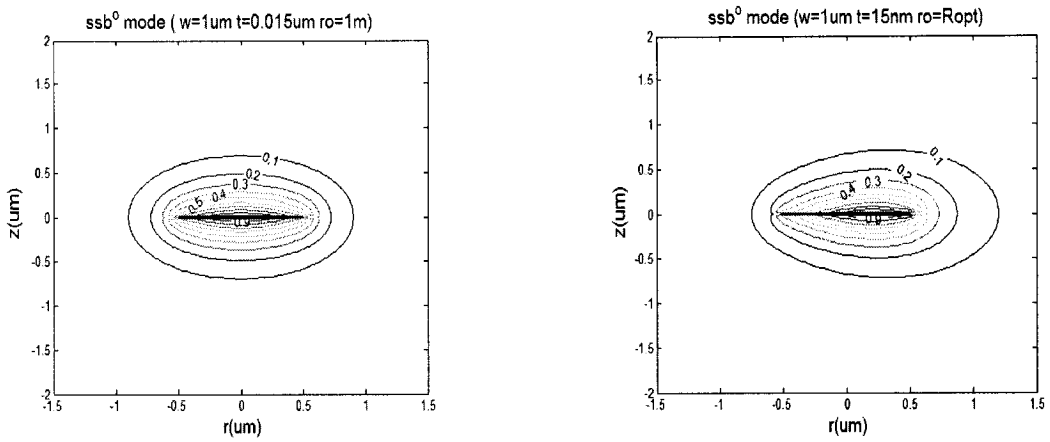

(f_1) (f_2)

Fig.4-14 Contour plots of normalized dominant electric field distributions of the ss_b^o mode supported by the curved metal waveguides with w=1μm and different thickness t. (a_i) to (f_i) $(i=1,2)$ are for t=10nm to t=15nm, respectively. The subscript i identify the radius, where $i=1$ represents the case of radius=1m, and $i=2$ denotes the modal distribution with the optimum radius.

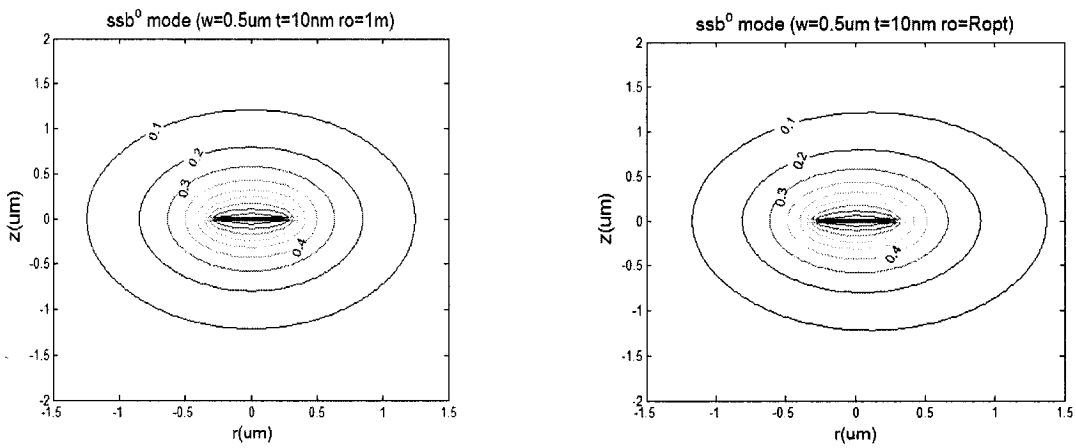

(a_1) (a_2)

Fig. 4-15 continues from page 104- page 106.

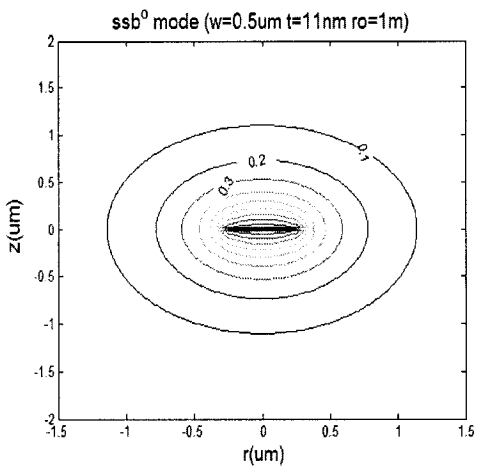

(b_1)

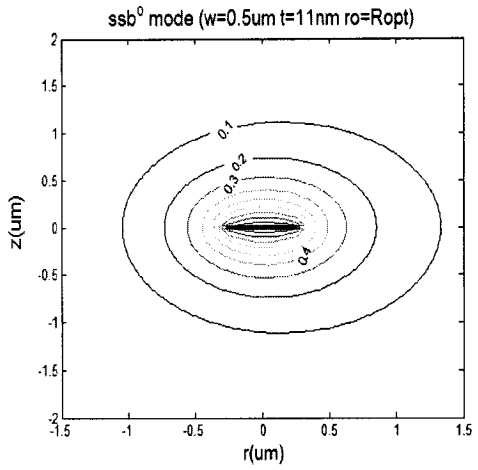

(b_2)

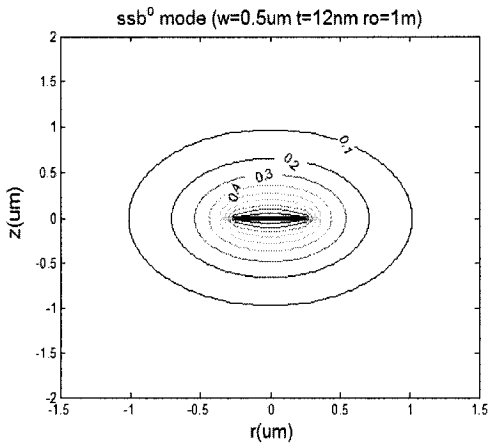

(c_1)

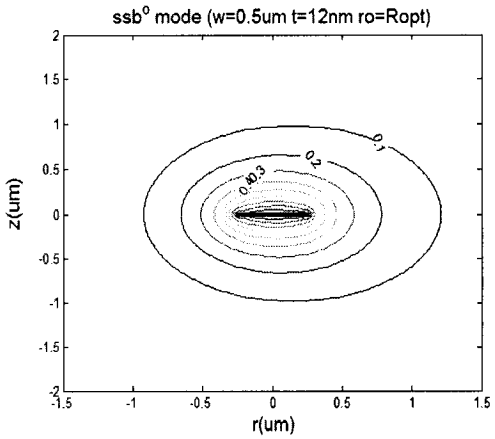

(c_2)

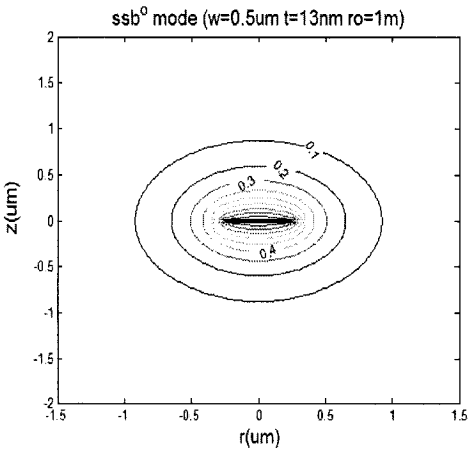

(d_1)

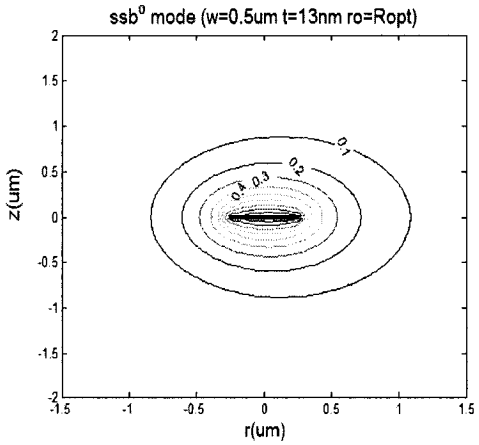

(d_2)

Fig. 4-15 continues from page 104- page 106.

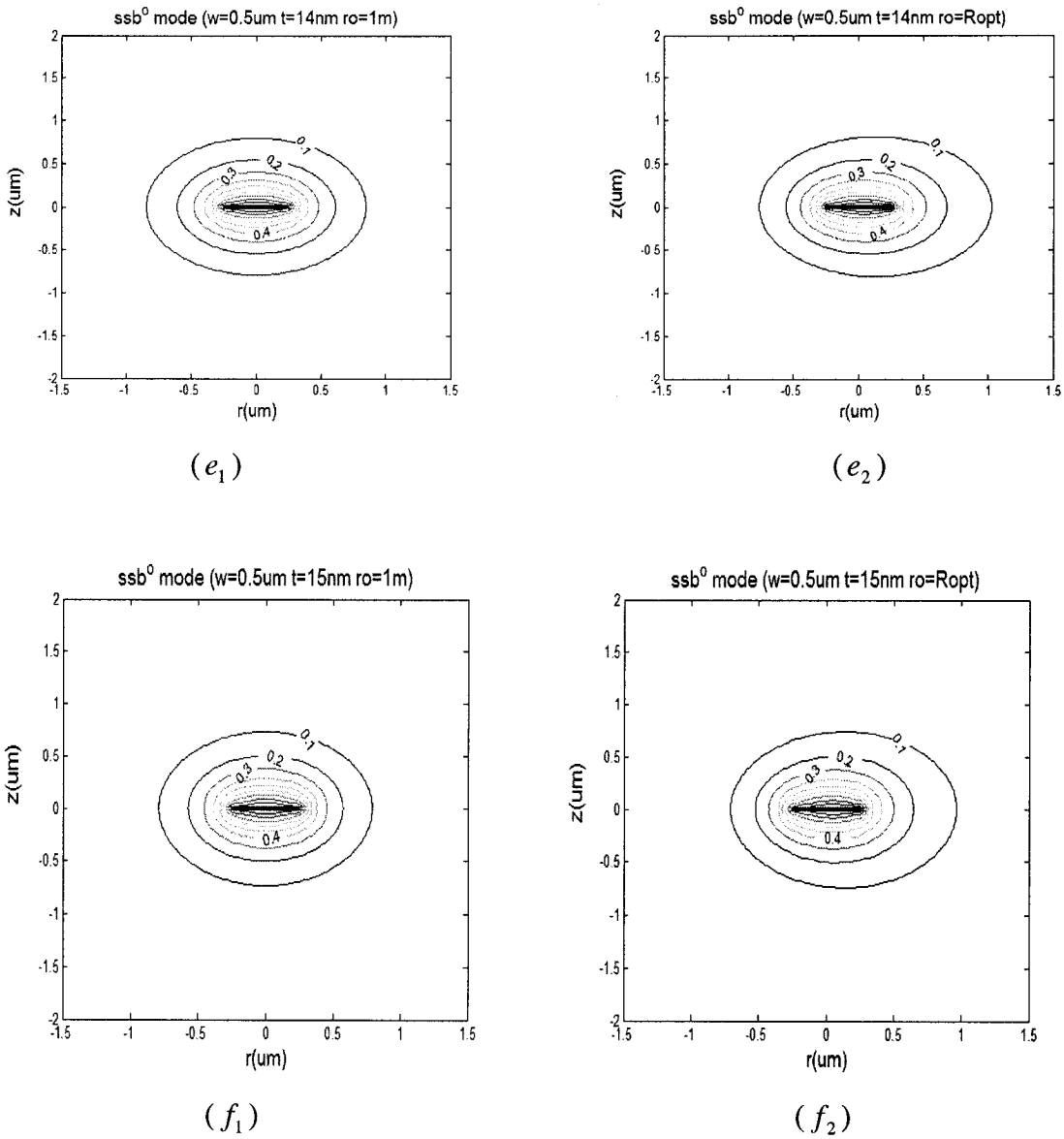

(e_1) (e_2)

(f_1) (f_2)

Fig.4-15 Contour plots of normalized dominant electric field distributions of the ss_b^o mode supported by the curved metal waveguides with w=0.5μm and different thickness t. (a_i) to (f_i) $(i=1,2)$ are for t=10nm to t=15nm, respectively. The subscript i identify the radius, where $i=1$ represents the case of radius=1m, and $i=2$ denotes the modal distribution with the optimum radius.

4.4 Conclusion

This chapter analyzes the plasmon-polariton waveguides, i.e., metal optical waveguides, with an emphasis placed on the mode propagation characteristics of metal optical waveguide bends. The analysis of metal optical waveguide bends includes 12 cases of structures with different widths and thicknesses. The simulation results for the insertion loss, and the pure radiation loss of these bend structures are shown, and the optimum radii of curvature, which correspond to the minima of the insertion losses of these bend structures, are also presented in this chapter. Considering the importance of the optimum radius curvature, the transition loss at this point is analyzed for each case of the bend structure. The numerical analyses of the mode propagation characteristics of the metal waveguide bends at the optical frequencies in this chapter are presented for what is believed to be the first time.

Chapter 5

Conclusions

5.1 Thesis Summary

This thesis mainly deals with the modeling of the propagation characteristics in optical waveguide bends: The radiation loss from the waveguide-bending effect, and the transition loss due to the modal mismatch at the junction of waveguides with different radii of curvature.

The modeling is set up based on the cylindrical MoL. The detailed formulation includes the algorithms for the analysis of the propagation characteristics and those for six 1D and 2D electromagnetic field distributions. The code is implemented successfully, verified by the validation in Chapter 3. The initial goal to set up a design tool for analyzing propagation characteristics in an optical waveguide bend using the method of lines (MoL) has been reached.

In this thesis, the developed code is applied to the analysis of the finite-width metal waveguide bend. To the author's best knowledge, no numerical work regarding the insertion loss of the metal waveguide bend with finite width has appeared in the literature up to now. It has demonstrated the usefulness of the tool for practical designs in the integrated optics technology.

5.2 Future Extensions

Although the code was proven to be very suitable for the analysis of circular bends with various cross sections, it has a limitation for the analysis of the longitudinal inhomogeneous waveguide bends, such as the optical taper bend. To overcome this limitation, some extensions should be made to the code.

To analyze the longitudinal inhomogeneous bent waveguide, R. Pregla and J. Gerdes etc., in [54], have put forward a beam-propagation algorithm based on MoL, and got satisfactory numerical results. As a result, the code based on the BPM-MoL algorithm can be incorporated into the design tool to make it function more generally.

Appendix A

Muller's Method

The procedure for Muller's method is developed by writing a quadratic equation that fits through three points in the vicinity of a root, in the form $av^2 + bv + c$ (See Fig. A-1). The development is simplified if we transform axes to pass through the middle point, by letting $v = x - x_0$.

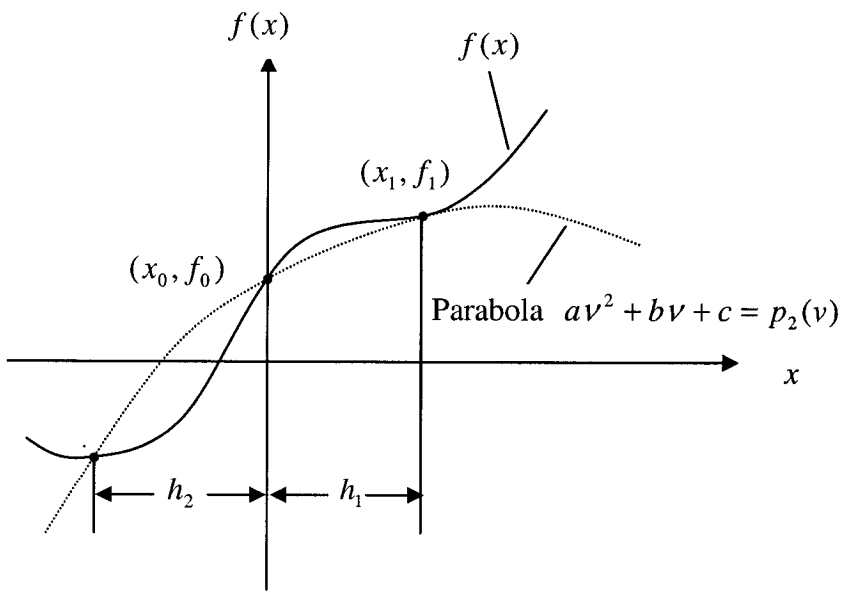

Fig. A-1

Let $h_1 = x_1 - x_0$ and $h_2 = x_0 - x_2$. We evaluate the coefficients by evaluating $p_2(v)$ at the three points:

$$v = 0: \qquad a(0)^2 + b(0) + c = f_0;$$

$$v = h_1: \qquad a(h_1)^2 + b(h_1) + c = f_1;$$

$$v = -h_2: \qquad a(h_2)^2 - b(h_2) + c = f_2;$$

From the first equation, $c = f_0$. Letting $h_2 / h_1 = v$, we can solve the other two equations for a and b:

$$a = \frac{v f_1 - f_0(1+v) + f_2}{v h_1^2 (1+v)} \tag{A.1}$$

$$b = \frac{f_1 - f_0 - a h_1^2}{h_1} \tag{A.2}$$

After computing $a, b,$ and $c,$ we solve for the root of $av^2 + bv + c = 0$ by the quadratic formula, choosing the root nearest to the middle point x_0. This value is

$$root = x_0 - \frac{2c}{b \pm \sqrt{b^2 - 4ac}} \tag{A.3}$$

With the sign in the denominator taken to give the largest absolute value of the denominator (that is, if b>0, choose plus; if b<0, choose minus: if b=0, choose either).

We take the root of the polynomial as one of a set of three points for the next approximation, taking the three points that are most closely spaced (that is, if the root is to the right of x_0, take x_0, x_1, and the root; if to the left, take x_0, x_2, and the root). We always reset the subscripts to make x_0 be the middle of the three values.

An algorithm for Muller's method is:

Given the points x_2, x_0, x_1 in increasing value,

1. Evaluate the corresponding function values f_2, f_0, f_1.
2. Find the coefficients of the parabola determined by the three points.
3. Compute the two roots of the parabolic equation.
4. Choose the root closest to x_0 and label it x_r.
5. IF $x_r > x_0$ THEN rearrange x_0, x_r, x_1 into x_2, x_0, x_1

   ELSE rearrange x_2, x_r, x_1 into x_2, x_0, x_1.
6. IF $|f(x_r)|$ <FTOL, THEN return x_r

   ELSE go to 1.

Note: As the Muller's Method is used to search for a complex root, the computation must, of course, use complex arithmetic.

Appendix B

Vector Differential Operator in Cylindrical Coordinates

1. Gradient

$$\nabla\psi = \hat{\rho}\frac{\partial\psi}{\partial\rho} + \hat{\phi}\frac{1}{\rho}\frac{\partial\psi}{\partial\phi} + \hat{z}\frac{\partial\psi}{\partial z} \tag{A.4}$$

2. Divergence

$$\Delta \bullet \bar{A} = \frac{1}{\rho}\frac{\partial}{\partial\rho}(\rho A_\rho) + \frac{1}{\rho}\frac{\partial A_\phi}{\partial\rho} + \frac{\partial A_z}{\partial\rho} \tag{A.5}$$

3. Curl

$$\nabla\times\bar{A} = \hat{\rho}(\frac{1}{\rho}\frac{\partial A_z}{\partial\phi} - \frac{\partial A_\phi}{\partial z}) + \hat{\phi}(\frac{\partial A_\rho}{\partial z} - \frac{\partial A_z}{\partial\rho}) + \hat{z}(\frac{1}{\rho}\frac{\partial(\rho A_\phi)}{\partial\rho} - \frac{1}{\rho}\frac{\partial A_\rho}{\partial\phi}) \tag{A.6}$$

4. Laplacian of a scalar field

$$\nabla^2\psi = \frac{1}{\rho}\frac{\partial}{\partial\rho}(\rho\frac{\partial\psi}{\partial\rho}) + \frac{1}{\rho^2}\frac{\partial^2\psi}{\partial\phi^2} + \frac{\partial^2\psi}{\partial z^2} \tag{A.7}$$

5. Laplacian of a vector field

$$\nabla^2\bar{A} = \nabla(\nabla\bullet\bar{A}) - \nabla\times\nabla\times\bar{A} \tag{A.8}$$

6. Expansion of the Laplacian of a vector field

$$\nabla^2 \vec{A} = \hat{\rho}\left(\frac{\partial^2 A_\rho}{\partial \rho^2} + \frac{1}{\rho}\frac{\partial A_\rho}{\partial \rho} - \frac{A_\rho}{\rho^2} + \frac{1}{\rho^2}\frac{\partial^2 A_\rho}{\partial \phi^2} - \frac{2}{\rho^2}\frac{\partial A_\phi}{\partial \phi} + \frac{\partial^2 A_\rho}{\partial z^2}\right)$$
$$+ \hat{\phi}\left(\frac{\partial^2 A_\phi}{\partial \rho^2} + \frac{1}{\rho}\frac{\partial A_\phi}{\partial \rho} - \frac{A_\phi}{\rho^2} + \frac{1}{\rho^2}\frac{\partial^2 A_\phi}{\partial \phi^2} + \frac{2}{\rho^2}\frac{\partial A_\rho}{\partial \phi} + \frac{\partial^2 A_\phi}{\partial z^2}\right) \qquad \text{(A.9)}$$
$$+ \hat{z}\left(\frac{\partial^2 A_z}{\partial \rho^2} + \frac{1}{\rho}\frac{\partial A_z}{\partial \rho} + \frac{1}{\rho^2}\frac{\partial^2 A_z}{\partial \phi^2} + \frac{\partial^2 A_z}{\partial z^2}\right)$$

7. Vector operator identities (hold in all coordinate systems)

$$\nabla \bullet (\nabla \times \vec{A}) = 0 \qquad \text{(A.10)}$$

$$\nabla \times \nabla \varphi = 0 \qquad \text{(A.11)}$$

$$\nabla \bullet (\varphi \vec{A}) = \vec{A} \bullet \nabla \varphi + \varphi \nabla \bullet \vec{A} \qquad \text{(A.12)}$$

$$\nabla \times (\varphi \vec{A}) = \nabla \varphi \times \vec{A} + \varphi \nabla \times \vec{A} \qquad \text{(A.13)}$$

Appendix C

The Component of ε_h at an Abrupt Transition

As numerical investigations have shown, it is best to put the interface, where the dielectric constant has an abrupt transition, on a ψ_h-line i.e. E line (or to choose the discretization in such a way that a ψ_h-line coincides with the interface line t) (shown as Fig. A.2). Which value of ε_r is to be inserted in ε_h on this line? To answer this question, we look at the behavior of ψ_e on the interface line t. On the interface itself ψ_e is continuous, but not $\partial\psi_e / \partial x$. Because of the continuity of the tangential E-field and the normal D-field components there is rather:

$$\psi_t^1 = \psi_t^2 \tag{A.14}$$

$$\frac{1}{\varepsilon_{r1}} \frac{\partial \psi_t^1}{\partial x} = \frac{1}{\varepsilon_{r2}} \frac{\partial \psi_t^2}{\partial x} . \tag{A.15}$$

Here, the subscript e is omitted as only ψ_e is regarded. Consequently, in the figure the ψ-curve is represented with a break on the interface; and the dashed curves are drawn without any break for the definition of the auxiliary quantities ψ_{k+1}^1 and ψ_k^1.

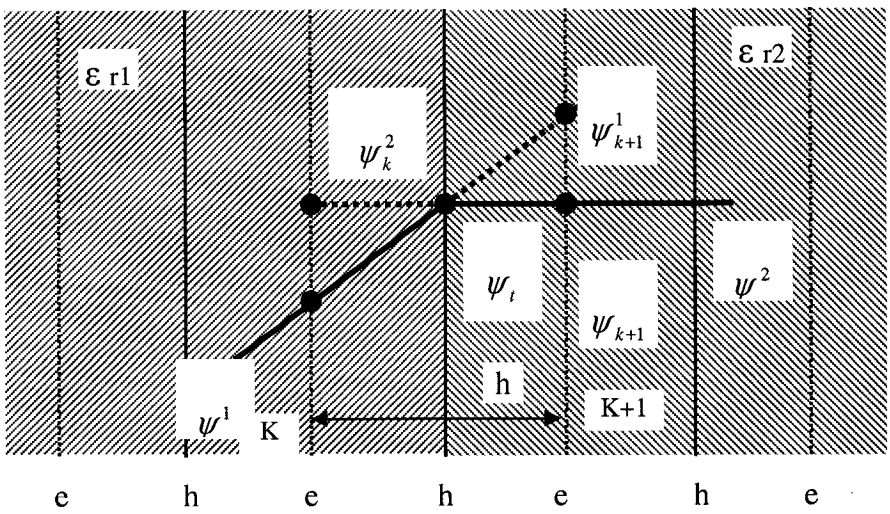

Fig. A-2 Behavior of ψ_e at an abrupt transition from ε_{r1} to ε_{r2}

These auxiliary quantities are necessary to compute the second derivative on the lines k and k+1. With the incremental formula (Taylor series up to the linear term, applied on the interface lint t) it is found:

$$\psi_{k+1}^1 \approx \psi_t + \frac{\partial \psi^1}{\partial x}\frac{h}{2} \tag{A.16}$$

$$\psi_{k+1} \approx \psi_t + \frac{\partial \psi^2}{\partial x}\frac{h}{2} \tag{A.17}$$

$$\psi_k \approx \psi_t - \frac{\partial \psi^1}{\partial x}\frac{h}{2} \tag{A.18}$$

$$\psi_k^2 \approx \psi_t - \frac{\partial \psi^2}{\partial x}\frac{h}{2} \tag{A.19}$$

Conditions (A.11) was immediately taken into account in these equations. With (A.11), we find for the two derivatives on the interface line:

$$h\frac{\partial \psi^1}{\partial x} \approx \frac{2\varepsilon_{r1}}{\varepsilon_{r1}+\varepsilon_{r2}}(\psi_{k+1}-\psi_k) \qquad \text{(A.20)}$$

$$h\frac{\partial \psi^2}{\partial x} \approx \frac{2\varepsilon_{r2}}{\varepsilon_{r1}+\varepsilon_{r2}}(\psi_{k+1}-\psi_k) \qquad \text{(A.21)}$$

With these, two derivatives are given by the special second derivatives on the lines k and k+1:

Line k: $$h^2\frac{\partial}{\partial x}\left(\frac{1}{\varepsilon_r}\frac{\partial \psi}{\partial x}\right) \approx \frac{2}{\varepsilon_{r1}+\varepsilon_{r2}}(\psi_{k+1}-\psi_k)-\frac{1}{\varepsilon_{r1}}(\psi_k-\psi_{k-1}) \qquad \text{(A.22)}$$

Line k+1: $$h^2\frac{\partial}{\partial x}\left(\frac{1}{\varepsilon_r}\frac{\partial \psi}{\partial x}\right) \approx \frac{1}{\varepsilon_{r2}}(\psi_{k+2}-\psi_{k+1})-\frac{2}{\varepsilon_{r1}+\varepsilon_{r2}}(\psi_{k+1}-\psi_k). \qquad \text{(A.23)}$$

References

[1] A. Melloni and F. Carniel, "Determination of bend mode characteristics in dielectric ic waveguides," *J. of Lightwave Tech.,* vol. 19, no. 4 pp. 571-577, April 2001.

[2] E.G. Neumann, and W. Richter, "Sharp bends with low losses in dielectric optical waveguides," *Applied Optics,* vol. 22, no.7, pp. 1016-1022, April 1983.

[3] W. k. Wang, R. Scotti, and D.J.Muehlner, " Phase compensation of bent silica-glass optical channel waveguide devices by vector-wave mode-matching method," *J. of Lightwave Tech.,*vol. 15, no. 3, pp. 538-545, March 1997.

[4] B. H.Verbeek, C.H. Henry, N.A. Olsson, K. J. Orlowsky, R.F. Kazarinov, and B.H Johnson, " Integrated four-channel Mach-Zehnder multi /dedemultiplexer fabricated with phosphorous doped SiO2 waveguides on Si," *J. of Lightwave Tech.,* vol. 6, pp. 1011-1015, June 1988.

[5] B.H.Verbeek and M.K. Smit, "Phased array based WDM devices," in *Proc. IOOC-ECOC 1995*, Paper Tu.A.3.1.

[6] E.A.J. Marcatili, "Bends in optical dielectric guides," *Bell Syst. Technol. J.*, vol. 48 pp. 2103-2132, 1969.

[7] D. Marcuse, "Bending losses of the asymmetric slab waveguide," *Bell Syst. Technol. J.*, vol. 50, no.8, pp. 2551-2563, Oct. 1971.

[8] D. Marcuse, *Light Transmission Optics*, 2nd Ed., New York: Van Nostrand Reinhold pp. 406-414, 1982.

[9] D. Marcuse, "Curvature loss formula for optical fibers," *J. Opt. Soc. Am.*, vol.66, pp. 216-220, Apr. 1966.

[10] D.Marcuse, " Field deformation and loss caused by curvature of optical fibers," *J. Opt. Soc. Am.*, vol. 66, no. 4, pp. 311-320, Apr. 1976.

[11] L. Lewin, " Radiation from curved dielectric slabs and fibers," *IEEE Trans. Microwave Thoery Tech.*, vol. MTT-22, no. 7, pp. 718-727, July 1974.

[12] M. Heiblum, and J. H. Harris, " Analysis of curved waveguides by conformal transformation," *IEEE J. Quantum Electron.*, vol. QE-11, pp. 75-83, 1975.

[13] C. Winker, J. D. Love, and A.K Ghatak, " Loss calculations in bent multimode optical waveguides," *Optical and Quatum Electron.*, vol.11, pp. 173-183, 1979.

[14] W. Berglund, and A. Gopinath, " WKB analysis of bend losses in optical waveguides," *J. of Lightwave Tech.*, vol. 18, no. 8, pp.1161-1166, August 2000.

[15] J. Janta, and J. Ctyroky, " On the accuracy of WKB analysis of TE and TM modes in planar graded-index waveguides," *Opt. Commun.*, vol. 25, pp. 49-52, 1978.

[16] A. Gedeon, " Comparison between rigorous theory and WKB analysis of modes in graded-index waveguides," *Opt. Commun.*, vol. 12, pp. 329-332, 1974.

[17] M. Rivera, " A finite difference BPM analysis of bent dielectric waveguide," *J. Lightwave Technol.*, vol. 13, pp.233-238, Feb. 1995.

[18] G. R. Hadley, "Transparent boundary conditions to the beam propagation method,"

IEEE J. Quantum Electon., vol. 28, pp. 363-370, 1992.

[19] T. Yamamoto, and M. Koshiba, " Numerical analysis of curvature loss in optical waveguides by finite-element method, " *J. Lightwave. Technol.*, vol. 11, pp. 1579-1583, Oct. 1993.

[20] J.S. Gu, P.A. Besse, and H. Melchior, "Novel method for analysis of curved optical rib-waveguides," *Electron. Lett.*, vol. 25, no.4, pp.278-279, Feb. 1989.

[21] J.S. Gu, P.A. Besse, and H. Melchior, "Method of lines for the analysis of the propagation characteristics of curved optical rib waveguides," *Opt. Quantum Electron.*, vol. 27, no.3, pp. 531-536, March 1989.

[22] H.J.M. Bastiaansen, J.M.van der Keur, and H. Block, "Rigorous, full vectorial source type integral equation analysis of circularly curved channel waveguides," *IEEE Microwave Theory Tech.*, vol. 43, pp. 401-409, Feb. 1995.

[23] S. Kim, and A. Gopinath, " Vector analysis of optical dielectric waveguide bends using finite-difference method," *J. Lightwave Technol.*, vol. 14, no. 9, pp. 2085-2092, Sept. 1996.

[24] W. Pascher, and R. Pregla, " Vectorial analysis of bends in optical strip waveguides by the method of lines," *Radio Science,* vol. 28, Number 6, pp. 1229-1233, 1993.

[25] R. Pregla, "The method of lines for the analysis of dielectric waveguide bends," *J. of Lightwave Technol.*, vol. 14, no. 14, pp. 634-638, April 1996.

[26] R. Pregla, and W. Pascher, "The method of lines," in *Numerical Techniques for Microwave and Millimeter Wave Passive Structures,* edited by T. Itoh, pp. 381- 446, John Wiley, New York, 1989.

[27] H. Diestel, and S.B. Worm, "Analysis of hybrid field problems by the method of lines with nonequidistant discretization," *IEEE Trans. Microwave Theory Tech.*, vol. 32, pp. 633-638, 1984.

[28] U. Rogge, and R. Pregla, " Method of lines for the analysis of strip-loaded optical waveguides, *J. Opt. Soc. Am., Part B,* vol. 8, pp. 459-463, Feb. 1991.

[29] A. Dreher, and R. Pregla, "Analysis of planar waveguides with the method of lines and absorbing boundary conditions," *IEEE Microwave and Guided Wave Letters,* vol. 1, no. 6, pp. 138-140, June 1991.

[30] R. Pregla, and D. Kremer, " Method of lines with special absorbing boundary conditions: analysis of weakly guiding optical structures, " *IEEE Microwave and Guided Wave Letters,* vol. 2, no. 6, pp. 239-241, June 1992.

[31] P. Berini, and K. Wu, " Modeling lossy anisotropic dielectric waveguides with the method of lines," *IEEE Trans. Microwave Theory and Tech.*, vol.44, no.5, pp.749-759, May 1996.

[32] F. J. Schmü, and R. Pregla, " Method of lines for the analysis of lossy planar waveguides," *IEEE Trans. Microwave Theory Tech.*, vol. 38, pp. 1473-1479, 1990.

[33] S. J. Al-Bader, and H. A. Jamid, "Perfectly matched layer absorbing boundary conditions for the method of lines modeling scheme," *IEEE Microwave and Guided Wave Letters.*, vol. 8, no.11, pp. 357-359, Nov. 1998.

[34] R. Pregla, and L. Vietzorreck, "Combination of the source method with absorbing boundary conditions in the method of lines," *IEEE Microwave and Guided Wave Letters*, vol. 5, no.7, pp. 227-229, July 1995.

[35] S.B. Worm, and R. Pregla, " Hybrid mode analysis of arbitrarily shaped planar mi-

crowave structures by the method of lines," *IEEE Trans. Microwave Theory Tech.* vol. MTT-32, pp. 191-196, Feb. 1984.

[36] U. Rogge, and R. Pregla, " Method of lines for the analysis of dielectric waveguides," *J. Lightwave Technol.*, vol. 11, no. 12, pp. 2015-2020, De. 1993.

[37] R. E. Collin, *Field Theory of Guided Waves*, McGraw-Hill Book Company, New York, Toronto, London, 1960.

[38] P. Berini, *Numerical Methods in Electromagnetic Engineering* , ELG. 5379 Course Notes in University of Ottawa, 2000 Ed.

[39] Feit. M.D., and J. A. Fleck, " Light propagation in graded-index optical fibers," *Appl. Opt.* ,vol. 17, pp. 3990-3998, 1978.

[40] Moore, T. G., J.G. Blaschak, A. Taflove, and G.A. Kriegsmann, " Theory and application of radiation boundary operators," *IEEE Trans. Antennas Propagation*, vol. 36, no. 12, pp. 1797-1811, 1988.

[41] R. Pregla, *Pr ogress in Electromagnetics Research*, PIER 11, pp. 51-102, 1995.

[42] A. Dreher, and R. Pregla, "Analysis of planar waveguides with the method of lines and absorbing boundary conditions," *IEEE Microwave and Guided Wave Letters,* vol. 1, no. 6, pp. 138-140, June 1991.

[43] R. Pregla, and D. Kremer,"Method of lines with special absorbing boundary conditions: analysis of weakly guiding optical structures," *IEEE Microwave and Guided Wave Letters,* vol. 2, no. 6, pp. 239-241, June 1992.

[44] R.J. Deri and R. J. Hawkins, " Polarization, scattering and coherent effects in simiconductor rib waveguide bends," *Opt. Lett.*, vol. 13, no. 10, pp. 922-924, 1988.

[45] M.W.Austin, "GaAs/GaAlAs curved rib waveguides," *IEEE J. Quantum Electron.*, vol. QE-18, pp. 795-800, Apr. 1986.

[46] P. Berini, " Plasmon-polariton modes guided by a metal film of finite width bounded by different dielectrics", *Opt. Exp.*, vol. 7, no. 10, pp. 329-335, Nov. 2000.

[47] P. Berini, " Plasmon-polariton waves guided by thin lossy metal films of finite width: bound modes of symmetric structures," *Phys. Rev.* B61, pp. 10484-10503 2000.

[48] R. Charbonneau, P. Berini, E. Berolo and E. Lisicha-Shrzek, " Experimental observation of plasmon-polariton waves supported by a thin metal film of finite width," *Opt, Lett.* 25, pp. 844-846, 2000.

[49] T. Kitoh, N. Takato, M. Yasu, and M. Kawachi, " Bending loss reduction in silica-based waveguides by using lateral offsets," *J. of Lightwave Tech.*, vol. 13, no.4, pp. 555-562, April 1995.

[50] H. Van Brug, F. H. Groen, Y. S. Oei, J. W. Pedersen, E. C.M. Pennings, D.K. Doeksen, and J.J.G.M. Van Der Tol, " Low-loss straight and curved ridge waveguides in LPE-grown GaInAsP," *Electron. Lett.*, vol. 25, no. 20, pp. 1330-1332, 1989.

[51] E.C.M. Pennings, G.H. Manhoudt, and M.K. Smit, " Low-loss bends in planar optical ridge waveguides," *Electro. Lett.*, vol. 24, no.16, pp. 998-999, 1988.

[52] J.J.G.M.van der Tol, J.W.Verhoff, and M.B.J. Diemeer, and E. C.M. Pennings, " S-bends using offsets in fiber-compatible K^+ - N_a^+ ion-exchanged glass waveguide," *Electron. Lett.*, vol. 27, no. 4, pp. 379-380, 1991.

[53] V.Va, P. P. Absil, J.V. Hryniewicz, and P.T. Ho, " Propagation loss in single mode GaAs-AlGaAs microring resonators: measurement and model," *J. of Lightwave*

Tech., vol. 19, no. 11, pp. 1734-1739, Nov. 2001.

[54] Gerdes, J., and R. Pregla, " Beam-propagation algorithm based on the method of lines." *J. Optical Society of America B*, vol.8, no.2, pp. 389-394, 1991.

[55] C. Kittel, *Introduction to Solid State Physics*, 6th Edition, Wiley Company, New York, Toronto, 1986.